MODELING, PATH PLANNING, AND CONTROL CO-DESIGN OF MARINE CURRENT TURBINES

by

Arezoo Hasankhani

A Dissertation Submitted to the Faculty of

The College of Engineering and Computer Science

in Partial Fulfillment of the Requirements for the Degree of

Doctor of Philosophy

Florida Atlantic University

Boca Raton, FL

May 2022

MODELING, PATH PLANNING, AND CONTROL CO-DESIGN OF MARINE CURRENT TURBINES

by

Arezoo Hasankhani

This dissertation was prepared under the direction of the candidate's dissertation co-advisors, Dr. Yufei Tang, Department of Electrical Engineering and Computer Science, and Dr. James VanZwieten, Department of Civil, Environmental and Geomatics Engineering, and has been approved by the members of her supervisory committee. It was submitted to the faculty of the College of Engineering and Computer Science and was accepted in partial fulfillment of the requirements for the degree of Doctor of Philosophy.

SUPERVISORY COMMITTEE:

Yufei Tang

Yufei Tang, Ph.D.
Dissertation Co-Advisor

James VanZwieten

James VanZwieten, Ph.D.
Dissertation Co-Advisor

Xiangnan Zhong
Xiangnan Zhong (May 25, 2022 10:29 EDT)

Xiangnan Zhong, Ph.D.

Hanqi Zhuang, Ph.D.

Manhar Dhanak

Manhar Dhanak, Ph.D.

Hanqi Zhuang, Ph.D.
Chair, Department of Electrical Engineering and Computer Science

M Cardei

Stella Batalama, Ph.D.
Dean, The College of Engineering and Computer Science

Robert W. Stackman Jr.
Robert W. Stackman Jr. (May 26, 2022 23:12 EDT)

Robert W. Stackman Jr., Ph.D.
Dean, Graduate College

June 1, 2022

Date

ACKNOWLEDGEMENTS

I would like to express my sincere appreciation to all the people who have helped me in ways large and small in my journey to a Ph.D.

First, I would like to express my gratitude to my advisor Dr. Yufei Tang, for his trust, support and guidance in the past several years. He has helped me expand my boundaries and pushed me to achieve the highest standard that I am able to reach within my ability.

I am incredibly grateful to my co-advisor Dr. VanZwieten for his patient and delicate guidance. I was fortunate to be able to work with him. Huge thanks to his professional and insightful suggestions to help improve my work and teach me to think creatively.

I would like thank my committee members, Drs. Xiangnan Zhong, Hanqi Zhuang, and Manhar Dhanak, who took time out of their busy lives to provide valuable suggestions and improve my work.

I have to thank my husband, my best friend, and the love of my life, Mojtaba, for his endless support, patience, and love. I must express my very profound gratitude to my parents and my brother for providing me with unfailing support. Last but not least, I would like to thank my beloved sister, Elahe, for her enduring love and encouragement.

Many thanks as well to all my colleagues from I-SENSE at Florida Atlantic University, for their endless help and making me feel like I am a part of the big family.

This dissertation research was supported in part by the U.S. National Science Foundation under Grant Nos. ECCS-1809164, CMMI-2145571, & OAC-2017597 and the U.S. Department of Energy under Grant No. DE-EE0008955.

ABSTRACT

Author:	Arezoo Hasankhani
Title:	Modeling, Path Planning, and Control Co-Design of Marine Current Turbines
Institution:	Florida Atlantic University
Dissertation Co-Advisors:	Dr. Yufei Tang Dr. James VanZwieten
Degree:	Doctor of Philosophy
Year:	2022

Marine and hydrokinetic (MHK) energy systems, including marine current turbines and wave energy converters, could contribute significantly to reducing reliance on fossil fuels and improving energy security while accelerating progress in the blue economy. However, technologies to capture them are nascent in development due to several technical and economic challenges. For example, for capturing ocean flows, the fluid velocity is low but density is high, resulting in early boundary layer separation and high torque. This dissertation addresses critical challenges in modeling, optimization, and control co-design of MHK energy systems, with specific case studies of a variable buoyancy-controlled marine current turbine (MCT). Specifically, this dissertation presents (a) comprehensive dynamic modeling of the MCT, where data recorded by an acoustic Doppler current profiler will be used as the real ocean environment; (b) vertical path planning of the MCT, where the problem is formulated as a novel spatial-temporal optimization problem to maximize the total harvested power of the system in an uncertain oceanic environment; (c) control co-design of the MCT, where the physical device geometry and turbine path control are optimized

simultaneously. In a nutshell, the contributions are summarized as follows:

- We propose a comprehensive modeling and numerical simulation of a 700 kW variable buoyancy controlled MCT for operation in a realistic environment of the Gulf Stream off the East Coast of Florida. A detailed turbine system is modeled, including actuator (i.e., generator and variable buoyancy), and the equations of motion of this system are presented. Simulation predictions of MCT performance are made for normal, hurricane, and fault conditions.

- We propose a novel spatiotemporal optimization problem for the MCT vertical path planning operating in an uncertain oceanic environment to maximize the total harvested power of the system. Under this problem formulation, a reinforcement learning (RL)-based method is designed to explore the optimal control actions, and results are compared with a model predictive control (MPC)-based strategy. Moreover, an integrated path planning and tracking control is proposed, which includes a path planner that allocates an optimal path and a path controller to track the optimal reference path commanded from the planner subject to the MCT dynamic model and problem constraints.

- We propose a turbine geometric/spatiotemporal control co-design to maximize the power-to-weight ratio of a buoyancy-controlled MCT and analyze the whole design from hydrodynamics to power generation to ensure that it is optimal. To formulate a bi-directional coupling between plant design and path control, we propose a nested co-optimization framework, consisting of two optimization loops, i.e., an outer optimization loop responsible for the optimal design parameters and an inner optimization loop taking care of path planning.

Evaluations are carried out using field-collected Acoustic Doppler Current Profiler (ADCP) data and simulation in the Matlab/Simulink. Comparative studies with baseline designs validate the superiority of our proposed innovations.

MODELING, PATH PLANNING, AND CONTROL CO-DESIGN OF MARINE CURRENT TURBINES

LIST OF TABLES

LIST OF FIGURES

CHAPTER 1
INTRODUCTION

Electricity production from renewable energy sources has been steadily increasing due to environmental concerns associated with fossil fuels and recent advances in enabling technologies. This growth includes the increasing installation of both solar and wind technologies, as well as a push to harness additional renewable energy resources, such as marine hydrokinetic (MHK) energy. Although MHK energy technologies are still in their infancy when compared to other types of renewable energies, their vast power production potential along with the success of numerous prototype testing campaigns have encouraged the transition of these technologies into array deployments and interconnection with the electrical grid. A recent study suggests that about 2000 GW of power can be extracted from waves globally (300 GW from U.S. waters) and 1000 GW from tidal currents globally (50 GW in U.S.) [1]. In the U.S., an additional 14 GW of in-stream hydrokinetic power (i.e., not using dams) can be extracted from rivers [2] and 18.6 GW can be extracted from offshore ocean currents [3].

Significant potential for ocean current energy extraction exists along the western boundaries of ocean basins [4]. The Gulf Stream contains roughly 18.6 GW (i.e., 163 TWh/year) of available power in U.S. waters between Southeast Florida and North Carolina, with the Florida Current portion of the Gulf Stream containing 5.1 GW (i.e., 45 TWh/year) [3,5]. Ocean currents not only possess large quantities of extractable power but are also very power dense in several areas. This power density is depth dependent, with the highest values near the sea surface [6]. Hence, ocean current turbines should typically be located near the ocean surface, but would benefit from the capability of varying their depth to avoid surface waves during storms or

to maximize energy production during events where the most energy dense ocean currents occur at deeper depths.

This thesis focuses on the marine current turbine (MCT), which is an energy-harvesting autonomous underwater vehicle (AUV) and can be autonomously controlled to seek and follow the optimal path. Technologies are being developed to harness the high power potential, where the harnessed power is depth dependent. The main hurdles in developing MHK technologies are high investment and maintenance costs (e.g., due to hostile operating environment) and the difficulty of integrating their produced electricity into the grid. There are many approaches to address the high cost, such as lowering the cost of turbine design through control co-design [7, 8], optimizing the operational strategy [9], and specifically finding the optimal path/depth [10].

An MCT should autonomously navigate along the optimal path in the presence of a highly nonlinear and uncertain oceanic environment, accounting for the fact that the predicted ocean velocity is affected by perturbations. The main focus in this thesis is on the MCT designed for the open ocean currents. At the first step, a feasible and technical model for the MCT should be designed and numerically simulated, which can operate near the sea surface where the current is strongest, yet below the sea surface to avoid surface effects and/or interactions with surface vessels. An effective real-time path control may entail several prerequisites, leading to a challenging problem. The optimal path is acquired by optimizing an ultimate goal, i.e., maximizing harvested energy from an MCT in a given time period. Moreover, the optimal path may change continuously due to the inherent spatiotemporal uncertainties in the oceanic environment [11]. The highly nonlinear dynamic model of the MCT that includes multi-physics couplings increases the problem complexity. Therefore, the challenges of optimization and control are significant for the MCTs. The MCT system is investigated in the following aspects in this thesis.

1.1 MCT MODELING AND NUMERICAL SIMULATION

Several technologies have been proposed to maintain a proper operating depth for the MCT system: variable buoyancy [12–16], lifting surfaces or wings [17–21], sub-sea winches [22], and surface buoys [23,24]. Among these proposed structures, the variable buoyancy solution seems to be more feasible, as this design type was the first to be deployed in an open ocean current while moored directly to the seafloor [12]. However, there exists a lack of a model to precisely describe the dynamic characteristics of the buoyancy controlled MCT and predict its performance for normal, hurricane, and fault scenarios. Another feasible approach for the MCT system is a lifting surface controlled MCT, which has been limitedly modeled and studied in the literature.

We develop a comprehensive modeling and numerical simulation of a buoyancy-controlled MCT for operation in a realistic environment of the Gulf Stream off the East Coast of Florida. Then, we predict the performance of this buoyancy-controlled MCT over realistic flow speed inputs that vary both spatially and temporally to simulate a realistic underwater operating environment.

1.2 MCT PATH PLANNING

The MCT can be treated as an AUV but with the primary role of energy generation. The challenge for MCT path planning is unique since the turbine is tethered to the seafloor through a mooring system. It is critical to study the path planning for MCT in the turbulent oceanic environment with the absence of human intervention (e.g., remote areas and deep-sea). A predictive methodology is nominated in the literature to design the planner in the presence of an approach to model the environmental uncertainties and give a fair prediction from the environment, taking into account the proposed approach in similar applications of airborne wind turbines [25] and underwater vehicles [10]. However, the error between the predicted ocean environment

and the real one should not be neglected, which is the main intuition to move towards the approach relying more on the real measured data from the oceanic environment instead of the predicted data.

We advocate a novel spatiotemporal optimization problem for the MCT vertical path planning operating in an uncertain oceanic environment to maximize the total harvested power of the system. Under this problem formulation, a reinforcement learning (RL)-based method is designed to explore the optimal control actions, and results are compared with a model predictive control (MPC)-based strategy and a baseline A* approach.

1.3 CONTROL CO-DESIGN FOR MCT

Most existing studies on the MCT have been carried out on mechanical and structural design. Yet, a scientific gap in developing a co-design to couple the physical design and the path control has been identified. Despite the intensive study on developing the control co-design in a sister field of wave energy conversion [7], there exists limited literature on the co-design of the MCT energy system, such as an ocean kite [26]. Given the complexities of the MCT and spatiotemporal uncertainties of ocean currents, a detailed study on designing the control co-design is well deserved; however, the control challenges are intensified due to an inefficient mechanical design.

We advance the control co-design for buoyancy-controlled MCT to optimize the physical design and path control simultaneously. Note that the planned path should qualify for the physical design, and the MCT system is able to follow this path through its controllers and actuators. Eventually, there exist several major features that are required to be addressed in the mechanical design to harness a fair amount of power from the ocean currents.

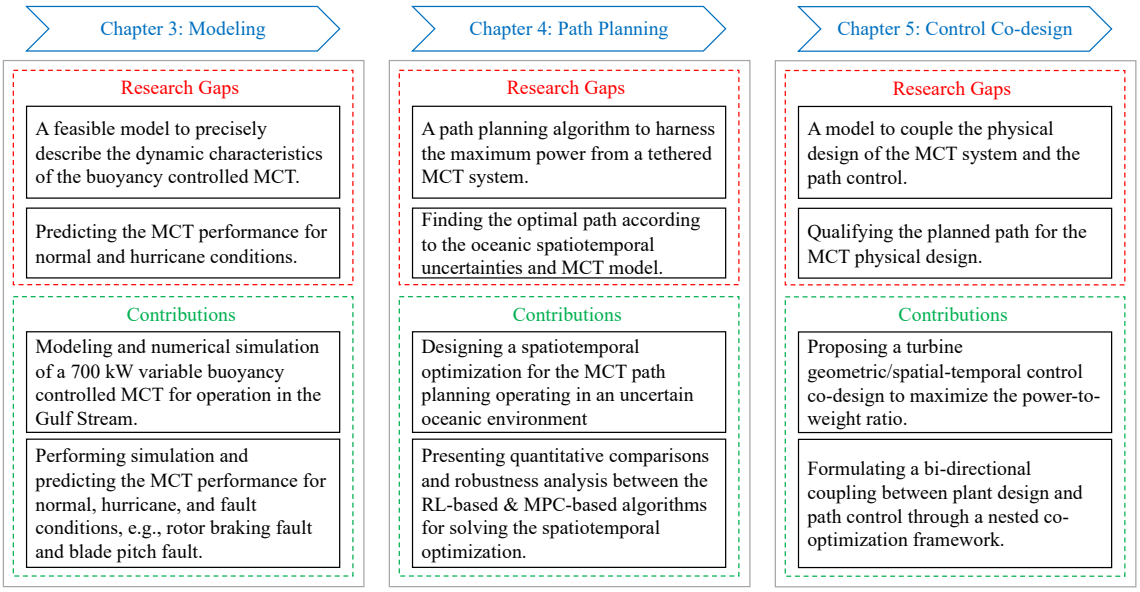

Figure 1.1: Schematic of the research gaps and proposed contributions in the field of modeling, path planning, and control co-design of a marine current turbine.

1.4 THESIS ORGANIZATION

This thesis studies the buoyancy-controlled MCT in three aspects, including, modeling, path planning, and control co-design, which are elaborated in chapters 3, 4, and 5, respectively. A schematic of the research gaps and the corresponding contributions in this dissertation are shown in Figure 1.1. Currently, the prototype is under development, and the research carried out in this thesis will lay out the foundation for future validation, where the proposed model and approach will be tested on a real MCT prototype.

More specifically, we organize the thesis as follows. Chapter 2 briefly describes the background and literature review on the modeling, path planning, and control co-design of the MCT systems. Chapter 3 deals with modeling and numerical simulation for the buoyancy controlled MCT, as well as performing simulation to predict the performance of the MCT under different conditions. Chapter 4 develops a new spatiotemporal optimization for the MCT path planning to maximize the harnessed

power from this system. Chapter 5 presents a control co-design framework to couple the physical design and path control and find the optimal MCT design by maximizing the power-to-weight ratio. Finally, Chapter 6 concludes the thesis and discusses the future directions.

Chapter 2: Literature Review

In this chapter, we review the literature on the MCT system. First, we discuss the numerical modeling of MCT systems addressed in a series of publications focused on system dynamics and environmental conditions. Then, we summarize the existing works on path planning of the AUV systems, especially the energy-harvesting AUVs and MCT. We also present the background on the control co-design of the MHK turbines to couple the physical design and the cyber controllers.

Chapter 3: Modeling of Buoyancy Controlled MCT

In this chapter, we present the modeling and numerical simulation for the investigated 700 kW MCT as a representative design for operation in the Gulf Stream off Florida's East Coast, which consists of two variable buoyancy sections of a single variable buoyancy tank, variable pitch rotor, main body, and a 607 m mooring cable attached to the ocean floor at a depth of 325 m. We also present the numerical simulation results of testing the MCT system for different conditions, including normal, hurricane, and fault conditions.

Chapter 4: Path Planning Algorithm for Buoyancy Controlled MCT

In this chapter, we formulate the path planning algorithm by a spatiotemporal optimization approach to maximize the net output power of the MCT under uncertain ocean velocities. We apply two different algorithms, including MPC as a model-based method and RL as a learning-based method, to solve the formulated spatiotemporal optimization problem with constraints. We also perform the quantitative comparisons between the results obtained by the RL method, the MPC approach, and a baseline

A* approach. Then, we present an integrated path planning and tracking control for the MCT that iteratively plans the optimal path to maximize the harvested power and tracks the commanded path to minimize the tracking error.

Chapter 5: Control Co-design for Buoyancy Controlled MCT

In this chapter, we present a novel control co-design framework for the MCT system to maximize the power-to-weight ratio for the buoyancy controlled MCT and couple the mechanical design with the path control. We formulate and solve this control co-design problem by a nested multi-level co-optimization to take care of the optimal physical design as well as path planning and path tracking.

Chapter 6: Discussion and Future Work

In the final chapter, we conclude the thesis and summarize the contributions to modeling, path planning, and control co-design of the buoyancy-controlled MCT. We then discuss the main ideas for expanding the current study to other autonomous renewable energy systems and present the potential directions to continue the current thesis.

1.5 THESIS CONTRIBUTION

In summary, our major contributions in this thesis are demonstrated in three aspects:

- We propose a comprehensive modeling and numerical simulation of a 700 kW variable buoyancy controlled MCT for operation in a realistic environment of the Gulf Stream off the East Coast of Florida. A detailed turbine system is modeled, which includes the physical design, mathematical equations, and actuator models (i.e., generator and variable buoyancy). Simulation predictions of MCT performance are made for normal, hurricane, and fault conditions, e.g., rotor braking fault and blade pitch fault.

- We propose a novel spatiotemporal optimization problem for the MCT vertical

path planning operating in an uncertain oceanic environment to maximize the total harvested power of the system. Under this problem formulation, an RL-based method is designed to explore the optimal control actions, and results are compared with an MPC-based strategy. Moreover, an integrated path planning and tracking control framework is proposed, which includes a path planner that allocates an optimal path to maximize the harvested energy from the MCT using the RL approach; also, the path tracker is developed to track the optimal reference path commanded from the planner subject to the MCT dynamic model and problem constraints.

- We propose a turbine geometric/spatiotemporal control co-design to maximize the power-to-weight ratio of a buoyancy-controlled MCT and analyze the whole design from ocean currents to power generation to ensure that it is optimal. To formulate a bi-directional coupling between plant design and path control, a nested co-optimization framework, consisting of two optimization loops, i.e., an outer optimization loop responsible for the optimal design parameters and an inner optimization loop taking care of path planning, is proposed.

The following 12 papers are related to the work described in this thesis, where the first 9 are already published and the last 3 are under preparation at the time this dissertation is finished:

1. A. Hasankhani, J. VanZwieten, Y. Tang, B. Dunlap, A. De Luera, C. Sultan and N. Xiros, "Modeling and numerical simulation of a buoyancy controlled ocean current turbine," International Marine Energy Journal, vol. 4, no. 2, pp. 47-58, 2021.

2. A. Hasankhani, A. De Leura, J. VanZwieten, B. Dunlap, Y. Tang, C. Sultan and N. Xiros, "Numerical Simulation of A Buoyancy-Controlled Ocean Current Turbine," 2021 International Conference on Ocean Energy (ICOE), 2021.

3. A. Hasankhani, Y. Tang, J. VanZwieten and C. Sultan, "Ocean Current Turbine Active Depth Optimization for Maximum Power Production," 2021 International Conference on Ocean Energy (ICOE), 2021.

4. A. Hasankhani, Y. Tang, J. VanZwieten, and C. Sultan, "Comparison of deep reinforcement learning and model predictive control for real-time depth optimization of a lifting surface controlled ocean current turbine," in 2021 IEEE Conference on Control Technology and Applications (CCTA). IEEE, 2021, pp. 301–308.

5. A. Hasankhani, Y. Tang, J. VanZwieten and C. Sultan, "Spatiotemporal Optimization for Vertical Path Planning of an Ocean Current Turbine," IEEE Transaction on Control Systems Technology, 3rd Review (Conditionally Accepted).

6. A. Hasankhani, E. Ondes, Y. Tang, C. Sultan and J. VanZwieten, "Integrated Path Planning and Tracking Control of Marine Current Turbine in Uncertain Ocean Environments," 2022 American Control Conference (ACC), Accepted.

7. A. Hasankhani, Y. Tang, A. Synder, J. VanZwieten and W. Qiao, "Control Co-Design for Buoyancy-Controlled MHK Turbine: A NestedOptimization of Geometry and Spatial-Temporal Path Planning," 2022 Conference on Control Technology and Applications (CCTA), Accepted.

8. A. Hasankhani, Y. Tang, Y. Huang and J. VanZwieten, "Real-Time Vertical Path Planning Using Model Predictive Control for an Autonomous Marine Current Turbine," 2022 Conference on Control Technology and Applications (CCTA), Accepted.

9. A. Hasankhani, Y. Tang and J. VanZwieten, "Reinforcement Learning for Underwater Spatiotemporal Path Planning, with Application to an Autonomous

Marine Current Turbine," IEEE Robotics and Automation Letters, Submitted.

10. A. Hasankhani, J. VanZwieten, Y. Tang, C. Sultan and N. Xiros, "Modeling and Numerical Simulation of a Lifting Surface Controlled Ocean Current Turbine," Renewable Energy Journal. (Under preparation).

11. A. Hasankhani, Y. Tang and J. VanZwieten, "Integrated Path Planning and Tracking Control using Reinforcement Learning, with Application to a Marine Current Turbine," IEEE Transactions on Vehicular Technology. (Under preparation).

12. A. Hasankhani, Y. Tang and J. VanZwieten, "A Framework for Integrating Geometry, Path Planning, and Tracking Dynamics for the Control Co-Design of Marine Current Turbines," IEEE Transactions on Control Systems Technology. (Under preparation).

CHAPTER 2
LITERATURE REVIEW

In this chapter, we first present related work about modeling and numerical simulation of the MCT system, where we also review the technical design and in-water testing of moored MCT systems that have been conducted by both industry and academia. Then, we look at the literature on the suggested approaches for path planning of AUVs and autonomous renewable energy systems operating in a spatiotemporally varying environment. Finally, we describe the existing studies on the control co-design of the MHK turbines.

2.1 MODELING, NUMERICAL SIMULATION, AND TESTING OF MCT

Up until now, several variable buoyancy turbine designs have been proposed. A sample variable buoyancy controlled MCT designed by IHI Corporation is shown in Figure 2.1. The system developed and tested by the University of Naples [13] has counter-rotating propellers, variable buoyancy control, a unique v-tail configuration, and has been designed to generate the rated power of 100 kW at flow speeds of 2.8 m/s. A buoyancy controlled turbine with a rated power of 1.2 MW has been proposed in [14]. The air compressor proposed for this system has been designed to pump air, or another working fluid, in order to provide appropriate pressure. Recently, a 1/5th scale turbine named Floating Kuroshio Turbine (FKT) is being designed with the proposed corresponding full scale system of 20 kW at 1.5 m/s [15, 16]. This proposed FKT turbine includes two rotors and a foil float with two aft- and two

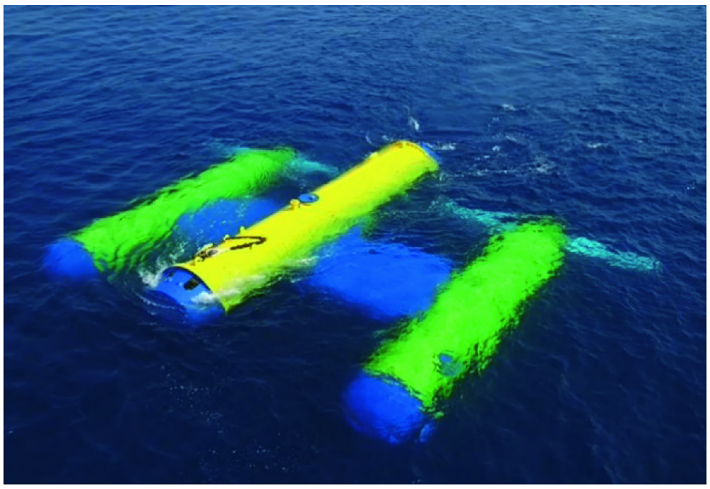

Figure 2.1: Example of a buoyancy-controlled MCT that has counter-rotating rotor blades with a single variable buoyancy module. Image credit IHI Inc. [12, 27].

fore-buoyancy engines, so the float (i.e., buoyancy engine) is responsible for providing variable buoyancy.

2.1.1 Numerical Simulation of MCT

Numerical simulations of moored turbines have also been developed, along with control system technologies. A pitch controller has been designed for harnessing constant power while minimizing thrust of MCT system [28,29]. Numerical tools have been developed and evaluated for single- and dual-rotor MCTs with mooring cables that are designed for operation in the deep waters of the Gulf Stream [30]. The motion of the MCT system has also been simulated considering real conditions [31] and controlled using pitch control [32] by the University of Tokyo. Moreover, the dynamic motion of a floating type MCT (i.e., contra-rotating MCT) and a twin-rotor type MCT have been simulated [33], where the numerical model of the twin-rotor type MCT has been described using 6-DOF [34] and its transient movement [35], as well as the movement during rotor rotation initiation and during system failures [36]. The numerical simulation of the MCT system has been addressed in [37, 38] without considering any

feedback or fault in their MCT model. In addition, the numerical model of an MCT system using wing-like surfaces [39] and blade pitch control [40] has been preliminary explored.

2.1.2 In-water Testing of MCT

The technical design and in-water testing of moored MCT systems have been conducted by both industry and academia. The first on-site prototype testing for turbines designed to operate in deep water offshore currents was the Vertical Axis Hydro Turbine, which was developed by Nova Energy Limited and the National Research Council of Canada [41,42]. This MCT was successfully tested from an anchored vessel in the Gulf Stream during a one-day mission in April, 1985. Aquantis spent nearly a decade developing variants of its 2.5 MW C-plane, dual-rotor turbine designed to extract energy from the Gulf Stream [17], with two separate moored prototype tests conducted in towing tanks [39, 43]. Anadarko successfully tested their MCT system in the Gulf of Mexico, producing approximately 12 kW of shaft power with a 1/5th scale system [44]. This proposed system uses an induction generator with fin-ring propellers. In 2017, IHI Corporation began testing an MCT in the Kuroshio current off Japan that uses a dual-rotor, 100 kW turbine system to capture kinetic energy [12,45].

In 2020, three different MCTs were tested in Gulf Stream during a multi-day mission designed to verify the capability of producing electricity over a 24-hour period [46]. In addition, National Taiwan University built an 800 W (1/5th scale) test apparatus model placed in a towing tank, which was also successfully tested in the open water of the Kuroshio Current [47]. This test quantified the hydrodynamic performance by establishing values for the rotor rotation speed, torque, and thrust. Further, National Taiwan University did a towing test on a 1/25th scale FKT turbine at the towing tank to quantify the torque, power, and thrust coefficients [15]. Another towing test was done in Kuroshio currents, while the 1 kW turbine was attached to a

small boat and towed to simulate the ocean currents [24]. In addition, the next phase of testing on the designed turbine was done to find both the operation of the mooring system and impacts of waves on the turbine, which was tested at a circulating water channel (length = 48 m, width = 4 m, and depth = 1.67 m) using the wave-making facilities with the flow speed of 2 m/s, and the maximum wave height of 0.3 m [48].

2.1.3 Previously Developed Simulation Algorithms for Our Designed MCT

The numerical modeling specifically in line with our designed MCT system has been addressed in a series of publications focused on system dynamics and environmental conditions. The initial mathematical modeling approach has been used to describe the dynamics of a nearly neutrally buoyant 20 kW MCT, where the mooring cable is not attached to the sea floor but instead is assumed to be a part of a larger mooring system [37]. The study has used a 7 degree of freedom model to assess both linear and angular displacements of the MCT, in addition to the states associated with the cable model. Furthermore, the model has considered kinematics, equations of motion, hydrostatics, rotor forces, streamline body forces, cable force, and included a wave model. The hydrodynamic loads on this 3-meter diameter rotor blade have been calculated using a blade element momentum approach with a dynamic wake inflow model, using 3D lift and drag coefficients. These 3D lift and drag coefficients have been calculated using Xfoil [49] then AirfoilPrep [50] based on the hydrofoil shapes of a rotor blade. Wave effects on calculated turbine forces have been based on the wave induced orbital water velocities. The utilized wave spectrum has been defined as the product of a Pierson-Moskowitz frequency spectrum and a directional spreading function. Each element of a mooring cable has been modeled as a linear element with forces determined by velocity and position of its end nodes using finite element lumped mass approach. Cable forces have been calculated considering buoyancy, hydrodynamic drag, gravity, and internal strain.

The same modeling process has been enhanced to simulate a 700 kW MCT to develop the use of variable blade pitch control for regulating position and attitude [40]. Airfoil shapes for the new rotor blade have been selected using HARP-Opt, and FX-83-W airfoils are found as the best design for this MCT based on power production when compared with numerous other airfoil shapes. On the other hand, all of the lengths, areas, volumes & masses, and moments of inertia are multiplied by 20/3, $(20/3)^2$, $(20/3)^3$, and $(20/3)^5$ compared to numbers presented in [37]. In addition, effects of variable blade pitch are simulated, i.e., effects of the individual blade root angles are considered in the angle of attack calculations and when determining the reduced flow rate [40]. Hence, the momentum portion of the blade element model determines the blade root angle according to the last rotor blade to pass its location. In addition, the open- and closed-loop flight controller is applied to move this MCT, which operates according to harmonic oscillations of blade root angles [40, 51].

The turbulence model used in chapter 3 has been originally presented in [52]. This model calculates turbulent flow perturbations in time domain, so the free-stream water velocity at each node, where hydrodynamic forces are calculated, is formulated as the sum of current induced velocity, wave induced velocity, and turbulence induced velocity. This approach is accounted for the temporal, spatial, and directional correlations of turbulence over all numerically modeled components.

2.2 PATH PLANNING FOR AUV & AUTONOMOUS RENEWABLE ENERGY SYSTEMS

Path planning is studied for many applications, such as AUV and autonomous renewable energy systems operating in spatiotemporally varying environments, which are insightful for our study. These works have been reviewed in this section, where the candidate approaches are introduced to solve this optimization problem. Finally, the suggested integrated path planning and tracking for similar applications have been

reviewed.

It should be mentioned that an efficient path control has entailed with optimized ultimate goals (such as a collision-free optimal path [53, 54], minimized path length [55], minimized consumed time path [56], minimized energy consumption [57], maximized harnessed energy [58], etc). In our thesis, the primary goal of an autonomous MCT is to find the path (i.e., operation depth) that maximizes the harnessed power from the ocean current since the ocean current speed is depth-dependent and time-varying.

2.2.1 Path Planning for AUV

In the field of autonomous agents path planning, an AUV has gained increasing attention due to its complexity, and lack of human accessibility. The AUV systems have been primarily used for searching and investigation in the underwater environment, implying minimized power consumption and travel time [59]. Graph search methods, including Dijkstra's algorithm [60], A* algorithm [61], and D* algorithm [62], are classical path planning approaches to address the graph constructed by the discretized environment, which are fast but suffering from lower precision due to discretization and computational complexity in the high-dimensional environment [63]. On the other hand, popular planning approaches for continuous environment rely on heuristic algorithms [64], learning-based methods [65], and predictive algorithms [66].

The path planning problem becomes more complicated when the autonomous vehicles operating in a spatiotemporally varying environment [59,67–69]. A vast literature is devoted to addressing an independent task of path planning for AUV applications. For example, an estimator is designed to predict the spatially dependent ocean velocity, and trajectory planning is further developed to determine the location of an AUV applied as an energy harvester [70]. Trajectory planning of AUVs is addressed to avoid collisions in the presence of dynamic obstacles [71] and to reduce expected

cost [72]. Transoceanic gliders treated as AUVs are studied, aiming to a decreased battery consumption on long-duration missions [73]. Bayesian optimization is used to specify the configuration and location of an MCT array to maximize harvested energy [22]; however, the research is focused on the economic side and a more detailed and realistic model is desired.

2.2.2 Path Planning for Autonomous Renewable Energy Systems

Recently, the path planning is applied for the emerging field of energy-harvesting autonomous vehicles, such as an airborne energy system [74, 75] and ocean kite [10]. In these applications, the classical path planning algorithms, i.e., graph searching techniques designed originally for the autonomous agents operating in a static gridded environment [61, 62], are not adequate in a spatiotemporally varying environment. Hence, it is intuitive to develop an approach to fit a particular task of seeking an optimal path in an environment with enhanced space-time uncertainties.

The first attempts to address the path planning problem for autonomous renewable energy agents have been devoted to the airborne energy system, where an extremum seeking approach [75] and MPC method [25] have been proposed to find a sequence of optimal waypoints. Similar problem has been then formulated in the context of the energy-harvesting ocean kite [10] addressed through the MPC approach.

2.2.3 Candidate Approaches for Path Planning

Among many approaches to address real-time vertical path planning, extremum seeking, MPC, and RL are gaining increasing attention in recent years due to their success in both academia and industry. These approaches can be justified with a classical path planning algorithm, e.g., A* algorithm, that is extensively studied for the autonomous vehicles' path planning, particularly the AUV [61, 76]. The extremum seeking approach is applied to deal with the path planning of similar research to our

problem, such as airborne wind energy systems [75, 77, 78] and AUVs [79–82].

To address the path planning for autonomous vehicles in a dynamic environment, MPC-based approaches are applied to determine the optimal path and operation mode of vehicles [66, 83, 84]. A spatial-based path planning method for autonomous vehicles is introduced in [85], verifying autonomous driving in an obstacle-free environment and in the presence of obstacles. For a specific application of the airborne wind energy system, MPC-based techniques are employed to set the optimal altitude [25, 86], in which the future wind speeds are predicted and the output power is optimized by changing the location of the system to access the optimal velocities. An MPC-based real-time navigation optimization has been proposed for the AUVs to minimize the squared distance from the target state [87]. A coupled sample-based path planning with MPC has been used to simultaneously seek the optimal actuators and path for the AUV [88].

On the other hand, the path planning of autonomous vehicles is applied through RL approaches considering safety, security, and communication issues [89]. An RL-based path planning of mobile robots with obstacles is proposed to avoid collision and determine the optimal path through identifying environmental spatiotemporal data [90, 91]. To realize the minimum power consumption for plug-in hybrid electric vehicles, path planning and energy management are addressed through an RL-based approach [92]. However, due to the error induced by the prediction modeling, spatiotemporal uncertainties, etc. [11], the feasibility and robustness of these methods applied to MCT vertical path planning are not investigated. To incorporate the uncertainties into the control planning frameworks, a Gaussian process (GP) approach can be employed, such as applying the GP for modeling probabilistic dynamics in RL [93, 94], as well as using the numerical GP approach to model the uncertainty associated with noisy data for partial differential equations [95].

2.2.4 Integrated Path Planning and Tracking

An integrated framework for path control, contributing to a single complex task of path planning and tracking, represents a possible solution to the highly nonlinear dynamic systems operating in an inherent stochastic environment. Such a framework deals with high-level path planning and low-level path tracking in real time, subject to nonholonomic constraints. As an instance from the proposed frameworks, a multiconstrained model predictive control (MMPC) has been developed to construct a collision-free path for autonomous driving and successfully follow the path [66]. An integrated path planning and tracking for an AUV has been proposed in [96] following a spline path defined due to AUV's dynamic. Deep reinforcement learning (DRL), as an approach in the machine learning area highly applied for autonomous control applications, has been demonstrated impressive results in the field of path control. For example, DRL has been applied to address collision avoidance as a path planning task and path following for the AUV in the presence of stationary obstacles [97, 98] and a complex layout of dynamic obstacles [99]. For a similar application of AUV, path planning and tracking has been developed in a bi-level framework taking advantage of DRL in both levels [100], thereby enabling more complicated planning objectives but increasing the complexity and simulation time.

2.3 CONTROL CO-DESIGN OF MHK SYSTEMS

The controller should be designed to complement the physical system design as an approach named control co-design [101], thereby limiting adverse effects on the system efficiency, cost, and stability. The control co-design, integrated design process that has been followed is a so-called *wave to wire* design in wave energy conversions [7,102–105]. There exist limited literature on the co-design of the MHK energy system, such as an ocean kite [26]; however, to the best of our knowledge, it is the first time in this thesis that the co-design problem is investigated for the MCT system.

CHAPTER 3

MODELING OF BUOYANCY CONTROLLED MCT

Increased global renewable power demands and the high energy density of ocean currents have motivated the development of MCTs. Compliant mooring systems will be used together with variable buoyancy, lifting surface, sub-sea winches, and/or surface buoys to maintain desired near-surface operating depths. This chapter presents a complete numerical simulation of a 700 kW variable buoyancy controlled MCT that includes a detailed turbine system, mathematical modeling, equations of motion, and actuator (i.e., generator and variable buoyancy) modeling. Simulation predictions of MCT performance are made for normal, hurricane, and fault scenarios. Results suggest this MCT can operate between depths of 38 m to 90 m for all homogeneous flow speeds between 0.5 m/s $-$ 2.5 m/s. Fault scenarios show that rotor braking faults will result in a rapid vertical MCT system assent and blade pitch faults will create power fluctuations apparent in the frequency domain. Finally, the MCT power statistics and system behaviors are quantified under typical and extreme operations using measured ocean currents with normal and hurricane conditions.

In summary, our main contribution in this chapter is to model and simulate a 700 kW buoyancy controlled MCT, where we detail the mathematical models of key components and carries out a preliminary dynamic analysis of the system. The developed model in this work addresses a fundamental challenge for the marine hydrokinetic community and meanwhile opens a new research frontier to the control community to address the control requirements for the designed MCT.

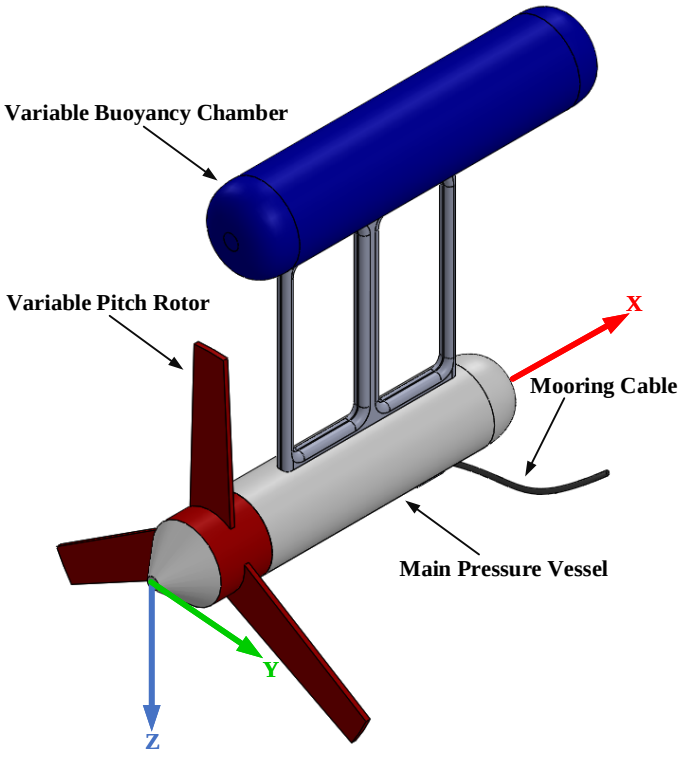

Figure 3.1: Schematic of the numerically simulated buoyancy controlled marine current turbine (MCT).

3.1 MECHANICAL DESIGN AND MATHEMATICAL MODELING OF MCT

The developed high-fidelity numerical simulation platform has many similarities to the 700 kW, 3-blade horizontal axis MCT turbine design from [40], which also has many geometric and inertial characteristics scaled from a 20 kW experimental MCT located at Southeast National Marine Renewable Energy Center (SNMREC) [106, 107]. In this chapter, we detail the numerically modeled MCT specifications and present new simulation advancements. These new modeling advancements include environmental models that utilize ocean current measurements and actuator models. A representative sketch of this system is provided in Figure 3.1 to show the relative scale and location of the primary MCT components.

3.1.1 Overview of the Modeled and Simulated MCT

The investigated MCT system is a representative design with the basic features necessary for operation in the Gulf Stream current off Florida's East Coast. The designed 700 kW system has a single 20 m diameter variable pitch rotor, which is described in detail in [40]. Its geometric and inertial parameters are set to those in [40] which are scaled from the 20 kW turbine presented in [37], besides those of the variable buoyancy chamber which replaces the "buoyancy compensation modules" in previous nearly neutrally buoyant designs.

The dimensions of this MCT are presented here, with all locations and moments of inertia referenced to the center of rotation of the rotor (i.e., coaxial with the rotor shaft) at its front surface. Provided moments of inertia values for the entire MCT assume the variable buoyancy tanks are empty (i.e., do not contain water) and are $I_{xx} = 1.35 \times 10^7$ kgm^3, $I_{yy} = 4.74 \times 10^7$ kgm^3, and $I_{zz} = 3.45 \times 10^7$ kgm^3. Moreover, the total mass is 4.98×10^5 kg without considering ballast water. The variable buoyancy chamber is divided internally into two separate buoyancy tanks, each with 3.20×10^4 kg (31.251 m^3) of variable ballast. These ballast tanks are sized such that the MCT achieves an operating depth near 50 m (50.4 m) when each ballast tank is half filled with water in a homogeneous current speed of 1.6 m/s.

The center of the collective fixed and variable ballast tank (i.e., the variable buoyancy chamber) is located at $x = 9.58$ m, $y = 0$ m, and $z = -15.34$ m, and it has an overall length of 20.00 m and a diameter of 4.45 m. This MCT is 90 kN positively buoyant when the ballast tanks are filled with water and 718 kN when they are filled with air. The main pressure vessel that houses the generator, gearbox, and electronics is aligned with the rotor and has a length and diameter of 14.76 m and 3.98 m respectively. In addition, the single 607 m long mooring cable has a diameter of 0.16 m, slightly smaller than the 0.20 m diameter double-armor umbilical suggested for a 5 MW offshore wind turbine [108]. The resulting displaced mass of this cable

based on its geometry is 20.6 kg/m, and a mass of 46 kg/m is assumed based on the average density of a double-armor umbilical suggested for offshore wind in [108]. This cable is attached to the MCT at the location $x = 11.85$ m, $y = 0$ m, and $z = 3.00$ m so that a near zero pitch angle is achieved (1.1°) when both buoyancy tanks are half filled with water in a homogeneous flow speed of 1.6 m/s.

3.1.2 Mathematical Modeling of MCT

The investigated MCT system is modeled with 14 states X, consisting of the position $\eta = [x\ y\ z\ \phi\ \theta\ \psi]^T$ and the velocity of the MCT system $\mathcal{V} = [u\ v\ w\ p^b\ q\ r]^T$; two remaining states of the MCT system are the angular velocity of the rotor p^r, and rotation angle of the rotor blade ϕ^r, thereby symbolizing the state vector by $X = [\eta\ \mathcal{V}\ p^r\ \phi^r]^T$.

Kinematics and Coordinate Frame: To derive the equations of motion for the MCT system, five coordinate frames are used, including (i) an inertial coordinate frame ($\mathcal{O}_I$), (ii) a body-fixed coordinate frame ($\mathcal{O}_B$), (iii) a momentum mesh coordinate frame ($\mathcal{O}_M$), (iv) a shaft coordinate frame ($\mathcal{O}_S$), and (v) a rotor blade coordinate frame ($\mathcal{O}_R$) [109]. The transformation matrix from the inertial coordinate frame ($\mathcal{O}_I$) to the body-fixed coordinate frame ($\mathcal{O}_B$), $L_{\mathcal{O}_I}^{\mathcal{O}_B}$, is defined as follows [110]:

$$L_{\mathcal{O}_I}^{\mathcal{O}_B} = \begin{bmatrix} c_\psi c_\theta & s_\psi c_\theta & -s_\theta \\ c_\psi s_\theta s_\phi - s_\psi c_\phi & c_\psi c_\phi + s_\psi s_\theta s_\phi & c_\theta s_\phi \\ c_\psi s_\theta c_\phi - s_\psi s_\phi & -c_\psi s_\phi + s_\psi s_\theta c_\phi & c_\theta c_\phi \end{bmatrix} \tag{3.1}$$

where $s_{(.)} = sin(.)$ and $c_{(.)} = cos(.)$.

Equations of Motion: Given that the motion of the MCT system is defined in $\mathcal{O}_B$, instead of the rotation about the x-axis, the location of the center of gravity and center of buoyancy of the MCT system are represented by $r_G = [x_G\ y_G\ z_G]^T$ and $r_B = [x_B\ y_B\ z_B]^T$, respectively. A set of twelve equations of motion are reduced to the seven equations representing an MCT system with 7-DOF [109], with 6-DOF

describing the main body's rotation,

$$m(\dot{u} - vr + wq) - mx_G(q^2 + r^2) + m^b z_G^b(p^b r + \dot{q}) = F_x \tag{3.2}$$

$$m(\dot{v} + ur) - w(m^b p^b + m^r p^r) + m^b z_G^b(q^r - \dot{p}^b) + m^b x_G^b q p^b + m^r x_G^r q p^r + m x_G \dot{r} = F_y \tag{3.3}$$

$$m(\dot{w} - uq) + v(m^b p^b + m^r p^r) + m^b z_G^b(p^{b^2} + q^2) + m^b x_{cg}^b r p^b + m^r x_G^r r p^r + m x_G \dot{q} = F_z \tag{3.4}$$

$$-m^b z_G^b(\dot{v} - wp^b + ur) + I_x^r \dot{p^r} + qr(I_z^r - I_y^r) = M_x + \tau_{\text{em}} \tag{3.5}$$

$$\begin{aligned} &I_y \dot{q} + rp^b(I_x^b - I_z^b) + rp^r(I_x^r - I_z^r) + I_{xz}^b(p^{b^2} - r^2) + m^b z_G^b(\dot{u} - vr + wq) \\ &- mx_G(\dot{w} - uq) + m^b x_G^b v p^b - m^r x_G^r v p^r = M_y \end{aligned} \tag{3.6}$$

$$\begin{aligned} &I_z \dot{r} + qp^b(I_y^b - I_x^b) + qp^r(I_y^r - I_x^r) + I_{xz}^b(rq - \dot{p}^b) + mx_G(\dot{v} + ur) - m^b x_G^b w p^b \\ &- m^r x_G^r w p^r = M_z \end{aligned} \tag{3.7}$$

and the last DOF representing the rotor's rotation about the x-axis:

$$\dot{p^r} = \frac{M_x^r - \tau_{\text{em}} - qr(I_z^r - I_y^r)}{I_x^r} \tag{3.8}$$

where $F_{(.)}$ denotes the force; $M_{(.)}$ is the moment; $(.)_x$, $(.)_y$, and $(.)_z$ are the portion $(.)$ about $x-$, $y-$, and $z-$ axes; $(.)^r$ and $(.)^b$ denote the rotor and body portions; τ_{em} denotes the electromechanical torque. The mass $m^{(.)}$, the moment of inertia $I^{(.)}$, and the center of gravity $(.)_G$ are defined with respect to both the actual inertial properties and added inertial properties of the MCT (denoted as *virtual* in [109]).

Finally, these equations of motion can be summarized in a matrix form as presented in (3.9).

The total external forces acting on the MCT, F, consists of forces due to gravitational and buoyancy forces, rotor force, body force, variable buoyancy force, and tether force, namely:

$$F = F^{GB} + F^r + F^b + F^{vb} + F^t \tag{3.10}$$

$$\dot{\mathcal{V}} = \begin{bmatrix} m & 0 & 0 & 0 & m^{\mathrm{b}} z_{\mathrm{G}}^{\mathrm{b}} & 0 \\ 0 & m & 0 & -m^{\mathrm{b}} z_{\mathrm{G}}^{\mathrm{b}} & 0 & m x_{\mathrm{G}} \\ 0 & 0 & m & 0 & -m x_{\mathrm{G}} & 0 \\ 0 & -m^{\mathrm{b}} z_{\mathrm{G}}^{\mathrm{b}} & 0 & I_x^{\mathrm{b}} & 0 & -I_{xz}^{\mathrm{b}} \\ m^{\mathrm{b}} z_{\mathrm{G}}^{\mathrm{b}} & 0 & -m x_{\mathrm{G}} & 0 & I_y & 0 \\ 0 & m x_{\mathrm{G}} & 0 & -I_{xz}^{\mathrm{b}} & 0 & I_z \end{bmatrix}^{-1} \begin{bmatrix} F_x + m(vr - wq) + m x_{\mathrm{G}} (q^2 + r^2) - m^{\mathrm{b}} z_{\mathrm{G}}^{\mathrm{b}} p^{\mathrm{b}} r \\ F_y - mur + w \left(m^{\mathrm{b}} p^{\mathrm{b}} + m^{\mathrm{r}} p^{\mathrm{r}} \right) - m^{\mathrm{b}} z_{\mathrm{G}}^{\mathrm{b}} qr \\ -m^{\mathrm{b}} x_{\mathrm{G}}^{\mathrm{b}} qp^{\mathrm{b}} - m^{\mathrm{r}} x_{\mathrm{G}}^{\mathrm{r}} qp^{\mathrm{r}} \\ F_z + muq - v \left(m^{\mathrm{b}} p^{\mathrm{b}} + m^{\mathrm{r}} p^{\mathrm{r}} \right) + m^{\mathrm{b}} z_{\mathrm{G}}^{\mathrm{b}} \left(p^{\mathrm{b}2} + q^2 \right) \\ -m^{\mathrm{b}} x_{\mathrm{G}}^{\mathrm{b}} rp^{\mathrm{b}} - m^{\mathrm{r}} x_{\mathrm{G}}^{\mathrm{r}} rp^{\mathrm{r}} \\ M_x + \tau_{\mathrm{em}} - qr \left(I_z^{\mathrm{b}} - I_y^{\mathrm{b}} \right) + I_{xz}^{\mathrm{B}} p^{\mathrm{b}} q \\ -m^{\mathrm{b}} z_{\mathrm{G}}^{\mathrm{b}} \left(wp^{\mathrm{b}} - ur \right) \\ M_y - rp^{\mathrm{b}} \left(I_x^{\mathrm{b}} - I_z^{\mathrm{b}} \right) - rp^{\mathrm{r}} \left(I_x^{\mathrm{r}} - I_z^{\mathrm{r}} \right) - I_{xz}^{\mathrm{b}} \left(p^{\mathrm{b}2} - r^2 \right) \\ +m^{\mathrm{b}} z_{\mathrm{G}}^{\mathrm{b}} (vr - wq) - m x_{\mathrm{G}} uq + m^{\mathrm{b}} x_{\mathrm{G}}^{\mathrm{b}} vp^{\mathrm{b}} + m^{\mathrm{r}} x_{\mathrm{G}}^{\mathrm{r}} vp^{\mathrm{r}} \\ M_z - qp^{\mathrm{b}} \left(I_y^{\mathrm{b}} - I_x^{\mathrm{b}} \right) - qp^{\mathrm{r}} \left(I_y^{\mathrm{r}} - I_x^{\mathrm{r}} \right) - I_{xz}^{\mathrm{b}} rq \\ -m x_{\mathrm{G}} \ \mathrm{u} \ r + m^{\mathrm{b}} x_{\mathrm{G}}^{\mathrm{b}} wp^{\mathrm{b}} + m^{\mathrm{rv}} x_{\mathrm{G}}^{\mathrm{r}} wp^{\mathrm{r}} \end{bmatrix} \tag{3.9}$$

Similarly, the total moment acting about the center of mass of the MCT is equal to the sum of moments due to buoyancy moment, rotor moment, body moment, variable buoyancy moment, and tether moment, as follows:

$$M = M^B + M^r + M^b + M^{vb} + M^t \tag{3.11}$$

The forces and moments acting on the MCT system are defined through the hydrostatics, hydrodynamic, and tether forces in the following sections.

Hydrostatics: The MCT experiences hydrostatic forces and moments as a result of the system's buoyancy and weight, thereby formulating the gravitational and buoyancy forces F^{GB} as follows:

$$F^{GB} = F^G + F^B = L_{\mathcal{O}_I}^{\mathcal{O}_B} \begin{bmatrix} 0 \\ 0 \\ mg + \nu^{vb}(1 - b_{\mathrm{f}})\rho g + \nu^{vb}(1 - b_{\mathrm{a}})\rho g \end{bmatrix} + L_{\mathcal{O}_I}^{\mathcal{O}_B} \begin{bmatrix} 0 \\ 0 \\ -B \end{bmatrix} \tag{3.12}$$

where m is the total mass of the MCT not including buoyancy water, g is the earth gravitational acceleration, ν^{vb} is the volume of each variable buoyancy tank, b_{f} and b_{a} denote the forward and aft buoyancy tanks fill fractions, ρ is the water density, and B is the total buoyancy force.

The hydrostatic moment induced by the buoyancy moment M^B is formulated by:

$$M^B = r_{BG} \times F^B = (r_B - r_G) \times F^B \tag{3.13}$$

Here, $\times$ denotes the cross multiplication. r_{BG} denotes a vector from the center of gravity to the center of buoyancy. Assuming a constant center of buoyancy r_B and a variable center of gravity due to the changes of water in the variable buoyancy tanks:

$$r_G = \frac{r_G m + r_G^f \nu^{vb}(1 - b_{\mathrm{f}})\rho g + r_G^a \nu^{vb}(1 - b_{\mathrm{a}})\rho g}{m + \nu^{vb}(1 - b_{\mathrm{f}})\rho + \nu^{vb}(1 - b_{\mathrm{f}})\rho} \tag{3.14}$$

where r_G^f and r_G^a are the center of the gravity of the forward buoyancy tank and aft buoyancy tank, respectively.

Hydrodynamic: The hydrodynamic forces and moments are utilized for the MCT system due to the pressure of the surrounding fluid (i.e., ocean water) and forces acting on the rotor blade.

Assuming the MCT system as a streamlined body, the axial drag and tangential drag of the body are calculated; accordingly, the forces acting on the body are formulated as follows, where body is evenly divided into N_b discrete sections along its length:

$$F^b = \begin{bmatrix} -\frac{1}{2N_b}\rho c_a^b A_a^b \sum_{i=1}^{N_b} u_c^i V^i \\ -\frac{1}{2N_b}\rho c_t^b A_t^b \sum_{i=1}^{N_b} v_c^i V^i \\ -\frac{1}{2N_b}\rho c_t^b A_t^b \sum_{i=1}^{N_b} w_c^i V^i \end{bmatrix} \tag{3.15}$$

where c_a^b and c_t^b are the axial drag coefficient and the tangential drag coefficient for the body, respectively; A_a^b is the body frontal area, $A_t^b = d^b l^b$ is the crossflow area. u_c, v_c, and w_c denote zonal, meridional, and vertical portions of the ocean velocity V.

The hydrodynamic moment on the body is defined by:

$$M^b = r^b \times F^b \tag{3.16}$$

where r^b denotes the location vector from the center of gravity to the hydrodynamic center of the body.

In a similar approach, the hydrodynamic forces and moments for the variable buoyancy tank are written as follows:

$$F^{vb} = \begin{bmatrix} -\frac{1}{2N_{vb}}\rho c_a^{vb} A_a^{vb} \sum_{i=1}^{N_{vb}} u_c^i V^i \\ -\frac{1}{2N_{vb}}\rho c_t^{vb} A_t^{vb} \sum_{i=1}^{N_{vb}} v_c^i V^i \\ -\frac{1}{2N_{vb}}\rho c_t^{vb} A_t^{vb} \sum_{i=1}^{N_{vb}} w_c^i V^i \end{bmatrix} \tag{3.17}$$

$$M^{vb} = r^{vb} \times F^{vb} \tag{3.18}$$

where $(.)^{vb}$ denotes the variable buoyancy portion, and r^{vb} denotes the location vector from the center of gravity to the hydrodynamic center of the variable buoyancy tank.

The rotor force is calculated using a blade element momentum (BEM) rotor model describing the wake inflow model, calculated as follows:

$$F^r = \sum_{j=1}^{N_r} \sum_{i=1}^{N} L_{\mathcal{O}_S}^{\mathcal{O}_B} L_{\mathcal{O}_R}^{\mathcal{O}_S} \begin{bmatrix} \frac{1}{2}\rho A_a^{r,i} c_a^{r,ij} ((V_a^{ij})^2 + (V_t^{ij})^2) \\ 0 \\ \frac{1}{2}\rho A_t^{r,i} c_t^{r,ij} ((V_a^{ij})^2 + (V_t^{ij})^2) \end{bmatrix} \tag{3.19}$$

where $L_{\mathcal{O}_S}^{\mathcal{O}_B}$ is the transformation matrix from $\mathcal{O}_S$ to $\mathcal{O}_B$, $L_{\mathcal{O}_R}^{\mathcal{O}_S}$ denotes the transformation matrix from $\mathcal{O}_R$ to $\mathcal{O}_S$, A_a^r and A_t^r are the frontal and crossflow areas of the rotor, respectively; c_a^r and c_t^r are axial and tangential drag coefficients for the rotor.

The axial and tangential drag coefficients are calculated as follows:

$$\begin{aligned} c_a^r &= c_L \cos\phi + c_D \sin\phi \\ c_t^r &= c_L \sin\phi + c_D \cos\phi \end{aligned} \tag{3.20}$$

where c_L and c_D are lift and drag coefficients, which are functions of an angle of attack $\alpha = \phi - \gamma$. Given that the relative flow angle is $\phi = \tan^{-1}\frac{V_a}{V_t}$ and γ is the blade pitch angle.

The hydrodynamic moment on the rotor is expressed by:

$$M^r = r^r \times F^r \tag{3.21}$$

where r^r denotes the location vector from the center of gravity to the hydrodynamic center of the rotor.

Tether force: The final set of forces acting on the MCT system is tether force, formulated as [37]:

$$F^t = \frac{EA^c s}{l^c} H + \frac{c_i^c s}{l^c} H - \frac{\rho d^c l^c}{4} K + L_{\mathcal{O}_I}^{\mathcal{O}_B} \frac{(\rho^c - \rho) g \pi d^{c2} l^c}{8} \begin{bmatrix} 0 & 0 & 1 & 0 & 0 & 1 \end{bmatrix}^T \tag{3.22}$$

with

$$H = \begin{bmatrix} 0 & 0 & 0 & 0 & 0 & 0 \\ 0 & 0 & 0 & 0 & 0 & 0 \\ 0 & 0 & -1 & 0 & 0 & 1 \\ 0 & 0 & 0 & 0 & 0 & 0 \\ 0 & 0 & 0 & 0 & 0 & 0 \\ 0 & 0 & 1 & 0 & 0 & -1 \end{bmatrix}, K = \begin{bmatrix} \frac{c_a^c f_a^c (v_r^a)^2 v_n^a}{\sqrt{(v_n^a)^2 + (v_b^a)^2}} \\ \frac{c_a^c f_a^c (v_r^a)^2 v_n^a}{\sqrt{(v_n^a)^2 + (v_b^a)^2}} \\ c_a^c f_t^c v_r^a \mid v_r^a \mid \\ \frac{c_a^c f_a^c (v_r^b)^2 v_n^b}{\sqrt{(v_n^b)^2 + (v_b^b)^2}} \\ \frac{c_a^c f_a^c (v_r^b)^2 v_n^b}{\sqrt{(v_n^b)^2 + (v_b^b)^2}} \\ c_a^c f_t^c v_r^b \mid v_r^b \mid \end{bmatrix} \tag{3.23}$$

where A^c denotes the crossflow area of the cable, s is the cumulative stretch vector, c_i^c denotes the internal damping coefficient, ρ^c is the cable density, c_a^c denotes the axial drag coefficient for cable, f_a^c and f_t^c are the axial and tangential hydrodynamic loading functions for the cable.

3.2 MCT ACTUATOR MODELING

This section presents the actuator models, including the generator model and variable buoyancy model.

Generator Model: The model used to describe the dynamics of the generator in the MCT is given by [111]:

$$\begin{cases} \tau_{\text{em}}(s) / \tau(s) = \alpha / (s + \alpha) \\ \\ P_{gen}(t) = \eta \omega(t) \tau_{\text{em}}(t) \end{cases} \tag{3.24}$$

where α dictates the response time based on generator rated power, P_{gen} denotes the generator power, ω is the rotational speed of generator, and η denotes the efficiency of the generator. For this simulation $\alpha = 700$ for the 700 kW MCT and $\eta = 0.98$.

Variable Buoyancy Model: The variable buoyancy system has two separate variable buoyancy tanks. Each tank can hold 31.251 m^3 of air/water, and is sufficiently baffled such that the center of mass of ballast in each tank is not dependent on the orientation of the MCT. This system model is developed to predict ballast pump power usage and to provide reasonable limits on the rate at which water can be transferred into or out of these tanks.

This model assumes that a pump drives water through an opening such that the pressure in the tank is at vacuum pressure (i.e., $P_{\text{abs}} \cong 0$ kPa). Using this approach very little power is used (i.e., $P^{\text{fill}} \cong 0$) when the tanks are being filled with water, since this can be driven by the natural pressure difference between ambient pressure and vacuum pressure. The power required to pump sea water out of the tank can be calculated using pressure, volumetric flow rate Q_{B}, and pump efficiency:

$$P_{\text{B}}^{\text{fill}} = 0 \tag{3.25}$$

$$P_{\text{B}}^{\text{empty}} = \frac{P \cdot Q_{\text{B}}}{\eta_{\text{pump}}} \tag{3.26}$$

where $\eta_{\text{pump}} = 0.75$ is the pump efficiency, $P = P_{\text{atm}} + P_{\text{HS}}$. Assuming P_{atm} is atmospheric pressure (101 kPa) and P_{HS} is hydrostatic pressure ($P_{\text{HS}} = \rho.g.z$), where $g = 9.81$ m/s^2 is gravity. P_B^{empty} can be rewritten as:

$$P_{\text{B}}^{\text{empty}} = \frac{(101 + 10.1z)Q_{\text{B}}}{0.75} \tag{3.27}$$

To find reasonable limits for the volumetric flow rates of water as a function of depth this can be re-written as:

$$Q_{\text{B}} = \frac{0.75P_{\text{B}}^{\text{empty}}}{101 + 10.1z} \tag{3.28}$$

Assuming a ballast pump power for each ballast tank that is equal to that of WWII era submarines [112] of $P_{\mathrm{B}}^{\mathrm{empty}} = 18.8$ kW, a volumetric flow rate Q_B of 0.023 m^3/s is achieved at a depth of 50 m. Since each of the two ballast tanks has a volume of 31.251 m^3, these tanks can be completely emptied in 22.2 minutes at this depth, with a total energy usage of 14.02 kWh that is independent of the fill rate.

3.3 SIMULATION RESULTS

To help quantify buoyancy controlled MCT performance, numerical simulations are conducted for a variety of conditions. MCT operating range is predicted for different flow conditions, system response to both an actuator and rotor faults are evaluated, and system performances in measured open ocean currents are quantified.

3.3.1 MCT Operating Range Assessment

The operating range of MCTs will be important for operating in the most energy dense resources, operating beneath surface waves in storm conditions, and surfacing for maintenance. Therefore, we quantify MCT operating range for two simplistic flow conditions, a homogeneous flow field and a current that linearly decreases with depth (i.e., shear flow), each matched with two operating scenarios. These operating scenarios include maximizing/minimizing depth regardless of MCT pitch angle and maximizing/minimizing depth with an MCT pitch angle near 0°. Hence, the simulation results of the resulting four cases are presented:

Homogeneous flow without pitch control: For this case, numerical simulations are conducted for five different homogeneous flow speeds, 0.5 m/s, 1.0 m/s, 1.5 m/s, 2.0 m/s, and 2.5 m/s, with both ballast tanks filled with water, $b_{\mathrm{f}} = b_{\mathrm{a}} = 0.0$. Then both ballast tanks were filled with air, $b_{\mathrm{f}} = b_{\mathrm{a}} = 1.0$, quantify the achievable operating range. Resulting equilibrium states, including altitude (negative depth $-Z$), pitch angle θ, and roll angle ϕ, are presented in Figure 3.2 (a) as a function of flow speed.

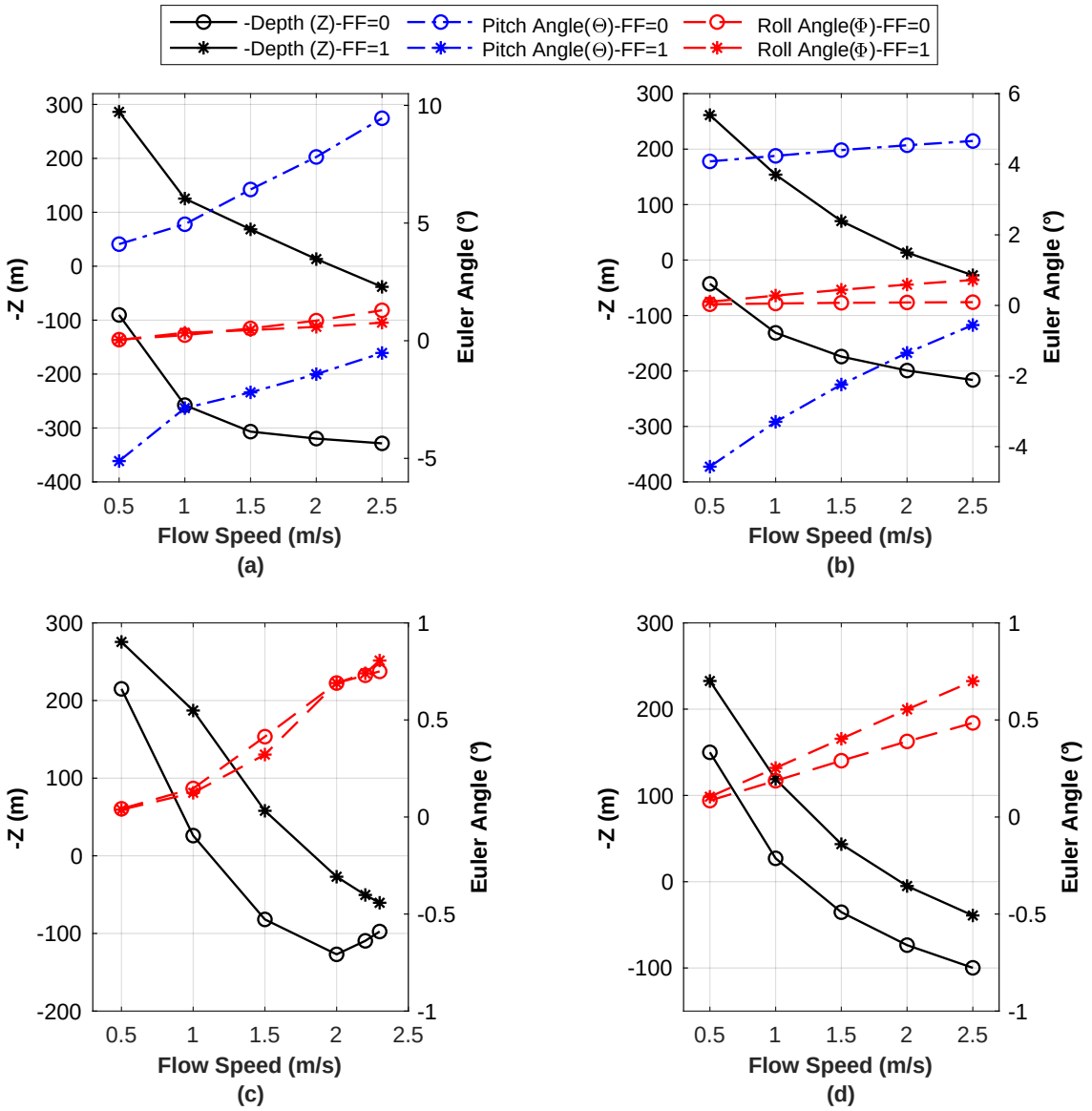

Figure 3.2: Operating range assessment for (a) homogeneous flow speeds, (b) shear flow speeds, (c) homogeneous flow speeds ensuring the pitch angle is driven towards zero, and (d) shear flow speed ensuring the pitch angle is driven towards zero.

Results show that this MCT can reach the sea surface ($Z \approx 15$ m) for flow speeds below 2.2 m/s, and $Z = 38$ m for a flow speed of 2.5 m/s when $b_{\mathrm{f}} = b_{\mathrm{a}} = 1.0$. It is noted that achieved altitudes/depths for flow speeds less than about 2.2 m/s result in the turbine operating partially or fully out of the water as the air/sea interface is not

modeled. However, these results are relevant to MCTs deployed in deeper water and therefore are included. Results also show that maximum depths between $Z = 90$ m to 329 m can be achieved for these flow speeds. Results also show MCT roll angles range between 0.03° to 1.29°, and pitch angles range between −5.11° to 9.45°, with the larger pitch angles achieved at deeper depths.

Shear flow without pitch control: In this scenario, numerical simulations are conducted for sea surface flow speeds of 0.5 m/s, 1.0 m/s, 1.5 m/s, 2.0 m/s, and 2.5 m/s, assuming the flow decreases linearly with depth to a flow speed of 0.0 m/s at the seafloor [113], which is located 325 m below the sea surface. Resulting equilibrium states, including altitude (negative depth $-Z$), pitch angle θ, and roll angle ϕ, are presented in Figure 3.2 (b) as a function of sea surface flow speed. Results show that this MCT can reach the sea surface ($Z \approx 15$ m) for a flow speeds below 2.2 m/s, and $Z = 27$ m for a flow speed of 2.5 m/s. These results also show that maximum depths between $Z = 43$ m to 216 m can be achieved for these flow speeds, more than 100 m shallower than for a homogeneous flow. For these results, MCT roll angles are between 0.03° to 0.72°, and pitch angles range between −4.56° to 4.66°, with larger pitch angles achieved at deeper depths.

Homogeneous flow with pitch control: This case quantifies the MCT's operating range while the pitch angle, θ, remains near 0° (i.e., ±0.5°), as rotor alignment with the flow increases power production and reduces cyclic loads. Obtained equilibrium states, including $-Z$ and ϕ are presented for the homogeneous flow in Figure 3.2 (c). The lowest position is found by setting one b_{f} equal to zero (i.e., tank filled with water) and using a controller to change the other b_{a} and drive θ towards 0°. Similarly, the highest position is found by setting one fill fraction equal to one (i.e., tank filled with air) and using a controller to modify the other fill fraction such that drive θ towards 0°. Results show that this MCT can only operate beneath the sea surface with zero pitch for flow speeds above 1.2 m/s, and cannot reach the sea surface for

flow speeds above 1.9 m/s. Additionally, a depth of 50 m can only be achieved with zero pitch for flow speeds between 1.3 m/s and 2.3 m/s. Therefore, outside of this range, a finite pitch is necessary for operation at this depth with the current MCT configuration.

Shear flow with pitch control: This case quantifies the MCT's operating range in the previously described shear flow (see "Shear flow without pitch control" case) where the pitch angle remains near 0° (see "Homogeneous flow with pitch control" case). Obtained equilibrium states, including $-Z$ and ϕ are presented for the homogeneous flow in Figure 3.2 (d). Results show this MCT can only operate beneath the sea surface with zero pitch for flow speeds above 1.3 m/s, and cannot reach the sea surface for flow speeds above 2.1 m/s. Additionally, a depth of 50 m can only be achieved with zero pitch for flow speeds between about 1.7 m/s and 2.6 m/s. Therefore, outside of this range, a finite pitch is necessary for operation at this depth with the current MCT configuration.

3.3.2 Actuator Fault Response: Rotor Braking

The actuator fault scenario of "rotor braking" is presented in this section, which is also a necessary scenario for MCT deployment/retrieval. System response is very dynamic as total system drag decreases by more than 50%. For this analysis, the MCT initially operates at a depth of 50 m in shear flow with a surface speed of 1.6 m/s. Rotor rotation, ω, is rapidly stopped at $t = 3000$ s, and the resulting MCT pitch angle, θ, and vertical position, $-Z$, are presented in Figure 3.3, along with the corresponding values if braking is not applied. Presented results show that θ remains within 1°, as well as changes in both roll, ϕ, and yaw, ψ (not shown). Moreover, the MCT moves rapidly upwards, hitting the ocean surface in 100 s. Ignoring sea surface effects, these results show a net 80 m upward MCT displacement, a result relevant to deeper deployment locations. This response can eventually be compensated by

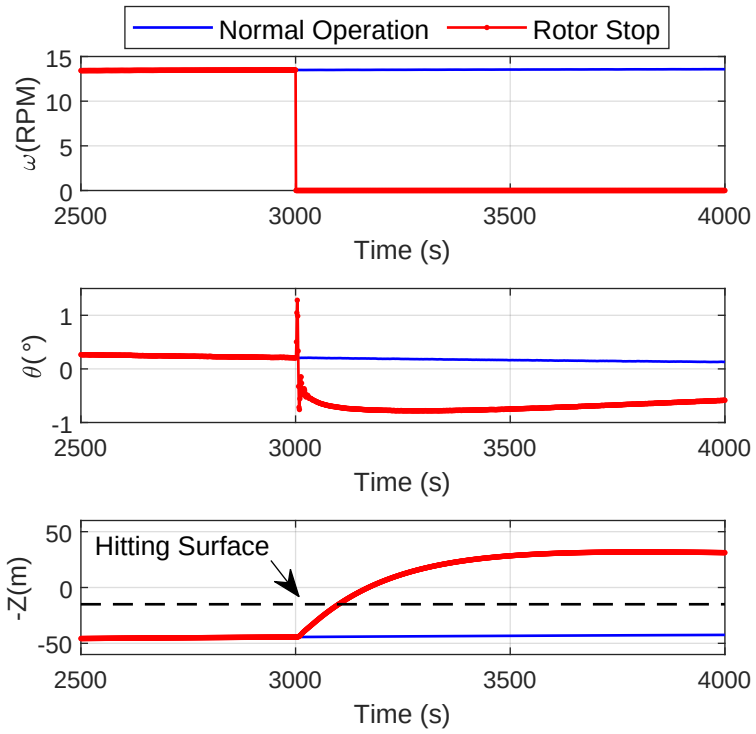

Figure 3.3: Time histories of the MCT's equilibrium states, i.e., angular speed ω, pitch angle θ, and vertical position Z before and after rotor stop at $t = 3000$.

adding water to the ballast tanks. However, the ballast process of an MCT will likely occur much more slowly than the response to rotor braking (22 minutes estimated earlier here for a complete ballast). Therefore, rotor braking implications should be carefully considered when planning MCT operations.

3.3.3 Rotor Fault Response: Blade Pitch Fault

The impacts of blade pitch imbalance faults are highlighted in this section. For this analysis, the MCT initially operates at a depth of 50 m with a linear shear from a speed of 1.6 m/s at the surface to 0.0 m/s at the sea floor. A pitch imbalance of 4° occurs at $t = 2000$ s for the "fault" case. Two different turbulence intensities are considered, 0% to highlight fault signature details and 10% to highlight how ambient

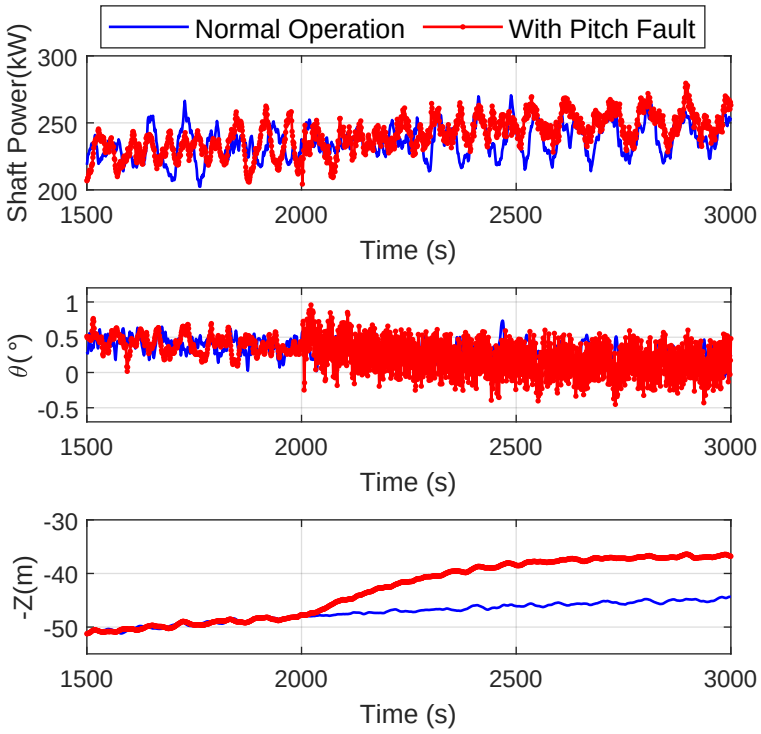

Figure 3.4: Time histories of the MCT's equilibrium states, i.e., shaft power, pitch angle θ, and vertical position Z before and after pitch fault at $t = 2000$ s at the turbulence intensity of 10%.

turbulence masks faults signatures. Time histories are shown with and without faults in Figure 3.4 for a turbulence intensity of 10%. This figure shows that the shaft power has minimal perceivable deviations in the time domain, while pitch angle deviations are more easily visible. However, these deviations are relatively small with all Euler angles (i.e., pitch angle, roll angle, and yaw angle), remaining within 1° for all cases. Additionally, the MCT moves 15 m upward after the blade pitch fault.

The effects of the blade pitch fault are presented in the frequency domain for pitch, θ, and shaft power (Figure 3.5). Normalized pitch angle θ (Figure 3.5 (a)) and normalized shaft power (Figure 3.5 (b)) spectra for non-turbulent water show spikes at multiples of the rotor angular speed, i.e., 1P and 2P, and these spikes are

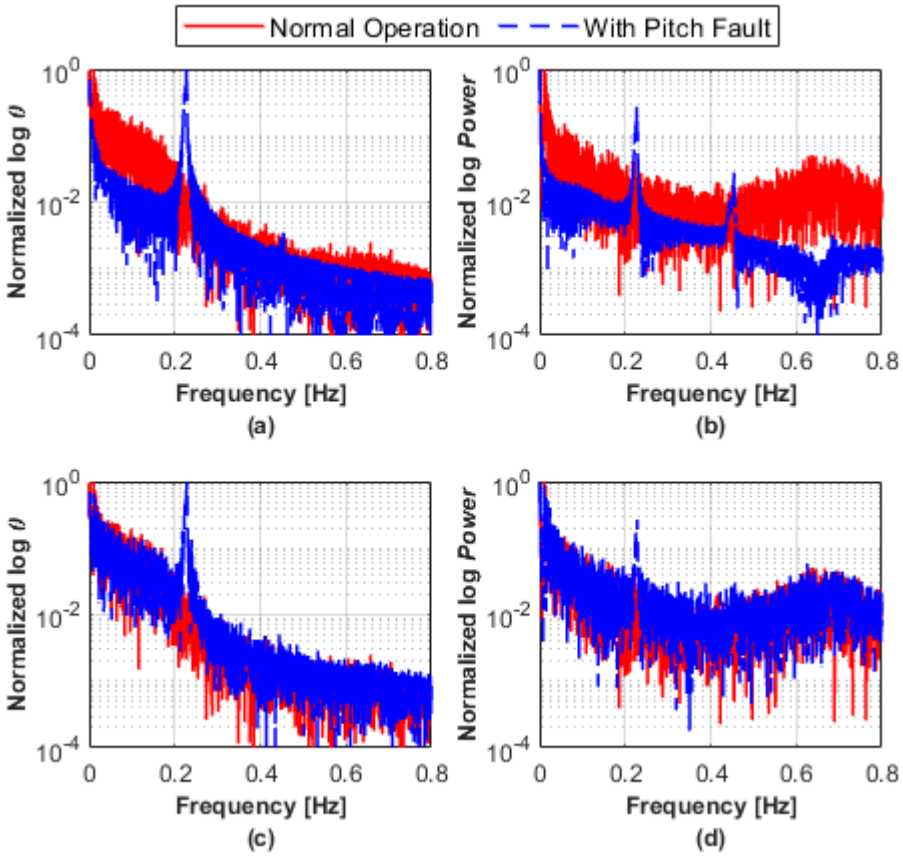

Figure 3.5: Frequency domain of the pitch fault of 4° for (a) normalized pitch angle (θ) without turbulence, (b) normalized shaft power without turbulence, (c) normalized pitch angle (θ) at the turbulence intensity of 10%, and (d) normalized shaft power at the turbulence intensity of 10%.

even more visible for shaft power. On the other hand, the frequency response of the normalized pitch angle θ (Figure 3.5 (c)) and normalized shaft power (Figure 3.5 (d)) spectra are only easily distinguishable at the 1P frequency.

3.3.4 MCT Operating in an Oceanic Environment

MCT operations in measured oceanic environments are investigated. Simulations are run for a "normal" condition (Figure 3.6) and two "hurricane" conditions (Figs. 3.7

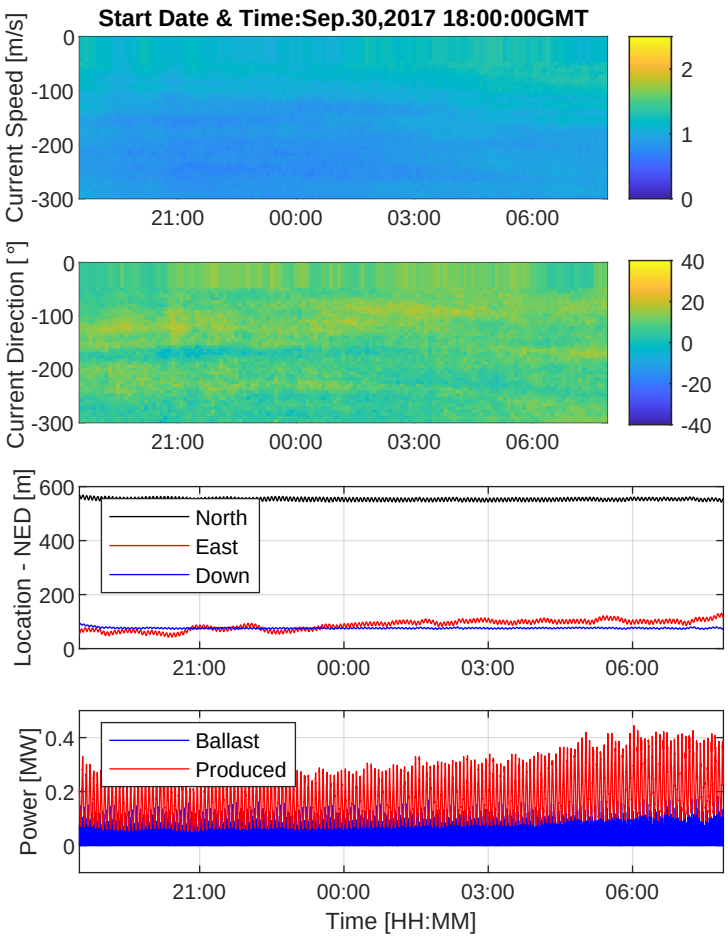

Figure 3.6: Normal condition (October 1, 2017): time histories of the MCT's states, i.e., Euler angle, location-NED, and power.

and 3.8). October 1st, 2017 represents a "normal" condition for this region with a mean flow speed over the simulated time-frame of 1.19 m/s at a depth of 75 m. September 11th, 2017 is the date that Hurricane Irma passed through the Florida Keys, resulting in a much higher than normal flow speed in the measurement area [114] (mean flow speed of 2.0873 m/s for a depth of 75 m over the simulated time-frame). September 25th, 2017, had a low current event that was likely associated with Hurricane Irma, as suggested by [114], and/or a counter-clockwise eddy that traveled along the western edge of the Gulf Stream (mean current speed for a depth of 75 m of 0.87 m/s over the simulated time-frame). Wave conditions for these dates are modeled

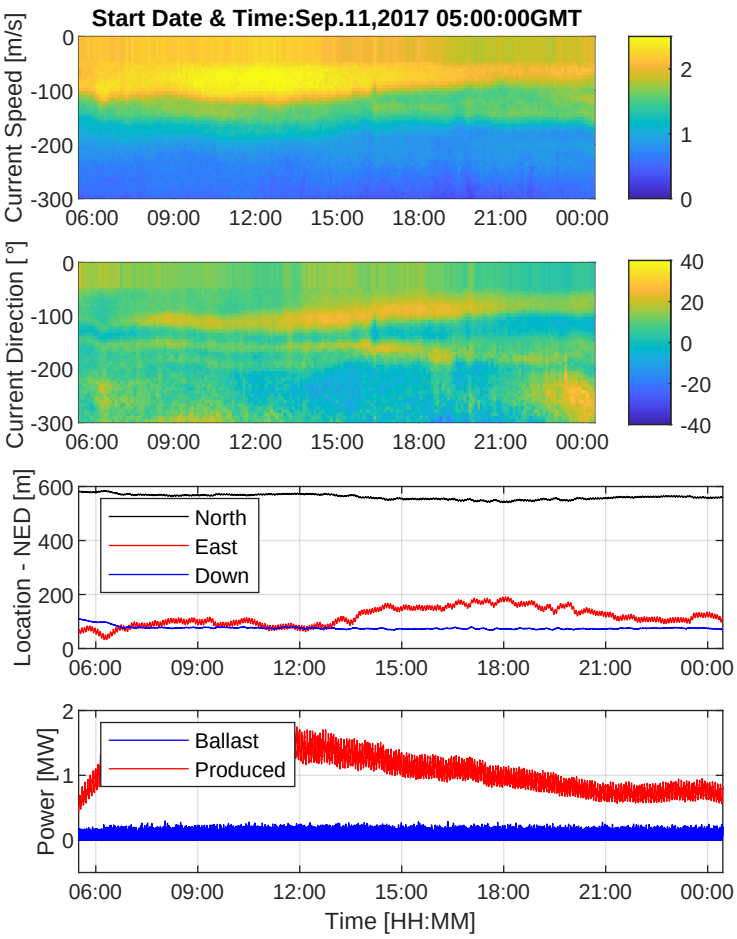

Figure 3.7: Hurricane condition (September 11, 2017): time histories of the MCT's states, i.e., Euler angle, location-NED, and power.

based on the National Oceanic and Atmospheric Administration (NOAA) wave buoy recorded wave heights and direction in the Fort Pierce, Florida [115]. For the October 1st, 2017, the significant wave height and direction are 0.8 m and 60°, respectively. For the September 11th, 2017, the significant wave height is 5.0 m and direction is 90°, while on September 25th, 2017, the significant wave height and direction are 2.0 m and 80°, respectively.

For these simulations, a low gain PI controller sets MCT ballast tank fill levels based on depth error such that a depth near 75 m is maintained,

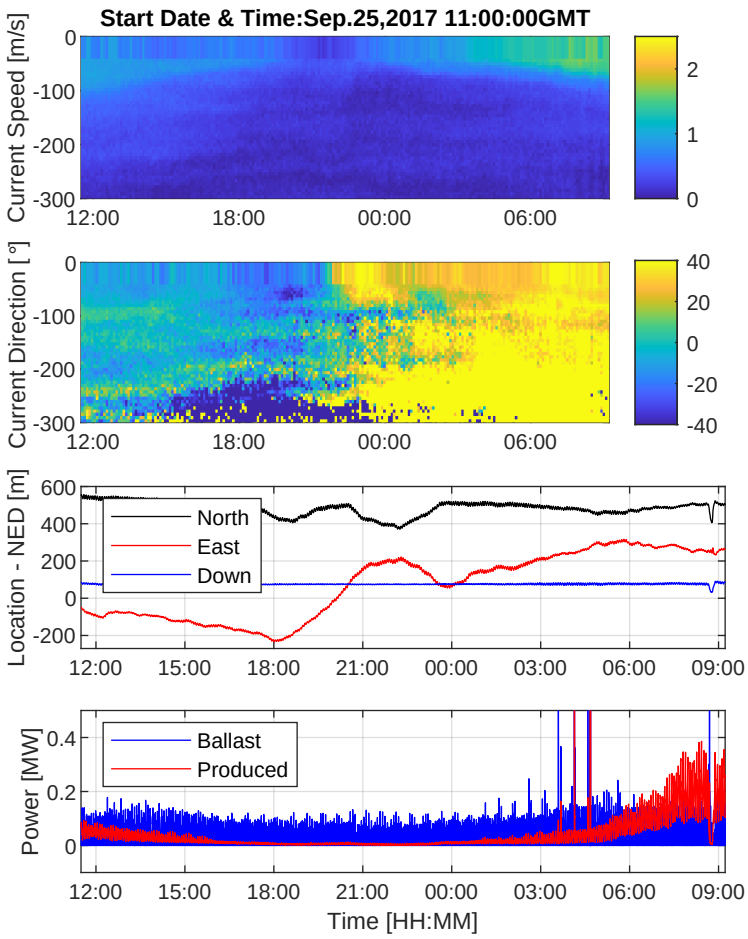

Figure 3.8: Hurricane condition (September 25, 2017): time histories of the MCT's states, i.e., Euler angle, location-NED, and power.

$$b_{\mathrm{f}} = b_{\mathrm{a}} = G_P * (Z - 75) + G_I * \int_0^t (Z - 75)dt \tag{3.29}$$

where G_P is the proportional gain and G_I is the integral gain. This also allows for an estimate of the ballast pump power required to maintain depth using equations presented in the next chapter (4.12) and (4.13). Presented results show that the depth remains within 75 m $\pm$ 35 m for both normal and hurricane conditions. Position and power signals in all cases have perturbations at frequencies around 0.0036 Hz (periods around 4.6 minutes) that are likely related minimally damped position states being excited by low-frequency turbulence perturbations. The stability of moored MCTs

is discussed in detail in [51], and these oscillations can be dampened through active control.

The resulting location and power (both harnessed and utilized by ballast pumps) during the "normal" conditions measured on October 1st are presented in Figure 3.6. Over the simulated 13 hours of operation flow speeds ranged between 1.06 m/s and 1.34 m/s at a depth of 75 m, with the flow direction at this depth remaining between 4.29° and 14.20°. The calculated mean produced power of the MCT is 0.17 MW, where the mean ballast power to maintain the depth is 0.02 MW (i.e., 11.76% of mean produced power). The MCT's east position with respect to the anchor point, Y, changes between 41.71 m and 114.05 m, and its depth, Z, remains within 70.86 m and 93.13 m below the sea surface. Moreover, the results show that pitch, θ, roll, ϕ, and yaw, ψ, deviations remain within ranges of 2.04°, 1.66°, and 16.80°, respectively (not shown).

For the hurricane condition on September 11, 2017 results are shown in Figure 3.7. Over the simulated 14 hours of operation, the flow speeds change within a wider range of 1.85 m/s and 2.32 m/s at a depth of 75 m, with flow directions between 2.99° and 17.46° at this depth. The mean produced power of the MCT increases to 1.06 MW due to higher flow speeds, where the mean ballast power is 0.027 MW (i.e., 2.5% of mean produced power). It is noted that this produced power is above the "rated" power of 700 kW mentioned previously for this design. Therefore, either power regulation control such as pitch control or active depth control should be used to keep produced electric power at or below rated power. The MCT moves within 32.62 m and 167.53 m in the east position, Y, and its depth, Z, ranges between 68.33 m and 110.07 m. Further, the results show that pitch, θ, roll, ϕ, and yaw, ψ, remain within ranges of 4.55°, 3.50°, and 19.6°, respectively (not shown).

For the low current case found on September 25th, 2017, results are presented in Figure 3.8. Over the simulated 11 hours, flow speeds change within 0.3511 m/s and

1.6426 m/s at a depth of 75 m, with the flow direction at this depth ranging between $-32.57°$ and $46.92°$. Mean produced MCT power decreases to 0.039 MW due to lower flow speeds, while the mean ballast power increases to 0.018 MW (i.e., 46.15% of mean produced power). The MCT moves within a wide range of -234.30 m and 316.59 m in the east direction, Y, due to the large changes in flow direction and its depth, Z, ranges between 66.87 m and 85.16 m. It is noted that the MCT hit the sea surface for this case when the current design was used, even when both ballast tanks were completely filled with water. Therefore, the ballast fill levels were allowed to go slightly negative (i.e., the turbine became slightly less buoyant than when both tanks are filled with water) when running this simulation to keep the turbine below the sea surface. Further, the results show that pitch, θ, roll, ϕ, and yaw, ψ, remain within ranges of $1.69°$, $1.85°$, and $74.97°$, respectively (not shown).

3.4 CONCLUSION

In this chapter, we presented a complete dynamic simulation for a buoyancy controlled MCT system, including a turbine, cable, and actuator (i.e., generator and variable buoyancy). Probable MCT faults were integrated into this simulation, including rotor, actuator, and sensor faults. Simulations were run for several different cases, including different simplified flow conditions, both actuator and rotor faults, and system performances in measured open ocean currents. We showed that the designed MCT can operate between depths of 38 m to 90 m for all homogeneous flow speeds between 0.5 and 2.5 m/s, and depths of 27 m to 43 m when the flow decreased linearly with depth from these flow speeds to 0.0 m/s at the sea floor. Moreover, performance results were presented for both normal and hurricane conditions where the operating depths remained within 75 m$\pm$35 m by using a PI controller. The novelty of the work, compared to existing research in the field is that we designed a buoyancy-controlled MCT for the real application in the Gulf Stream of Florida's East Coast and evaluate

its performance under several real condition, which is necessary before testing the system in the real-world operation.

CHAPTER 4
PATH PLANNING ALGORITHM FOR BUOYANCY CONTROLLED MCT

This chapter presents a novel spatiotemporal optimization approach for vertical path planning (i.e., waypoint optimization) to maximize the net output power of an MCT under uncertain ocean velocities. To determine the net power, MCT power generation from hydrokinetic energy and the power consumption for controlling the depth are modeled. The stochastic behavior of ocean velocities is a function of spatial and temporal parameters, which is modeled through a Gaussian process (GP) approach. The net power of the MCT system is composed of three parts, generated power, power for maintaining the system at an operating depth, and power consumed for navigating the turbine to the optimal water depth. Two different algorithms, including MPC as a model-based method and RL as a learning-based method, are applied to solve the formulated spatiotemporal optimization problem with constraints. Comparative studies show that the MPC- and RL-based methods are computationally feasible to address vertical path planning, which are evaluated with a baseline A* approach. Three RL algorithms, including Q-learning, DQN, and PPO, are nominated to deal with the path planning over both discrete gridded and continuous underwater environments modeling. These RL algorithms are compared, which are defined for both discrete and continuous representations of the oceanic environment.

Also, this chapter presents an integrated path planning and tracking control of marine hydrokinetic energy harvesting devices. To address the highly nonlinear and uncertain oceanic environment, the path planner is designed based on an RL approach by fully exploring the historical ocean current profiles. The planner will search for a

path to optimize a chosen cost criterion, i.e., maximizing the total harvested energy for a given time. The MPC approach is then utilized to design the tracking control for the optimal path command from the planner subject to problem constraints. The planner and the tracking control are accommodated in an integrated framework to optimize these two parts in a real-time manner. The proposed approach is validated on the designed MCT that executes vertical waypoint path searching to maximize the net power due to spatiotemporal uncertainties in the ocean environment, as well as the path following via an MPC tracking controller to navigate the MCT to the optimal path.

In summary, our main contribution in this chapter is threefold: 1) we propose a precise linear model to represent the net harvested power of a buoyancy-controlled MCT system, which includes directly generated power from ocean currents, consumed power for stabilizing the system at specified water depths, and consumed power to navigate to new optimal operating depths. The linear power model is derived based on the nonlinear modeling of the MCT to lessen the computational complexity, which is justified with the nonlinear model; 2) we also formulate a novel spatiotemporal optimization problem for the MCT vertical path planning operating in an uncertain oceanic environment to maximize the total harvested power of the system. This problem is solved through the RL-based method, the MPC-based strategy and a baseline A* approach; 3) We propose an integrated approach that iteratively plans the optimal path to maximize the harvested power and tracks the commanded path to minimize the tracking error.

4.1 PATH PLANNING PROBLEM FORMULATION

The schematic diagram of the studied MCT vertical path planning problem is shown in Figure 4.1. In this problem, the ultimate objective is to maximize the MCT generated power through a spatiotemporal optimization approach. Based on the

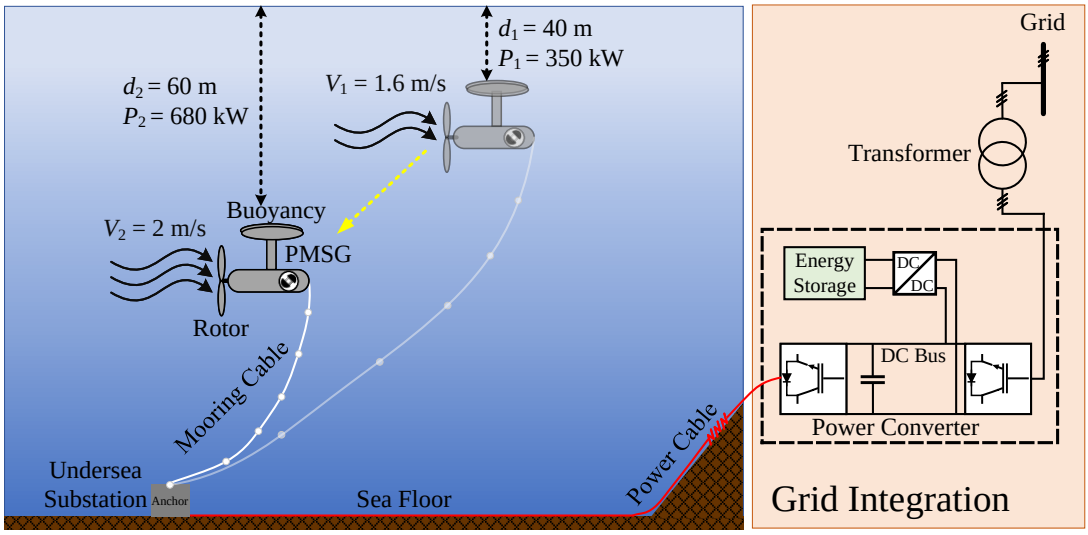

Figure 4.1: Proposed spatiotemporal optimization for MCT vertical path planning. The system is controlled hierarchically, and the main objective of the path planning is to maximize the harnessed power form the MCT.

predicted ocean velocity, the optimal path should be determined at each sampling time.

To address the complexity of this problem, a novel hierarchical spatiotemporal optimization and control framework is proposed. The ocean velocity is first modeled with the GP method, and the forecasted velocity is used to calculate the output power of the MCT system. The MCT system is controlled hierarchically, where the upper-level is designed to enable spatiotemporal optimization, and the lower-level is a dynamic tracking control.The MCT output power P is received by the spatiotemporal optimization at each time step in the upper-level, while the optimal water depth z^* as a set-point is determined accordingly for the lower-level controllers. The lower-level control tracks the prescribed set-points from the upper-level and adjust the turbine dynamics.

We first focus on the upper-level spatiotemporal optimization in this chapter, assuming that the lower-level control exists and follows the optimal path found through

the spatiotemporal optimization. This assumption arises from our experiments and knowledge on the dynamics of the MCT system and the previously designed flight controllers [116, 117], ignoring the detailed model of the MCT system. Two major operational constraints of the MCT system directly affecting the vertical path planning, including the range of operating depth and the constraint on the slew rate (i.e., highly related with the mooring system design), as well as the real recorded data from the Gulf Stream, are included in our spatiotemporal model to ensure a feasible vertical path according to the MCT model and real ocean environment. However, We are further developing an integrated path planning and tracking control framework for the investigated MCT system in the second part of this chapter.

The major goal of the proposed approach is to plan the vertical path that maximizes the harnessed power from the MCT, subject to the operational constraints of the MCT system and environmental model. The spatiotemporal optimization problem and constraints are formulated as follows:

$$\mathcal{OP}: \mathbf{u}^*(p) = \arg\min_{\mathbf{u}(p)} \sum_{i=p}^{p+T-1} [-E(P_{\text{net}}(u(i|p), v_*(u(i|p), i|p))] \tag{4.1a}$$

subject to

$$v_*(u(i|p), i|p) \sim f(z,t) \tag{4.1b}$$

$$u^{\min} \leq u(i|p) \leq u^{\max} \tag{4.1c}$$

$$\dot{u}(i|p) \leq \dot{u}^{\max} \tag{4.1d}$$

where $\mathbf{u}(p) \triangleq [u(p|p), ..., u(p+T-1|p)]$ denotes the decision variables vector, the optimal finite-horizon decision variables sequence $\mathbf{u}^*(p) \triangleq [u^*(p|p), ..., u^*(p+T-1|p)]$ is computed as the solution of the optimization problem. The predicted velocity is denoted by $v_*(u(i|p), i|p)$, the net output power is denoted by P_{net}, the expected power is denoted by $E(P_{\text{net}}(.))$, the minimum and maximum allowable decision variables are

denoted by $u^{\min}$ and $u^{\max}$, and the maximum limit on the slew rate is denoted by $\dot{u}^{\max}$. Here, constraint (4.1b) shows a model to predict the ocean velocity over the prediction horizon; also, constraints (4.1c) and (4.1d) limit decision variables and the corresponding slew rate. Note that the decision variable is defined as the operating depth of the MCT system z in our spatiotemporal optimization problem.

4.2 OCEAN ENVIRONMENT AND MCT MODELING

The uncertainties in the ocean current velocity field are addressed, and the future ocean velocity is predicted that is further used in the spatiotemporal optimization. The net generated power of an MCT system, which is a function of the ocean velocity, is then modeled in detail.

4.2.1 Statistical Ocean Current Shear Profile Characterization

The ocean velocity field varies with time in a 3D space. However, moored MCTs can primarily vary their vertical location (i.e., depth), and current shear is most prominent in the vertical direction. Therefore, the ocean velocity's dependence on both time and water depth is of primary importance; in other words, the ocean velocity should be determined at specific times t and operating depths z. The observed (recorded) ocean velocity data are represented as:

$$\mathbf{V_{n\times m}} = \begin{bmatrix} v(z_1,t_1) & \dots & v(z_1,t_m) \\ \vdots & \ddots & \\ v(z_n,t_1) & \dots & v(z_n,t_m) \end{bmatrix} \tag{4.2}$$

where n and m are the numbers of the discrete depths and the time samples, and $v(z_i,t_j)$ is the recorded ocean velocity at z_i and t_j. Matrix $\mathbf{V}$ includes $n\times m$ recorded ocean velocities.

Let $\mathcal{Z}$ denote the domain of allowable ocean depth choices, and $\mathcal{T}$ represent the temporal space. The goal here is to model ocean current velocity at depth $z \in \mathcal{Z}$

Table 4.1: Comparing different methods for modeling ocean velocities. Results are quantified by RMSE, MSE, and MAE.

Algorithms	RMSE	MSE	MAE
Linear regression	0.0369	0.0014	0.0297
Regression trees	0.0614	0.0038	0.0302
Support vector machines	0.0232	0.0005	0.0205
Gaussian process model	0.0031	9.6×10^{-6}	0.0022

and time $t \in \mathcal{T}$, by constructing a function $f : \mathcal{Z} \times \mathcal{T} \to \mathcal{R}$ whose output is a predicted velocity. The ocean velocity and especially the ocean turbulence are usually modeled with probability distributions, including log-normal distribution [118] and Burr distribution [119]. In this section, different methods for modeling the velocity are developed and compared, as shown in Table 4.1. Linear regression, regression trees, support vector machines, and the GP are compared and quantified using root mean square error (RMSE), mean square error (MSE), and mean absolute error (MAE), by assuming 70% of the recorded velocities as a training set, 15% for validation, and 15% for testing. The GP modeling shows the best performance and is briefly introduced in the following.

Gaussian Process Model: The GP is a probabilistic approach used to define a prior probability distributions over latent functions directly, which is extensively applied in wind speed forecasting [25, 120, 121] and ocean current flow velocity prediction [122, 123]. To predict the ocean current velocity, the GP model can be addressed through either a pure learning approach by finding the parameters for the Gaussian predictive distribution [122] or combining the laws of physics (e.g., nonlinear dynamics described by the partial differential equations) with the learning approach and propagating the uncertainty through time with the time-stepping method [95]. We proceed with the first approach when constructing the GP model through learning from the observed

velocity, while the latter is beyond the scope of our study and calls for a dynamic nonlinear model to describe the ocean current velocity. Another potential approach for modeling the ocean current flow velocity is to develop a physics-based deep neural network to learn the spatiotemporal features of the data [124], but this is not the focus of the current study.

To approach the real-world application and given that an acoustic Doppler current profiler (ADCP) will likely be installed just upstream from a turbine, an online learning approach that assumes water measurements velocities are available throughout the water column is used to predict the ocean current velocity. The aforementioned online approach deals with a finite size of input data to avoid the scalability issue as suggested in [122]. It is worth noting that the scalability of the GP model is well studied in the literature, proposing several precautions to avoid this issue, e.g., a sparse representation to recursively update the GP [125] or using a stochastic variational inference approach [126]. The computational complexity is intensified for our application due to its nature for a long-term and persistent operation when the size of input data increases. Hence, the prediction is generated according to a fixed-size rolling window of the observed ocean current velocity, which is accordingly rolled to complete the prediction over the prediction horizon, thereby removing the old data by the arrival of a new observation in the online application to maintain a fixed-size window. Since the accuracy degrades for predicting distant data when proceeding with a fixed GP model, the GP model is periodically regenerated.

Define $\mathbf{x}$ as the input set of the recorded ocean velocity associated with the target ocean velocity of v. The GP model with mean $m(\mathbf{x})$ (i.e., encodes the central tendency) and covariance $k(\mathbf{x}, \mathbf{x}^{'})$ (i.e., denotes the shape and structure between any two input sets of $\mathbf{x}$ and $\mathbf{x}^{'}$) is defined as:

$$f(\mathbf{x}) \sim \mathcal{GP}(m(\mathbf{x}), k(\mathbf{x}, \mathbf{x}^{'})) \tag{4.3}$$

The ocean velocity is predicted as $v = f(\mathbf{x}) + \epsilon$, while ϵ denotes a Gaussian

distribution $\mathcal{N}(0,\sigma^2)$. The joint distribution over the input set $\mathbf{x}$ and a prediction of the target ocean velocity v_* is defined as [127]:

$$\begin{bmatrix} \mathbf{v} \\ v_* \end{bmatrix} = \left(\begin{bmatrix} f \\ f_* \end{bmatrix} + \begin{bmatrix} \epsilon \\ \epsilon_* \end{bmatrix} \right) \sim \mathcal{N}\left(0, \begin{bmatrix} K_v & \mathbf{k}_* \\ \mathbf{k}_*^{\mathrm{T}} & k_{**} + \sigma^2 \end{bmatrix}\right) \tag{4.4}$$

where $f_* \triangleq f(\mathbf{x}_*)$ shows the latent function based on a new input vector $\mathbf{x}_*$ with corresponding noise ϵ_*. $\mathbf{v}$ denotes an output set of the ocean velocity. Define $K_v = k(\mathbf{x}, \mathbf{x})$; $\mathbf{k}_*$ and k_{**} are calculated as:

$$\mathbf{k}_* = [k(\mathbf{x}_*, \mathbf{x}_1), k(\mathbf{x}_*, \mathbf{x}_2), ..., k(\mathbf{x}_*, \mathbf{x}_m)] \tag{4.5}$$

$$k_{**} = k(\mathbf{x}_*, \mathbf{x}_*) \tag{4.6}$$

To represent the GP modeling, the mean $m(\mathbf{x}_*)$ and covariance $\sigma^2(\mathbf{x}_*)$ are defined as follows:

$$m_* \triangleq m(\mathbf{x}_*) = \mathbf{k}_*^{\mathrm{T}} K_v^{-1} \mathbf{v} \tag{4.7}$$

$$\sigma_*^2 \triangleq \sigma^2(\mathbf{x}_*) = k_{**} - \mathbf{k}_*^{\mathrm{T}} K_v^{-1} \mathbf{k}_* + \sigma^2 \tag{4.8}$$

Finally, the GP model for predicting new ocean velocities is determined using mean and covariance in (4.7) and (4.8):

$$f_* \sim \mathcal{GP}(m_*, \sigma_*^2) \tag{4.9}$$

4.2.2 Oceanic Environment Representation

The oceanic environment is represented in 1D (z-direction) since the autonomous MCT can primarily move in the vertical direction. In reality, there are two ways to implement this vertical path planning: a discrete manner that the turbine can only move to several discrete depths or a continuous manner that the turbine can move to any depth. Figure 4.2 illustrates two representations of a discrete (gridded)

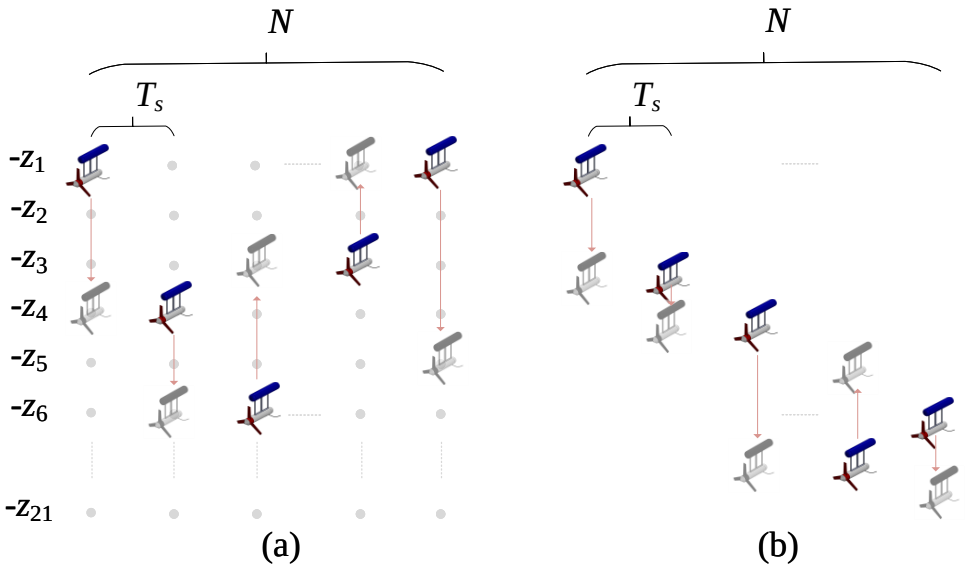

Figure 4.2: Schematic of the ocean environment. (a) Discrete (gridded) representation; (b) Continuous representation.

and continuous spatiotemporal underwater environment investigated in this chapter. In a gridded environment, we assume that the environment information, i.e., the discretized operating depth (waypoint) and history of recorded ocean current velocity, are fully known. Note that the operating depth is discretized every 6 m within the allowable depth range (21 waypoints total in the Gulf Stream), and the prediction horizon is N sampling time (i.e., predicted by the aforementioned STNN). While in the continuous environment, the autonomous MCT can continuously move to any feasible depth.

4.2.3 Mathematical Model of MCT Output Power

The output power of the designed MCT system is formulated in this section. The nonlinear MCT modeling techniques are utilized when simulating this system for the creation of the linear models used in the presented formulations. The output power of the system consists of three primary parts:

1. Generated power from hydrokinetic energy extraction, denoted as P_{MCT};

2. Power consumed by ballast pumps to Hold Depth, denoted as $P_{\mathrm{ballast}}^{\mathrm{HD}}$; and

3. Power consumed by ballast pumps to Change Depth, denoted as $P_{\mathrm{ballast}}^{\mathrm{CD}}$.

The total harvested power from the MCT system is calculated by (4.10):

$$P_{\mathrm{net}} = P_{\mathrm{MCT}} - P_{\mathrm{ballast}}^{\mathrm{HD}} - P_{\mathrm{ballast}}^{\mathrm{CD}} \tag{4.10}$$

where P_{net} is the total harvested power from the MCT system, P_{MCT}, $P_{\mathrm{ballast}}^{\mathrm{HD}}$, and $P_{\mathrm{ballast}}^{\mathrm{CD}}$ denote three parts of the harvested power.

First term, $\boldsymbol{P_{\mathrm{MCT}}}$: The generated power of MCT system is related to ocean velocity according to [128]:

$$P_{\mathrm{MCT}} = \frac{1}{2}\rho A C_{\mathrm{p}} v^3 \tag{4.11}$$

where ρ is the water density, A is the swept area of the MCT rotor, C_{p} is the average power coefficient, and v is the magnitude of the ocean velocity.

Second term, $\boldsymbol{P_{\mathrm{ballast}}^{\mathrm{HD}}}$: To calculate $P_{\mathrm{ballast}}^{\mathrm{HD}}$, the average consumed power for maintaining a near constant depth in a time-varying current is determined. This model assumes that ballast tank water fill levels, which are defined as a fraction of ballast capacity b (assuming that two fill fractions introduced in Section 3.2 are equal, i.e., $b_{\mathrm{f}} = b_{\mathrm{a}}$), are adjusted every Δt_1 to counteract changes in the flow velocity Δv and maintain the desired operating depth z. It should be noted that changes in flow velocity impact the mooring cable force (i.e., downward force in the MCT), resulting in an MCT elevation change unless counteracted by an equal and opposite change in the buoyancy force. Hence, the ballast levels must be changed to hold a constant depth when the flow velocities change. It should be noted that some equations regarding the buoyancy tank are repeated from Section 3.2 to clarify the modeling concept.

For these adjustments, the model assumes that a pump drives water through an opening such that the pressure in the tank is at vacuum pressure (i.e., $P_{\mathrm{abs}} \cong 0\,\mathrm{kPa}$).

Using this approach, very little power is used when the tanks are being filled with water since this can be driven by the natural pressure difference between ambient pressure and vacuum pressure. The power required to pump sea water out of the tank can be calculated from the product of the force F (i.e., the product of pressure and area, ΔPA) and velocity V (i.e., the quotient of volumetric flow rate over the area, Q_{B}/A) through the orifice divided by pump efficiency. Accordingly, the power to fill the tank $P_{\mathrm{B}}^{\mathrm{fill}}$ and the power to empty the tank $P_{\mathrm{B}}^{\mathrm{empty}}$ are defined as follows:

$$P_{\mathrm{B}}^{\mathrm{fill}} = 0 \tag{4.12}$$

$$P_{\mathrm{B}}^{\mathrm{empty}} = \frac{FV}{\eta_{\mathrm{pump}}} = \frac{\Delta P Q_{\mathrm{B}}}{\eta_{\mathrm{pump}}} \tag{4.13}$$

where η_{pump} denotes the pump efficiency. Given that $\Delta P = P_{\mathrm{atm}} + P_{\mathrm{HS}}$, the power to empty the tank defined in (4.13) can be rewritten as:

$$P_{\mathrm{B}}^{\mathrm{empty}} = \frac{(P_{\mathrm{atm}} + P_{\mathrm{HS}})Q_{\mathrm{B}}}{\eta_{\mathrm{pump}}} \tag{4.14}$$

where P_{atm} is atmospheric pressure, $P_{\mathrm{HS}} = \rho.g.z$ is hydrostatic pressure, and g is gravity.

Assuming a constant value for Q_{B}, two ballast tanks with volume of ν_{B} can be completely emptied of water in $\Delta t_{\mathrm{e}} = \frac{Q_{\mathrm{B}}}{\nu_{\mathrm{B}}}$. Hence, the energy required to empty either ballast tank $E_{\mathrm{tank}}^{\mathrm{empty}}$ and fill either ballast tank $E_{\mathrm{tank}}^{\mathrm{fill}}$ at an operating depth of z_{opt} are calculated by:

$$E_{\mathrm{tank}}^{\mathrm{fill}} = 0 \tag{4.15}$$

$$E_{\mathrm{tank}}^{\mathrm{empty}} = \frac{P_{\mathrm{B}}^{\mathrm{empty}}}{\Delta t_1} \tag{4.16}$$

To maintain MCT depth, ballast tank fill levels are changed every Δt_1 by a fraction of their total fill levels Δb to counteract the changes in flow velocity Δv. These changes in ballast fill levels occur more frequently than the changes in desired depth calculated

by the spatiotemporal optimization algorithm, with the associated fill level changes calculated using linear estimates of the relationships between fill level changes and equilibrium depth changes $\frac{db}{dz}$ as well as between flow speed changes and equilibrium depth changes $\frac{dv}{dz}$. Assuming linearity, the following relationship exists between flow speed changes and ballast level changes necessary to maintain a constant depth:

$$\frac{\Delta b}{\Delta v} = \frac{db}{dz}\frac{dz}{dv} \Rightarrow \Delta b = \frac{db}{dz}\frac{dz}{dv}\Delta v = \zeta \Delta v \tag{4.17}$$

where $\zeta = \frac{db}{dz}\frac{dz}{dv}$ denotes a constant coefficient to relate the flow speed changes and ballast level changes. It should be noted that in this section, a quasi-static relationship is assumed between the states and a steady and homogeneous flow field when running the nonlinear simulation.

The average power consumed over each Δt_1 to maintain the operating depth can be calculated using (4.17):

$$P_{\text{ballast}}^{\text{HD}} = \begin{cases} 0, & \text{if } \Delta v < 0 \\ \frac{(E_{\text{B}}^{\text{empty}})(\zeta \Delta v)}{\Delta t_1}, & \text{if } \Delta v > 0 \end{cases} \tag{4.18}$$

Third term, $\boldsymbol{P_{\text{ballast}}^{\text{CD}}}$: To calculate $P_{\text{ballast}}^{\text{CD}}$, the ballast model and its average consumed power for changing depth can be determined using many of the assumptions and models introduced for the second term of this formulation. To change MCT depth, ballast tank fill levels are changed every time step Δt_2 by a fraction of their total fill levels Δb. This change in fill level is based on the desired change in depth Δz using the linear relationship between Δz and Δb:

$$\Delta b = \frac{db}{dz}\Delta z = \kappa \Delta z \tag{4.19}$$

where $\kappa = \frac{db}{dz}$ denotes a constant coefficient to relate the fill level changes and depth changes.

The average consumed power to satisfy Δz depth change is calculated with respect to the energy required to fill the ballast tank (4.15), the energy required to empty the

Algorithm 1 Path Planning Spatiotemporal Optimization

1: Initialize n data sample $v(z,t)$ and optimization method parameters
2: **for** Each t **do**
3: Construct the GP model (f_*) based on a fixed-size window of the observed data;
4: **for** Prediction Horizon T **do**
5: Predict v_* over T using the GP model $f_* \sim \mathcal{GP}(m_*, \sigma_*^2)$;
6: **end for**
7: Apply optimization algorithm (e.g., MPC or RL);
8: Output optimal depth z^*;
9: **end for**

ballast tank (4.16), and the relation between fill fraction change and depth change (4.19) as follows:

$$P_{\text{ballast}}^{\text{CD}} = \begin{cases} 0, & \text{if } \Delta z > 0 \\ \frac{(E_{\text{B}}^{\text{empty}})(\kappa \Delta z)}{\Delta t_2}, & \text{if } \Delta z < 0 \end{cases} \tag{4.20}$$

4.3 PROPOSED METHODOLOGY

In this section, we focus on the spatiotemporal optimization shown in Figure 4.1. The pseudocode for this process is presented in Algorithm 1. Two approaches, MPC as a model-based approach and RL as a learning-based approach, are considered here. Also, the obtained path planning results are justified with a baseline A* approach.

4.3.1 Baseline Approach: A^*-based Vertical Path Planning

The A* algorithm is utilized as a search engine to find the optimum vertical path that maximizes harnessed power, where the vertical positions are shown as a discretized vector $\mathcal{Z} = [z_1, ..., z_n]$. Given a start depth $s \in \mathcal{Z}$ and the predicted ocean current velocities v_* over the $\mathcal{Z}$, the cost of transition (vertical movement) from the start depth

to any depths is defined by $-E(P_{\text{net}}(z(i), v_*(z(i), i)))$, with i denoting the time. The A* approach seeks feasible vertical positions (illustrated as a so-called open list in the A* algorithm), considering that the optimal vertical position at each time step justifies the minimum cost.

4.3.2 MPC-based Vertical Path Planning

MPC is considered in this section because of its capability to handle constrained problems. MPC is a powerful method for optimizing some objective functions by using a model of the system to be controlled to predict future states and actions. The objective is to maximize the output power of the MCT system. The objective function is formulated as a nonconvex optimization problem, which interprets the real power maximization objective of the MCT system with respect to the spatiotemporal ocean current velocity model, still facing nonlinearity and computational complexity. The constrained optimization problem which has to be solved by the MPC design is:

$$\mathbf{z}^*(p) = \arg\min_{\mathbf{z}(p)} \sum_{i=p}^{p+T-1} -E(P_{\text{net}}(z(i|p), v_*(i|p, z(i|p))) \tag{4.21a}$$

subject to

$$v_*(z(i|p), i|p) \sim f_* \sim \mathcal{GP}(m_*, \sigma_*^2) \tag{4.21b}$$

$$b(i+1) = b(i) + \zeta \Delta v + \kappa \Delta z \tag{4.21c}$$

$$z^{\min} \leq z(i|p) \leq z^{\max} \tag{4.21d}$$

$$\frac{z(i|p) - z(i-1|p)}{\Delta t_2} \leq r \tag{4.21e}$$

$$b^{\min} \leq b \leq b^{\max} \tag{4.21f}$$

$$\dot{b} \leq \dot{b}^{\max} \tag{4.21g}$$

where p denotes the p-th sampling time, T represents the prediction horizon. Define $\mathbf{z}(p) \triangleq [z(p|p), ..., z(p+T-1|p)]$, $\mathbf{z}^*(p) \triangleq [z^*(p|p), ..., z^*(p+T-1|p)]$. $v_*(z(i|p), i|p)$ denotes the predicted velocity. Constraint (4.21b) shows the GP model of ocean velocity to generate the ocean velocity prediction over the prediction horizon with mean m_* and covariance σ_*^2 (as explained in Section 4.2.1), and $z^{\min}$ and $z^{\max}$ are the minimum and maximum allowable depth. Constraint (4.21c) defines the fill fraction changes according to the changes in the flow speed and the MCT depth, which is detailed in Section 4.4.1. Other constraints formulate the fill fraction limits (4.21f) and fill fraction rate (4.21g). Note that the current optimal depth is chosen as the first element of the optimal decision variable sequence $\mathbf{z}^*(p)$.

The algorithm of MCT path optimization using MPC is presented in Algorithm 2. Firstly, all recorded ocean velocities and the prediction horizon T should be initialized. Then, v_* is predicted for each sampling time using (4.21b). The objective function is calculated over the prediction horizon while optimal depth is determined. Note that a sliding window is applied here, and only the first element from the optimal depth trajectory will be used in each sampling time. To solve the MPC-based optimization problem, we use dynamic programming (DP) by forward recursion, and to maintain the computational tractability, the optimization problem is defined over the depth-time grid (Figure 4.2). It should be noted that by using the DP, convergence to the global optimum is guaranteed subject to the ocean environment grid resolution. The continuous path planning takes care of finding an optimal path in a continuous underwater environment.

4.3.3 RL-based Vertical Path Planning

The RL is adopted here for its capability of learning a policy from historical data (i.e., data-driven), which could be robust to the environment model errors. The RL

Algorithm 2 Proposed MPC-based Design

Initialize n data sample $v(z,t)$, $i=0$, Δt_1, Δt_2, and T
for Each t **do**
    Construct the GP model (f_*) based on a fixed-size window of the observed data;
    for Prediction Horizon T **do**
        Predict v_* over T using the GP model $f_* \sim \mathcal{GP}(m_*, \sigma_*^2)$;
    end for
    Solve (4.21a) and obtain optimal depth trajectory $\mathbf{z}^*(p)$;
    Output optimal depth z^*;
end for

method takes the perspective of an agent (i.e., an MCT system in this study) that optimizes its behavior by interacting with the environment and learning from the feedback received. In the RL approach, the set of actions is done by the agent, and it receives the reward from the environment. Therefore, the learning procedure is completed for the agent from observing its resulted reward. Note that the whole RL algorithm includes three major sections (i) Environment: implementing the ocean environment defined by a grid of $n \times T$ or a continuous environment; (ii) Training: constructing the optimal RL table or network by performing the training procedure; and (iii) Testing: evaluating the constructed RL table or network through direct online testing.

It is critical to define the *set of states,* $s_i \in \mathcal{S}$, *actions,* $a_i \in \mathcal{A}$ and *rewards,* $r_i \in \mathcal{R}$. The long-term performance is optimized by learning a *policy* $\pi_\theta(a_i|s_i)$ for picking actions in state transition to maximize the total accumulated reward $R_T^\pi = \sum_{\tau=0}^{T} \gamma^\tau r_{i+\tau}$, where γ is the discount factor in $(0,1]$. As a reminder, the action of depth change at each time step should be determined to maximize the MCT net power.

State space: The net power of the MCT system is calculated in (4.10) as a function of the water depth z. We realize that the optimization gets more complicated when the prediction horizon T is considered. Transitions between different water depths $\mathbf{z}$ over the prediction horizon result in different net power. The state set is illustrated by the MCT position and underwater environment current velocity at t, i.e.,

$$S = \{z(t), v(t)\} \tag{4.22}$$

Action space: The action space is defined as a vector of feasible vertical positions for the MCT, where an action taken at t should enforce the MCT to reach the specified position at $t + 1$. The action space is formulated by

$$A = \{z_{\mathrm{e}}(t)\} \tag{4.23}$$

given that $z_{\mathrm{e}}(t) \triangleq z_{\mathrm{e}}^{\mathrm{d}}$ for the discrete gridded environment.

It is favorable to tune shaping reward functions with demonstrations of the ultimate objective of power maximization, which is separately formulated for each candidate RL algorithm to achieve the best performance. Since each RL algorithm follows a specific approach to find the optimal policy, it is predictable that the same reward function may not yield the best results for all methods. Note that different reward functions are tested, and the best reward function for each algorithm is presented here.

Three RL algorithms, including two approaches over the discrete environment and one for the continuous environment, are nominated to solve the MCT path planning problem. All algorithms are initially trained offline using the field-recorded data from the Gulf Stream, which is then applied in the online path planning.

Q-learning Algorithm: The Q-learning algorithm is assigned as the baseline algorithm among the RL algorithms, dealing with the problems defined over the gridded environment with a set of discrete actions. This algorithm employs a Q-table to store $Q(s, a)$ for all feasible states and actions, where the highest Q-value

Algorithm 3 Q-learning for path planning

1: **Input:** field-recorded current velocity, discrete spatial positions, and Q-learning parameters;
2: **Output:** optimal Q-table;
3: **for** each episode **do**
4: Sample an initial state $s \leftarrow \{z, v_{\mathrm{e}}\}$;
5: **for** each step of episode **do**
6: Accomplish $a \leftarrow z_{\mathrm{e}}^{\mathrm{d}}$ using ϵ-greedy policy (4.25);
7: Gain R^{Q} by (4.24), and update Q and s;
8: **end for**
9: **end for**

determines the optimal action taken at each state. The reward function to fulfill the power maximization is defined as follows:

$$R^{\mathrm{Q}} = \begin{cases} P_{\mathrm{net}} - P_{\mathrm{net}}^{\mathrm{b}}, & P_{\mathrm{net}} - P_{\mathrm{net}}^{\mathrm{b}} > \delta_1 \\ 0, & \text{otherwise} \end{cases} \tag{4.24}$$

where an action is rewarded while the power change is greater than a constant threshold of δ_1, and $P_{\mathrm{net}}^{\mathrm{b}}$ denotes a base net power parameter while keeping the current vertical position (i.e., no vertical movement).

To balance the exploration and exploitation, an ϵ-greedy approach is used, namely:

$$a = \begin{cases} \arg\max_a Q^{\pi}(s, a), & 1 - \epsilon \\ \text{random } a, & \epsilon \end{cases} \tag{4.25}$$

where $\epsilon = \epsilon_{\min} + (\epsilon_{\max} - \epsilon_{\min})e^{-d.e}$, with d being the decay factor, and e being the episode. The training of the Q-learning application for path planning is presented in Algorithm 3.

It is noteworthy to mention that the Q-value table approach suffers from the "curse of dimensionality" when scaling to the problems with high-dimensional action and

state spaces. To tame this deficiency, a deep Q-learning approach as a combination of the Q-learning and deep neural network can be applied to approximate the Q-value function, which is appropriate for a larger environment (especially a grid with a longer prediction horizon), as well as, enlarging the action decision variables (i.e., increasing the number of decision variables). Although the Q-value table is sufficient for the size of the ocean environment grid presented in the current study, we also apply a particular type of deep Q-learning called deep Q-network (DQN) to solve the problem at hand.

Deep Q-Network (DQN) Algorithm: The DQN approximates Q function with a neural network to deal with a large size state space and action space. This algorithm utilizes two neural networks with the same structure but different weights, where the weight of "target network" $Q(s, a|\theta'^{\mathrm{DQN}})$ is updated using the "Q-network" $Q(s, a|\theta^{\mathrm{DQN}})$. The DQN learns the optimal Q^* function through the optimal policy acquired by minimizing the following loss function:

$$\mathcal{L}(\theta^{\mathrm{DQN}}) = [Q(s(t), a(t); \theta'^{\mathrm{DQN}}) - Q(s(t), a(t); \theta^{\mathrm{DQN}})]^2 \tag{4.26}$$

with

$$Q(s(t), a(t); \theta'^{\mathrm{DQN}}) \triangleq R(t+1) + \gamma \max_a Q(s(t+1), a; \theta'^{\mathrm{DQN}}) \tag{4.27}$$

The reward function for the DQN algorithm is defined by two positive constant values ζ_1 and ζ_2 to avoid a high increase in the cumulative reward; the reward is given to the agent if it follows the increased velocity, as well as the increased power. This shaping of the reward function accelerates the training of the DQN by identifying a trend for the velocity increase and accordingly the power increase. The reward function is defined as follows:

$$R^{\mathrm{DQN}} = \varpi_1 R_{\mathrm{P}}^{\mathrm{DQN}} + \varpi_2 R_{\mathrm{v}}^{\mathrm{DQN}} \tag{4.28}$$

with

$$R_{\mathrm{P}}^{\mathrm{DQN}} = \begin{cases} \zeta_1, & P_{\mathrm{net}} - P_{\mathrm{net}}^{\mathrm{b}} > \delta_1 \\ 0, & \text{otherwise} \end{cases} \tag{4.29}$$

$$R_{\mathrm{v}}^{\mathrm{DQN}} = \begin{cases} \zeta_2, & v_{\mathrm{e}} - v_{\mathrm{e}}^{\mathrm{b}} > \delta_2 \\ 0, & \text{otherwise} \end{cases} \tag{4.30}$$

where the reward function consists of two terms due to the reward for power $R_{\mathrm{P}}^{\mathrm{DQN}}$, as well as velocity $R_{\mathrm{v}}^{\mathrm{DQN}}$ with ϖ_1 and ϖ_2 showing the constant coefficients; $v_{\mathrm{e}}^{\mathrm{b}}$ similar to $p_{\mathrm{net}}^{\mathrm{b}}$ defined in (4.24) denotes a base environment velocity parameter while holding the current vertical position.

The action is selected based on the same ϵ-greedy policy defined in (4.25). The algorithm of DQN for offline training is illustrated in Algorithm 4, where $\mathcal{D}$ denotes the experience replay memory.

Proximal Policy Optimization (PPO) Algorithm: To cope with the continuous states and actions, the PPO algorithm [129] is adopted in this letter. Let define the advantage function $\mathcal{A}$ as the difference between state-value and action-value functions $\mathcal{A}(s,a) = Q(s,a) - V(s)$. To build an estimate from the advantage function at t denoted as $\widehat{\mathcal{A}}(t)$, a critic network is used to approximate the value function $\widehat{V}$ and the advantage function estimation $\widehat{\mathcal{A}}(t)$ is defined by:

$$\widehat{\mathcal{A}}(t) = \delta(t) + (\gamma\lambda)\delta(t+1) + ... + (\gamma\lambda)^{T-t+1}\delta(T-1) \tag{4.31}$$

with

$$\delta(t) = R(t) + \gamma\widehat{V}(s(t+1)) - \widehat{V}(s(t)) \tag{4.32}$$

where T denotes the time horizon, γ denotes the discount factor, $0 \leq \lambda \leq 1$ denotes a parameter to bias the variance trade-off. The ultimate goal of the PPO is to maximize a "surrogate objective function", formulated as follows:

$$L^{\mathrm{CLIP}}(\theta^{\mathrm{PPO}}) = \widehat{\mathbb{E}}_t[\min(r(t;\theta^{\mathrm{PPO}})\widehat{\mathcal{A}}(t), \mathrm{clip}(r(t;\theta^{\mathrm{PPO}}), 1-\vartheta, 1+\vartheta)\widehat{\mathcal{A}}(t))] \tag{4.33}$$

Algorithm 4 DQN for path planning

Input: field-recorded current velocity, discrete spatial positions, and DQN parameters;
Output: optimal DQN;
for each episode **do**
    Sample an initial state $s \leftarrow \{z, v_{\mathrm{e}}\}$;
    for each step of episode **do**
        Accomplish $a \leftarrow z_{\mathrm{e}}^{\mathrm{d}}$ using ϵ-greedy policy (4.25);
        Gain R^{DQN} by (4.28), and update s;
        Store transition $(s, a, r, s^{'})$ in $\mathcal{D}$;
        Sample random mini-batch from $\mathcal{D}$;
        Calculate target Q-value by (4.27);
        Perform a gradient descent step on loss in (4.26);
        Update target network and update $\theta'^{\mathrm{DQN}} \leftarrow \theta^{\mathrm{DQN}}$ every c_1 steps;
    end for
end for

with $r(t;\theta^{\mathrm{PPO}}) = \frac{\pi(a,s;\theta^{\mathrm{PPO}})}{\pi(a,s;\theta'^{\mathrm{PPO}})}$ being the probability ratio with $\pi(a, s; \theta'^{\mathrm{PPO}})$ representing the old policy, which is clipped to stay within a constant range of $[1-\vartheta, 1+\vartheta]$. The reward function is defined according to the continuous nature of the action and state spaces:

$$R^{\mathrm{PPO}} = \varsigma_1 R_{\mathrm{P}}^{\mathrm{PPO}} + \varsigma_2 R_{\mathrm{v}}^{\mathrm{PPO}} \tag{4.34}$$

with

$$R_{\mathrm{P}}^{\mathrm{PPO}} = \mathrm{clip}(\frac{P_{\mathrm{net}} - P_{\mathrm{net}}^{\mathrm{des}}}{P_{\mathrm{net}}^{\mathrm{des}}}, -1, +1) \tag{4.35}$$

$$R_{\mathrm{v}}^{\mathrm{PPO}} = \mathrm{clip}(\frac{v_{\mathrm{e}} - v_{\mathrm{e}}^{\mathrm{des}}}{v_{\mathrm{e}}^{\mathrm{des}}}, -1, +1) \tag{4.36}$$

where the reward function includes two terms corresponding to the velocity and power

Algorithm 5 PPO for path planning

1: **Input:** field-recorded current velocity, continuous spatial positions, and PPO parameters;
2: **Output:** optimal PPO;
3: **for** each iteration **do**
4: Sample an initial state $s \leftarrow \{z, v_{\mathrm{e}}\}$;
5: Run policy $\pi(.;\theta'^{\mathrm{PPO}})$ over T and take $a \leftarrow z_{\mathrm{e}}$;
6: Calculate advantage function estimates over T by (4.31) using R^{PPO} in (4.34);
7: Perform a gradient ascent on the surrogate function in (4.33);
8: Update $\theta'^{\mathrm{PPO}} \leftarrow \theta^{\mathrm{PPO}}$ every c_2 iterations;
9: **end for**

with ς_1 and ς_2 denoting the constant coefficients; $v_{\mathrm{e}}^{\mathrm{des}}$ and $P_{\mathrm{net}}^{\mathrm{des}}$ denote large values as desired velocity and power.

The PPO algorithm for the path planning is outlined in Algorithm 5.

4.4 SIMULATION RESULTS FOR PATH PLANNING

We use real ocean velocity data and the example buoyancy-controlled MCT that is discussed in Section 4.2. Recorded ocean velocities $\mathbf{V}$ are modeled by the GP model in (4.9). At each time step, the ocean velocity v_* is predicted over the prediction horizon. The predicted velocity is then considered as the observed velocity, and the next velocity is predicted by a sliding prediction window. Based on predicted ocean velocities, the optimal ocean depth z^* is determined. Key parameters used in the simulation for path planning are presented in Table 4.2. Also, the main parameters for the RL algorithms are presented in Table 4.3, where a network with two hidden layers is selected with a batch size of 64. All the experiments were conducted on a PC equipped with a 2.3 GHz CPU and 32 GB of RAM.

MCT system specification: The theoretical model of the investigated MCT

Table 4.2: Key parameters used in the path planning optimization.

Symbol	Description	Value	Unit
P_{r}	Rated power	700	[kW]
ρ	Water density	1030	[kg/m^3]
A	Swept area of the MCT rotor	100π	[m^2]
C_{p}	Average power coefficient	41.5	[%]
η_{pump}	Pump efficiency	0.75	-
P_{atm}	Atmospheric pressure	101	[kPa]
g	Gravity	9.81	[m/s^2]
Q_{B}	Volumetric flow rate	0.023	[m^3/s]
ν_{B}	Volume of each ballast tank	31.251	[m^3]
ζ	Coefficient in (4.17)	0.65	[s/m]
Δt_1	Sampling time to hold depth in (4.18)	0.25	[hours]
κ	Coefficient in (4.19)	-0.0026	[1/m]
Δt_2	Sampling time to change depth in (4.20)	1	[hour]
$b^{\min}$	Minimum buoyancy tank fill fraction	0	–
$b^{\max}$	Maximum buoyancy tank fill fraction	1	–
$\dot{b}^{\max}$	Maximum slew rate of fill fraction	7.45×10^{-4}	[1/s]
T	Prediction horizon	2	[hours]
n	Number of discrete depths	27	-
$z^{\min}$	Minimum allowable depth	50	[m]
$z^{\max}$	Maximum allowable depth	150	[m]

system is presented in Section 4.2.3. Assuming an MCT operating depth of $z_{\mathrm{opt}} = 50\,\mathrm{m}$, the relationship between pump power and volumetric flow rate is determined using (4.14):

$$P_{\mathrm{B_{max}}}^{\mathrm{empty}} = \frac{606 Q_{\mathrm{B_{max}}}}{0.75} = 808 Q_{\mathrm{B_{max}}} \tag{4.37}$$

Table 4.3: Key parameters used in the RL algorithms.

Symbol	Description	Value	Unit
δ_1	Power threshold in (4.24) and (4.29)	1	[kW]
$\epsilon_{\min}$	ϵ-greedy coefficient	0.01	-
$\epsilon_{\max}$	ϵ-greedy coefficient	1	-
d	ϵ-greedy decay factor	0.01	-
e	ϵ-greedy episode	3000	-
γ^{Q}	Q-learning discount factor	0.5	-
ϖ_1	Coefficient in (4.28)	1	-
ϖ_2	Coefficient in (4.28)	0.5	-
ζ_1	Constant reward in (4.29)	1	-
ζ_2	Constant reward in (4.30)	1	-
δ_1	Velocity threshold in (4.29)	1	[kW]
δ_2	Velocity threshold in (4.30)	0.001	[m/s]
γ^{DQN}	DQN discount factor	0.5	-
ς_1	Coefficient in (4.34)	0.8	-
ς_2	Coefficient in (4.34)	0.2	-
P^{des}	Desired Power in (4.35)	700	[kW]
$v_{\mathrm{e}}^{\mathrm{des}}$	Desired Velocity in (4.35)	2	[m/s]
γ^{PPO}	PPO discount factor	0.5	-
λ^{PPO}	PPO variance bias parameter	0.9	-

It should be noted that the volumetric flow rate and ballast pump power are calculated associated with WWII submarines [112]. Accordingly, the power and energy to empty two ballast tanks are calculated as $P_{\mathrm{B}}^{\mathrm{empty}} = 18.8$ and $E_{\mathrm{B}}^{\mathrm{empty}} = 14.02$, respectively, with respect to (4.37) and values presented in Table 4.2. The linear quasi-static relationship is interpreted for a flow speed of 1.6 m/s. In our application, the depth

is limited within 50 m to 150 m since the maximum ocean currents nearly always occur in the top 150 m depths [6].

Ocean current shear profile: In this section, we use the data recorded by a 75 kHz ADCP at a latitude of 26.09°N and longitude of −79.80°E. ADCPs measuring water velocity data over 300+ m can make approximately one measurement per second, have a vertical spatial resolution of around 6 m, and typically save time-averaged water velocity measurements every 3 to 15 minutes to reduce measurement noise. The data include measures of northward current velocity, eastward current velocity, and data quality related parameters. To save battery, data used in this study were recorded every 15 minutes with 25 measurements averaged to create each recording, yielding an estimated measurement error standard deviation of 0.02 m/s throughout the water column (based on the ADCP's manufacturer specification found in [130]). Recorded data were filtered to remove bad data through the method suggested in [6], with "bad" data primarily measured above a depth of 50 m. "Bad" data were identified using ADCP correlation and percent good, as well as the echo intensity spikes characteristic of the initial return of side lobe acoustics reflecting from the sea surface. The ocean shear profile calculated from these data over a sample one-week period is shown in Figure 4.3. To expand the spatiotemporal path planning algorithms from this section to real turbine applications, an ADCP will likely be installed just upstream from an ocean current turbine, or array of turbines, so that near real-time current velocity data are accessible.

4.4.1 MCT Operating Depth Assessment for Linear Model and Nonlinear Model

To derive the MCT output power model, certain approximations are made to represent the nonlinear model with linear quasi-static relationships. The major approximations are included in (4.17) and (4.19) to determine the relationship between the fill fraction

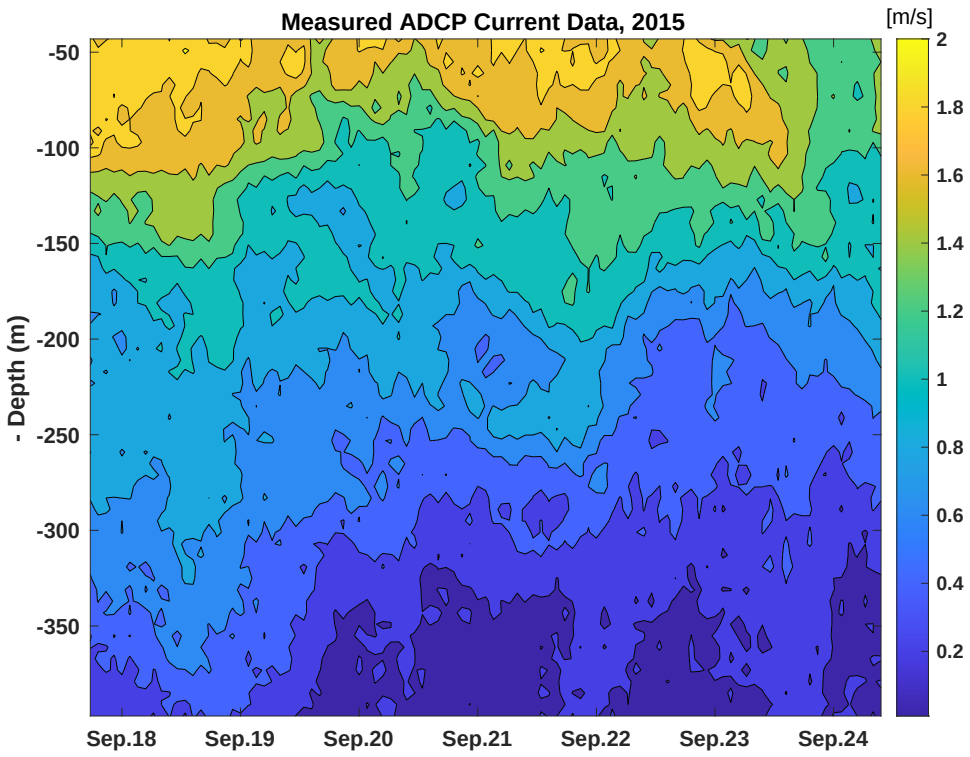

Figure 4.3: Sample ocean current shear profile recorded by an ADCP in the Gulf Stream over one week.

change and flow speed change as well as depth change. Hence, the fill fraction is affected by two parameters of depth and velocity, and the whole fill fraction equation can be rewritten as follows:

$$\Delta b = \zeta \Delta v + \kappa \Delta z \tag{4.38}$$

where $\Delta \triangleq (.) - (.)_{\text{eq}}$ given that $b_{\text{eq}} = 0.5$, $z_{\text{eq}} = 50$ m, and $v_{\text{eq}} = 1.6$ m/s.

To justify the accuracy of the presented linear model in (4.38), the MCT operating depth obtained through the nonlinear model is compared with those calculated by (4.38). The operating depths associated with the specified flow speeds and fill fractions (equal values for both tanks) are shown in Figure 4.4. Note that the operating depths are illustrated under the sea surface, where the MCT's ballast tank hits the surface if the MCT system is located at a depth of 15.34 m. As this figure

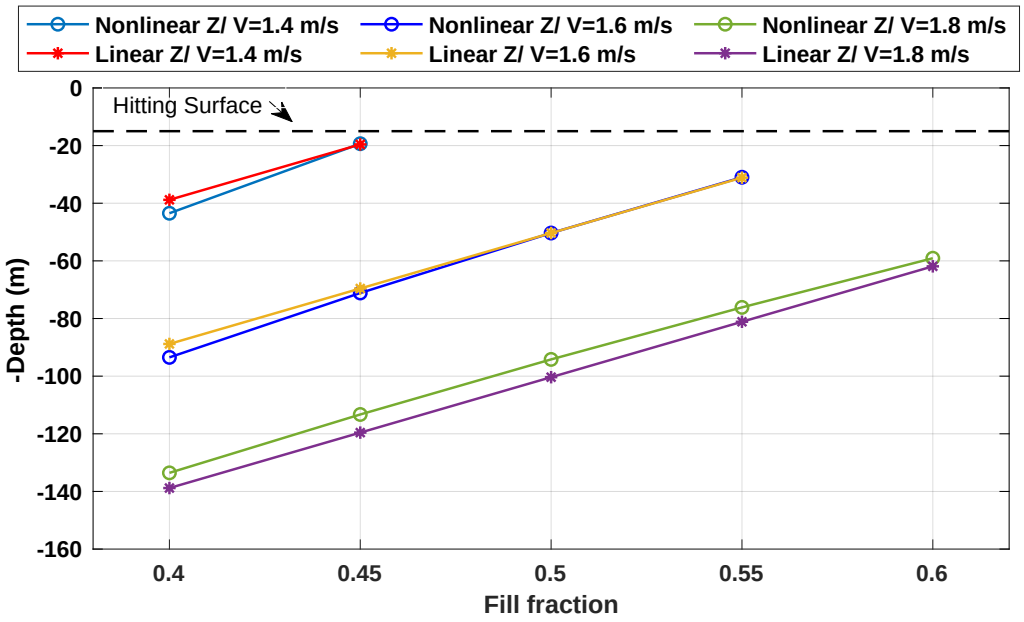

Figure 4.4: Comparison of equilibrium depths associated with the specified flow speeds and fill fractions (equal values for both tanks), found using both the nonlinear and linear models. It is noted that fill fractions of 0.5 for each tank and a flow speed of 1.6 m/s are utilized when creating the linear model.

shows, the operating depth calculated by the linear model (4.38) matches those obtained through the nonlinear model, where a negligible difference is anticipated due to approximations made to attain the linear model from a nonlinear model.

4.4.2 Comparative Results

To evaluate the performance of the proposed methods for MCT vertical path planning, the following four approaches are compared:

- Case without Spatiotemporal Optimization: The MCT is located at a fixed depth, which means no change in operating depth, i.e., the output power of the system is determined only by the ocean velocity at the operating depth.

- Path Planning with A* Algorithm: One commonly used algorithm for grid-

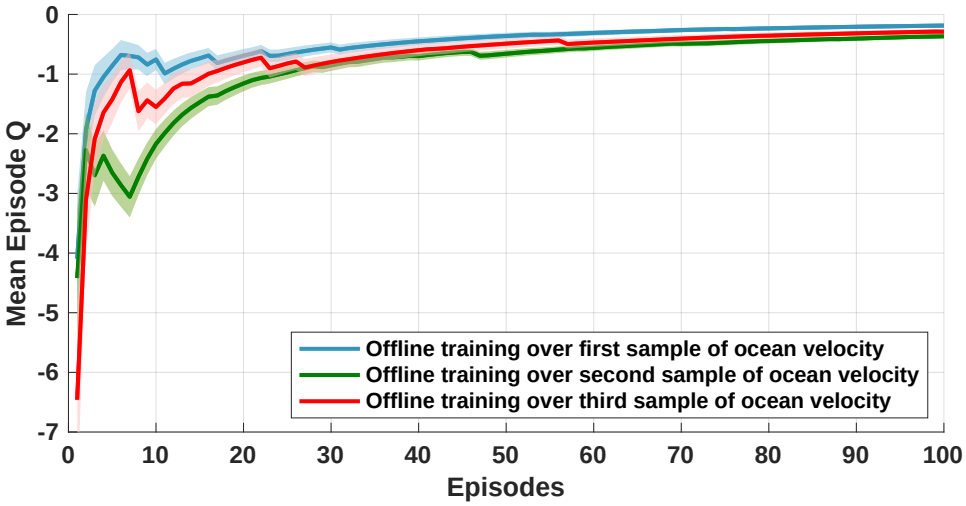

Figure 4.5: Average Q-values over 100 trial episodes are shown for offline training over the first sample of ocean velocity, second sample of ocean velocity, and third sample of ocean velocity. Solid lines show average Q-values, and the shaded region determines a 95% confidence interval.

based path planning is the A* algorithm, which can efficiently seek the ocean environment grid and find the optimal path [76]. The A* algorithm applies a greedy strategy, where the heuristic function is defined by the expected power. The heuristic function is applied to label each path and generate a weighted grid (or graph), which is further employed to find the optimal path.

- MPC-based Spatiotemporal Optimization: The optimal operating depth z^* is determined using objective function $J(z(p))$ in (4.21a), which aims to maximize the harvested power at each time step.

- RL-based Spatiotemporal Optimization: Learning from different experiments should be considered to update the RL algorithm. We first evaluate the Q-learning algorithm as a baseline approach among the RL approaches and justify its performance with MPC and A* algorithm. The algorithm is trained offline by multiple trials, and the cumulative Q-values over trial episodes are shown in

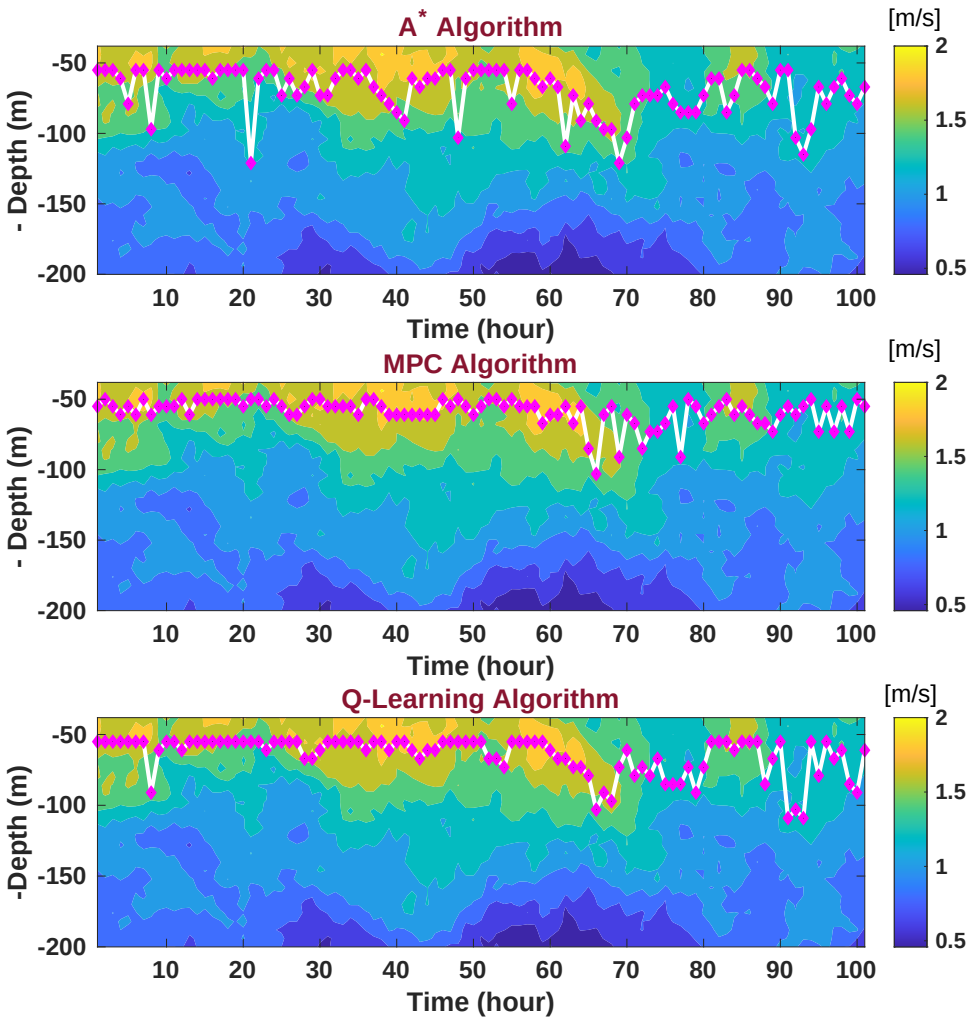

Figure 4.6: Comparing optimal path obtained over 100 hours under A* algorithm, MPC-based optimization, and Q-learning-based optimization.

Figure 4.5, which verifies the convergence of Q over 100 episodes for different sampling time. After training the RL algorithm, it is applied for online testing.

The obtained results over a sample simulation time of 100 hours are presented in Figure 4.6 to Figure 4.7. The optimal path obtained over 100 hours with A* algorithm, MPC algorithm, and Q-learning algorithm are illustrated in Figure 4.6. The control action is defined as the depth change in this study, and the optimal depth and the corresponding velocity are shown under the A* method, MPC-based

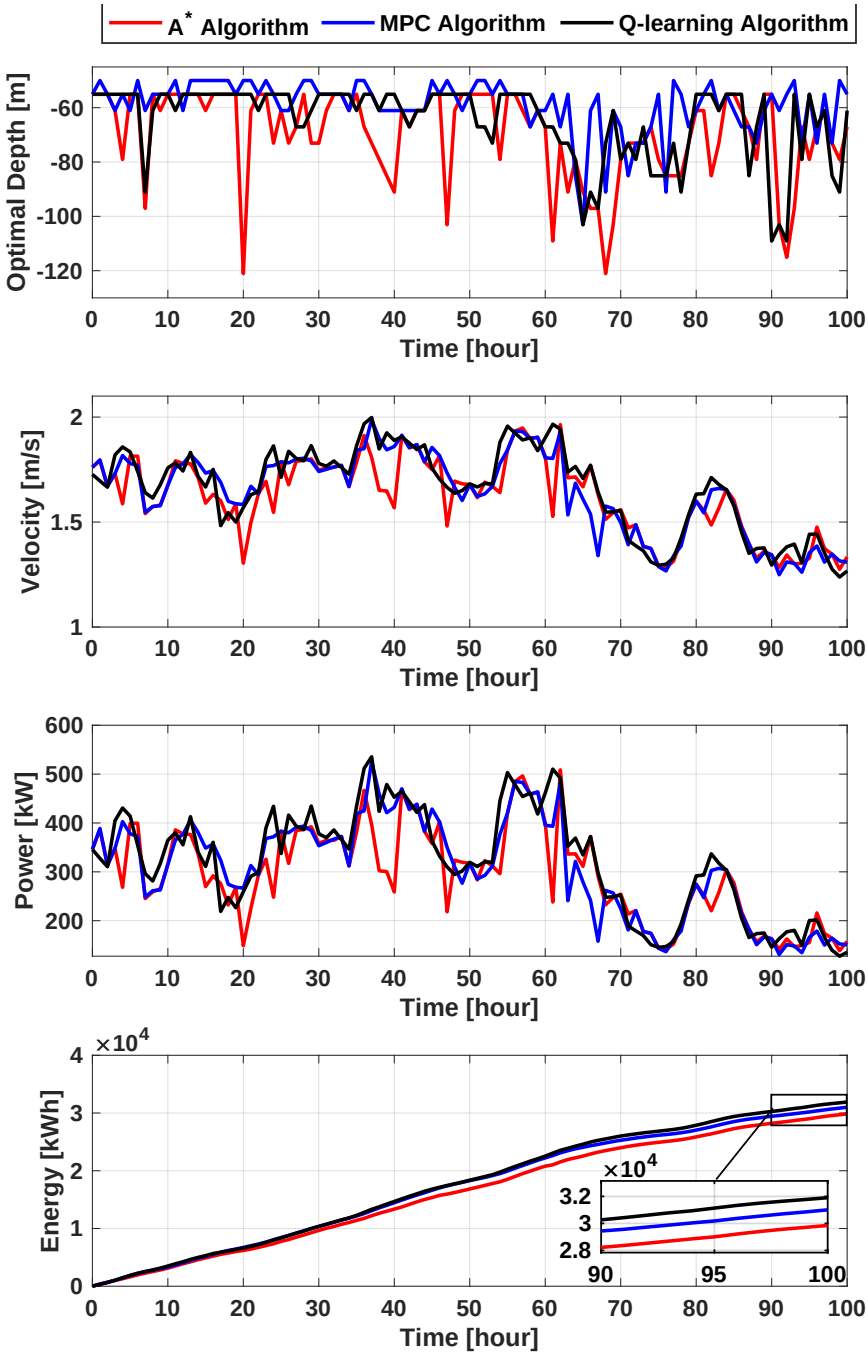

Figure 4.7: Comparing optimal depth and velocity over 100 hours obtained by case without spatiotemporal optimization, A* algorithm, MPC algorithm, and Q-learning-based algorithm. In this figure, (a) optimal depth, (b) optimal velocity, (c) optimal power, and (d) optimal energy are shown.

method, Q-learning method, and the case without spatiotemporal optimization. As presented in Figure 4.7, the optimal paths show similarities, especially for the Q-learning algorithm and MPC algorithm. However, there exist noticeable differences in selecting the next control action, such as at $t = 90$. Although different z are selected as the next optimal depth for each algorithm, the velocities at these depths are nearly the same (Figure 4.7), verifying that these algorithms can make optimal decisions.

The cumulative produced energy of the MCT system using the A* algorithm, the MPC algorithm, and the Q-learning algorithm are compared, as shown in Figure 4.7. Q-learning algorithm outperforms the remaining methods, and the final energy production for the A* algorithm, the MPC algorithm, the Q-learning algorithm, and case without applying spatiotemporal optimization are 29.812 MWh, 30.772 MWh, 31.920 MWh, and 26.657 MWh, respectively. The cumulative energy shows an increase compared to the case without optimization, highlighting the importance of applying path planning algorithms. We also observe that the cumulative energy productions of the MCT system are very close for different compared optimization approaches.

Robustness Analysis: For an evaluation of the spatiotemporal optimization robustness, the proposed methods are implemented by the perturbed ocean velocity, in which the ocean velocity is not correctly modeled due to the scale error in the velocity sensors, the data loss from measurement, and so on [131]. Figure 4.8 shows the perturbation of cumulative energy from baseline obtained by the A* algorithm, the MPC algorithm, and the Q-learning algorithm in response to 5% noise disturbances of the same intensities for 100 test cases. We can observe that the Q-learning algorithm is sufficiently robust, where a similar distribution of the results (i.e., cumulative energy) is obtained for the perturbed ocean velocity model. Moreover, the Q-learning algorithm outperforms the MPC algorithm, and the perturbed results (i.e., that in a small interval [31.623 $\sim$ 32.148] MWh) is very close to the obtained cumulative

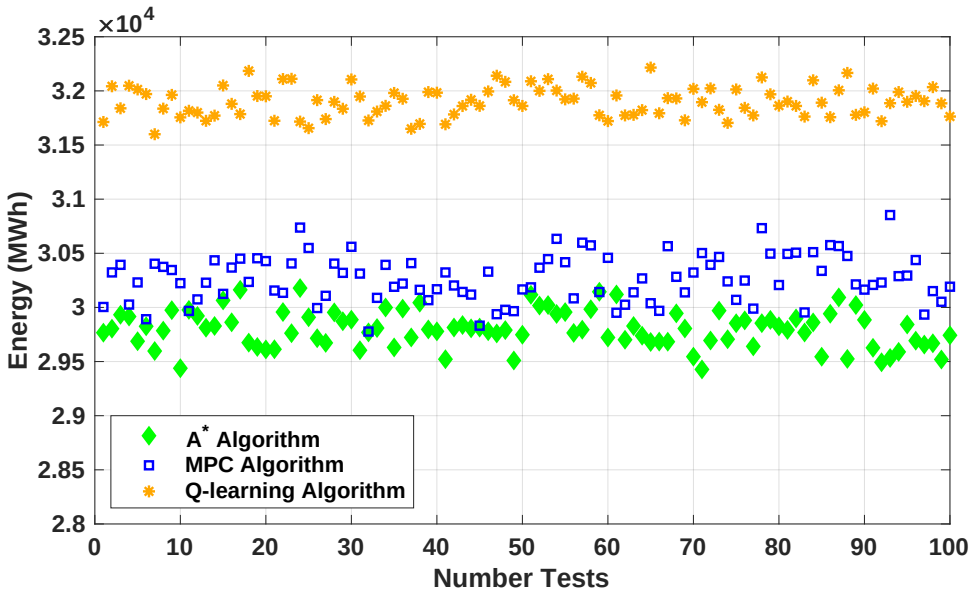

Figure 4.8: Robustness comparison of the A* algorithm, MPC algorithm, and Q-learning-based algorithm through cumulative energy under noise.

energy for baseline case without noise (31.920 MWh).

To further show the robustness of our proposed methods, the cumulative energy of the A* algorithm, the MPC algorithm, and the Q-learning algorithm in response to noise disturbances, ranging from 5% to 20%, for 100 test cases are presented in Table 4.4. Note that the results are reported as an average of the cumulative energy obtained by 100 tests. As can be seen from the table, the superiority of the Q-learning method over other methods is verified under these four cases, justifying that the A* algorithm and MPC algorithm are more sensitive to the increased ocean velocity modeling error.

Comparative Results for RL Algorithms: After verifying the performance of the Q-learning algorithm as a baseline RL algorithm with other approaches, we now compare the results obtained through three candidate RL algorithms, including Q-learning, DQN, and PPO algorithms. The convergence results for DQN and PPO algorithm are shown in Figure 4.9, which demonstrates that the PPO training needs

Table 4.4: Comparing the robustness in percent decrease of cumulative energy using accurate ocean velocity model vs. perturbed ocean velocity models.

Noise	A* Algorithm		MPC Algorithm		Q-learning Algorithm	
[%]	[MWh]	[%]	[MWh]	[%]	[MWh]	[%]
Baseline Ocean Velocity Model						
-	29.812	-	30.772	-	31.920	-
Ocean Velocity Model Perturbed with Noise						
5	29.030	2.63	29.772	3.25	31.733	0.59
10	28.303	5.07	29.174	5.19	31.009	2.86
15	27.633	7.31	28.712	6.70	30.472	4.54
20	27.136	8.98	28.271	8.13	29.661	7.08

more episodes than the DQN due to the larger action and state spaces in the continuous space, where the training episode takes 6.7 s for DQN and 0.107 s for PPO. Hence, the PPO is significantly faster than the DQN for the training per episode, but it needs almost three times more episodes to be fully trained. It should be noted that different values for the reward are gained by using two separate reward functions for DQN (4.28)-(4.30) and PPO (4.34)-(4.36).

Figure 4.10 illustrates the vertical positions found through the path planning, as well as the corresponding current velocity, net power, and cumulative energy harvested from the MCT. The planned path by the Q-learning induces a globally optimal path due to the gridded environment precision, which is used as a baseline for the DQN algorithm as a representative of the deep RL algorithms for the gridded environment. Therefore, it is justified by the experimental results that the DQN is able to successfully find the optimal path (similar to the Q-learning except for one position at the time step of 68). Meanwhile, the PPO algorithm solves the path planning problem in a continuous environment facing a large set of feasible vertical positions,

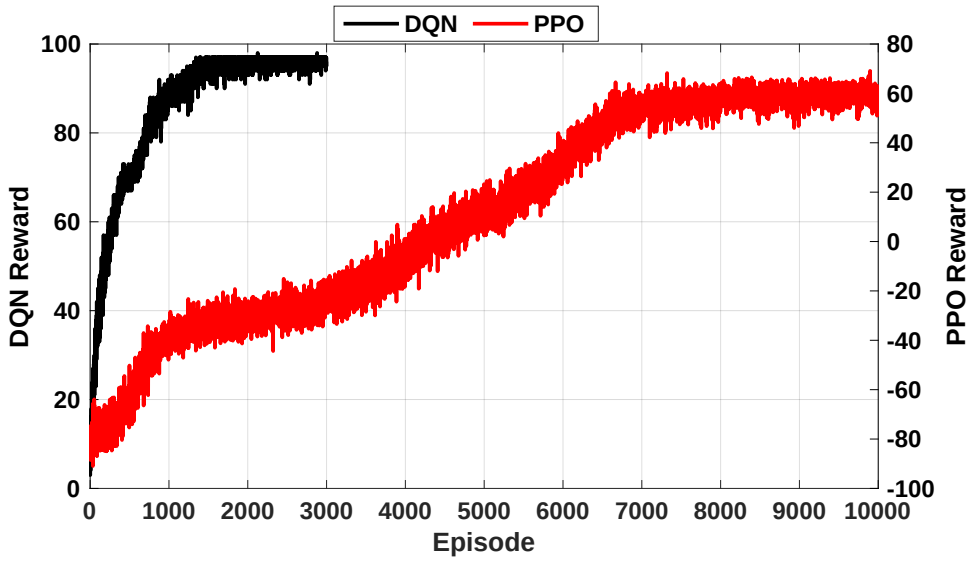

Figure 4.9: Cumulative reward for: (i) DQN when the reward (black line) converges after 3000 episodes; and (ii) PPO when the reward (red line) converges after 10000 episodes.

thereby increasing the complexity of the problem but upbringing a capability of larger space exploration to find a better optimal path than the discrete gridded environment. From the obtained vertical positions, the PPO follows almost a similar trend with the discrete approaches with increased precision in opting the positions. The PPO algorithm outperforms the discrete algorithms in terms of current velocity and harvested power, resulting in cumulative energy of 34.585 MWh over 100 hour compared to the harvested energy in the case of Q-learning (31.920 MWh) and DQN (31.822 MWh). Switching from a discrete environment to the continuous one leads to an intensive complexity but a higher accuracy in path planning, where caution should be taken to evaluate the required precision due to application and then making a selection between discrete and continuous approaches.

Comparative Results for PPO and Continuous MPC: To give a fair comparison, we also solve the MPC over the continuous oceanic environment. This so-

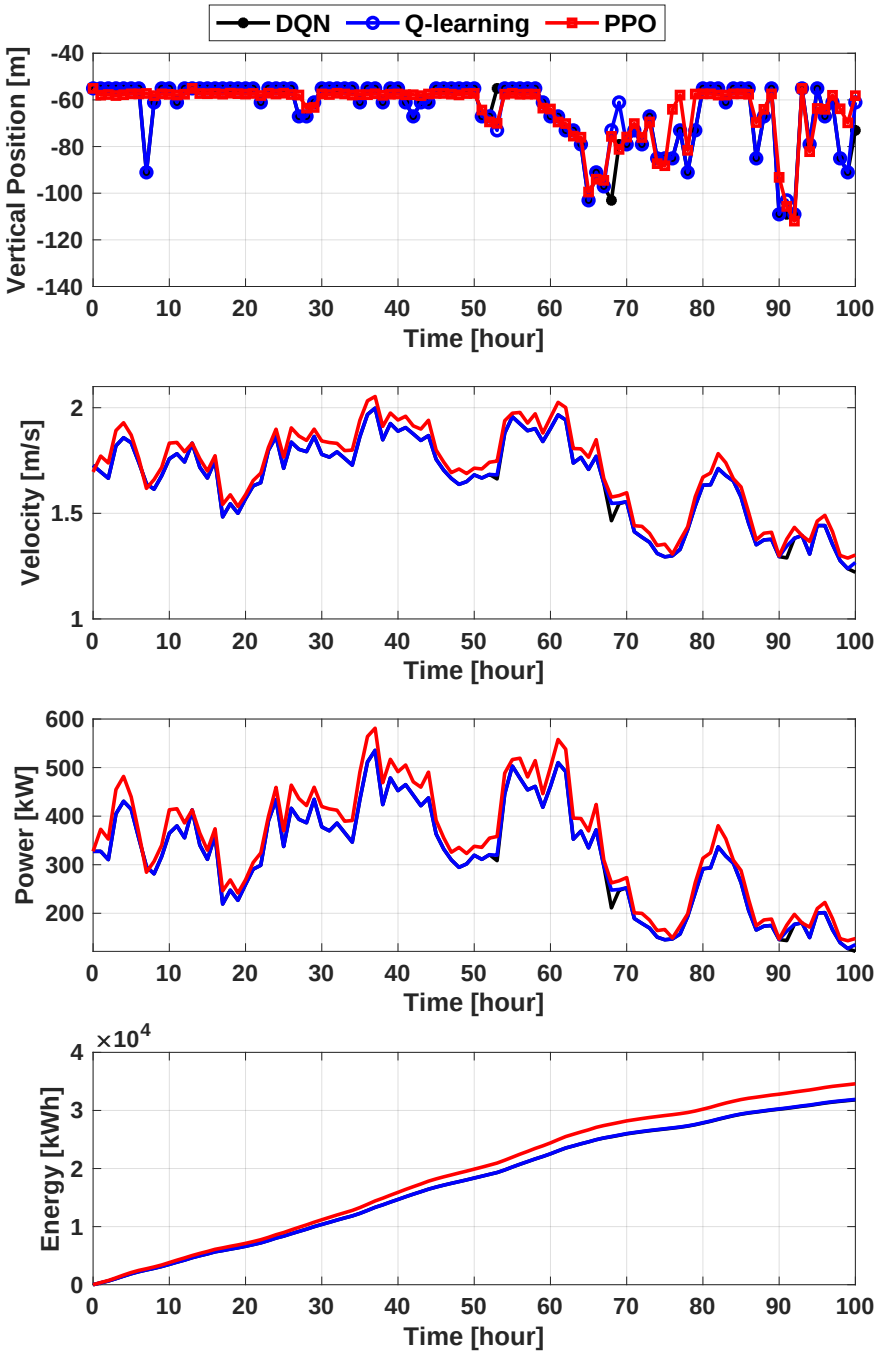

Figure 4.10: Comparative results (vertical position, velocity, power, and energy) obtained by Q-learning, DQN, and PPO algorithms.

called continuous MPC is real-time path planning, which takes care of finding an optimal path in a continuous underwater environment. There are two approaches to

solving the continuous MPC, including

(i) *Continuous Path Planning:* The optimal vertical path is planned for the autonomous MCT operating in the continuous ocean environment. A sequence of optimal depth is obtained over a prediction horizon.

(ii) *Reinforced Continuous Path Planning:* The initial optimal path is found by the discrete MPC-based path planning, which is then given to the continuous path planning to improve the final solution by taking advantage of both discrete and continuous representations from the ocean environment.

To solve this nonlinear optimization problem, the "fmincon" solver of the Matlab optimization toolbox is used. The obtained results show that the cumulative energy for the continuous MPC and the reinforced continuous MPC are 31.007 MWh and 32.386 MWh after a 100-hour operation. Although the results show an increase compared to the discrete MPC (30.772 MWh), the PPO algorithms still outperform the continuous MPC algorithms.

4.5 INTEGRATED PATH PLANNING AND TRACKING FOR MCT

Till this section, the main assumption is that the MCT is capable of following the optimal path obtained by the path planning algorithm, which is constrained with the major operational constraints of the MCT instead of considering the detailed plant dynamics. To address the coupled MCT path planning/tracking control problem, we develop an *integrated control* framework. The goal of the proposed architecture is to plan a cost criterion-optimal path and to track this optimal path, generally formulated in discrete-time in the following. The path planning problem is fully explained in the previous sections so that the main focus in this section is on the path tracking and integrated control framework.

Figure 4.11 visualizes the proposed integrated framework, which contains two phases of offline training phase and online phase. In the offline phase, the planner is

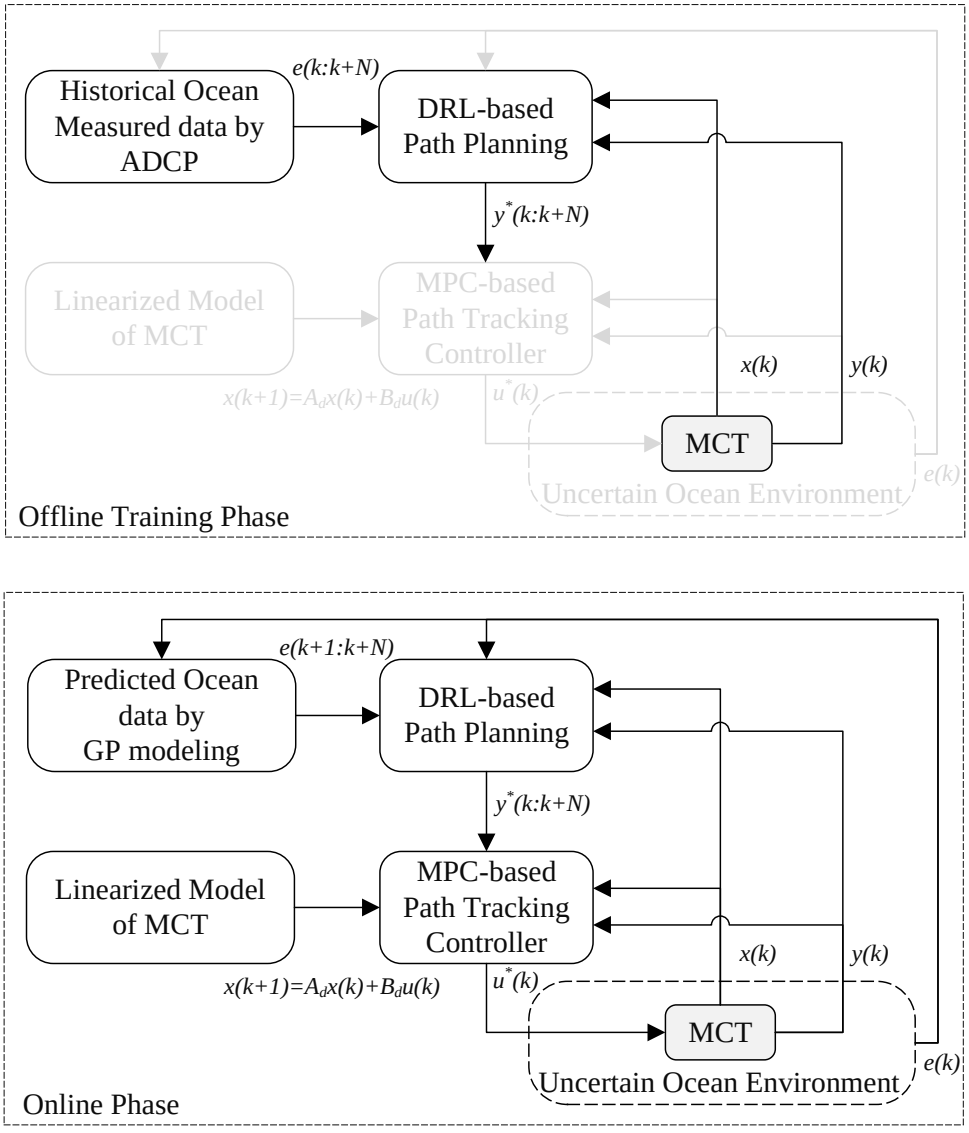

Figure 4.11: Proposed integrated path planning and tracking control framework for marine current turbine.

trained due to the historical ocean environment profile to seek the best path. In the online phase, at each iteration, the path planner takes the previous iteration's state, $x(k)$, and environmental data, $e(k)$, to generate an optimal path $y^*(k)$. At each discrete-time instant, k, the path tracking controller follows the commanded optimal path. To be more specific, the path planner solves the spatiotemporal optimization

problem to maximize the harnessed power, where the optimal path satisfies the constraints corresponded to the uncertain ocean model. A learning-based approach will be utilized to find the optimal path through learning from the historical environment profile. The path tracker follows the optimal path assigned by the path planner and computes feasible control inputs, $u(k)$, to minimize the tracking error by taking into account the linearized model of the plant subject to the system constraints. An MPC-based approach will be applied to address the optimization problem as a quadratic programming problem using the linearized MCT model (details in Section 4.5.1).

Remark. *The imposition of a learning-based approach, DRL, for the upper-level path planning is significant to address the highly uncertain environment through learning from the historical ocean environment profile. On the other hand, in the presence of the dynamic model of the plant, the selection of an analytical approach, MPC, for the lower-level path tracking ensures to successfully follow the assigned optimal path robustly, without violating the system's limitations. The result of this framework is an integrated control approach that satisfies path planning in an uncertain environment and path tracking using a detailed plant model.*

4.5.1 Path Tracking through Model Predictive Control

The path tracking will minimize the distance between the plant's current path and the optimal path commanded by the path planner. MPC, as a powerful model-based algorithm, is chosen to address path tracking due to the complex dynamics consisting of multiple states and the availability of a detailed MCT model.

Model Predictive Control (MPC): To design an MPC for the discrete linear

model of the MCT defined in (4.43), the following cost function must be minimized:

$$\begin{aligned}\tilde{V} \equiv & \frac{1}{2}\Bigg(\sum_{i=k+1}^{k+N_t-1}\Big((y(i|k)-y^*(i))^T Q_{\text{part}}\,(y(i|k)-y^*(i))\Big) \\ & + \sum_{i=k}^{k+N_c-1}\Big((u(i|k)-u(i-1|k))^T R_{\Delta\text{part}}\,(u(i|k)-u(i-1|k)) \\ & + (u(i|k)-d(i))^T R_{\text{part}}\,(u(i|k)-d(i))\Big) \\ & + (y(k+N_t|k)-y^*(k+N_t))^T Q_{\text{term}}\,(y(k+N_t|k)-y^*(k+N_t))\Big)\end{aligned} \tag{4.39a}$$

$$u^{\min}(i) \leq u(i) \leq u^{\max}(i) \tag{4.39b}$$

$$\Delta u^{\min}(i) \leq \Delta u(i) \leq \Delta u^{\max}(i) \tag{4.39c}$$

$$y^{\min}(i) \leq y(i) \leq y^{\max}(i) \tag{4.39d}$$

where N_t and N_c are the prediction horizon and the control horizon, respectively; $d(i)$ is a vector of the arbitrary user-selected target controls at time step i, Q_{part} and Q_{term} are the weight factors for the states and the final state point, respectively. Finally, $R_{\Delta\text{part}}$ and R_{part} are the weight factors for the control input changes and the desired control inputs, respectively. Constraints (4.39b)-(4.39c) impose that control input and control input change should stay within a predefined bound. Constraint (4.39d) captures the need to bound the system output. Here, $(.)^{\min}(i)$ and $(.)^{\max}(i)$ are the minimum and maximum values of $(.)(i)$.

After the algebraic manipulations as given in [132], the cost function is converted to the quadratic form, which is then minimized using the interior-point method, subject to the constraints given in (4.39b)-(4.39d).

MPC-based Path Tracking: In our problem, we leverage the path tracking algorithm to obligate the plant to follow the optimal path with a minimum error subject to system constraints. Considering the MCT with a high number of coupled states and the requirement of handling many constraints, MPC provides a controller that meets the desired objectives in a guaranteed manner. Also, the user-defined

weights bring flexibility about choosing the more important states in the plant to be followed while giving less priority to the other states that are relatively less crucial for the desired performance. MPC is designed to minimize the cost function as given in (4.39a), in which the weights are defined to prioritize the states to follow the trajectory with the minimum error. The reference path is defined in the vector of target outputs, $y^*(i)$, and at each sampling time, the updated reference is received from the DRL-based path planner. Algorithm 6 describes the MPC-based path tracking. The constraints of the MPC solver are defined based on the MCT design and specifications. Since the desired performance is to track the depth reference, the related state, z, has the only weight defined in Q_{part} and the rest is set to be zero as $Q_{\text{part}} = \text{diag}(0,0,0,0,0,0,0,0,0,1,0,0,0)$. The other rates are defined as $Q_{\text{term}} = I_{13}, R_{\text{part}} = 0$, and $R_{\Delta\text{part}} = I_3$, where I_n is the $n \times n$ identity matrix.

4.5.2 MCT Linear Model

To form the linear state space model for the MCT system, the equations of motion are averaged around the nominal condition (equilibrium point), thereby formulating the linear model as follows:

$$\delta\dot{\mathbf{x}}_{n\times 1} = A_{n\times n}\delta\mathbf{x}_{n\times 1} + B_{n\times m}\delta\mathbf{u}_{m\times 1} \tag{4.40}$$

Here, the states $\delta\mathbf{x}$ and control inputs $\delta\mathbf{u}$ are defined as deviation from the nominal condition. $\delta\mathbf{x} \in \mathbb{R}^n$ and $\delta\mathbf{u} \in \mathbb{R}^m$ with n and m denoting the number of states and control inputs used by the linear model ($n = 13$ and $m = 3$ in our MCT system), namely:

$$\delta\mathbf{x} = [\delta u\ \delta v\ \delta w\ \delta p_b\ \delta p_r\ \delta q\ \delta r\ \delta x\ \delta y\ \delta z\ \delta\phi\ \delta\theta\ \delta\psi]^{\text{T}} \tag{4.41}$$

$$\delta\mathbf{u} = [\delta b_{\text{f}}\ \delta b_{\text{a}}\ \delta\tau_{\text{em}}]^{\text{T}} \tag{4.42}$$

where the control inputs are defined by forward buoyancy tank fill fraction b_{f}, aft buoyancy tank fill fraction b_{a}, and τ_{em}. It is noted that the linear model has one less state

Algorithm 6 Model predictive control for path tracking

Discretize the continuous linear model based on Shannon's Theorem;
Initialize the linear model inside the MPC solver;
Initialize the constraints for the actuators and the system states;
Initialize N_t, N_c, Q_{part}, Q_{term}, $R_{\Delta\text{part}}$ and R_{part};
Initialize the initial state and control inputs;
for $i = 1$ *to* $N_{\text{operation}}$ **do**
    Initialize the reference trajectory based on the optimal waypoint path from the DRL;
    for $j = 1$ *to* $N_{\text{operation-int}}$ **do**
        Apply the interior-point method, select u^* for N_c over N_t;
        Solve the cost function $\tilde{V}$ in (4.39a) and obtain optimal $[u^*(i|N_c), ..., u^*(i|i + N_c - 1)]$;
        Apply $u^*(i|N_c)$ to the DLTI plant and obtain the next system state $x(i+1)$;
    end for
    Update the position error and send a feedback to DRL;
end for

than the non-linear model as the rotor rotation angle state, ϕ_{r}, is eliminated during the linearization process as described in [116]. Given that the nominal condition is defined by an averaged homogeneous flow speed of $v_{\text{eq}} = 1.6$ m/s, the nominal states and control inputs are characterized by $x_{\text{eq}} = [0\ 0\ 0\ 0\ 1.49\ 0\ 0\ 554.50\ 0.38\ 50\ 0.01\ 0.00\ 3.14]$ and $u_{\text{eq}} = [0.4677\ 0.4677\ -188280]$.

Furthermore, since the real-time path controller is designed in discrete-time with future objectives of implementation in a real plant (e.g., an MCT-based power plant), the linearized model is discretized using a sampling time, T_{s}, determined by the Nyquist-Shannon's sampling theorem [133]. The corresponding discrete linear time-

invariant (DLTI) plant model at discrete-time instant k is:

$$x(k+1) = A_{\mathrm{d}}x(k) + B_{\mathrm{d}}u(k) \tag{4.43}$$

where

$$A_{\mathrm{d}} = \begin{bmatrix} -0.315 & -0.080 & -0.003 & -0.217 & -0.217 & -0.495 & 0.196 & 0.029 & 0.000 & -0.025 & 0.007 & -0.839 & -0.011 \\ 0.000 & -0.141 & 0.609 & 0.273 & 0.000 & 1.534 & 2.156 & 0.000 & -0.000 & 0.000 & 1.229 & -0.063 & 0.310 \\ -0.077 & -0.470 & -0.172 & -0.060 & -0.059 & -1.022 & 1.210 & 0.012 & 0.000 & -0.011 & 0.003 & -3.577 & -0.046 \\ 0.000 & -0.048 & -0.004 & -0.654 & 0.000 & -0.021 & -0.382 & 0.000 & -0.000 & 0.000 & -1.660 & -0.004 & 0.193 \\ 0.545 & 0.000 & 0.000 & -0.259 & -0.259 & 0.000 & 0.000 & 0.000 & 0.000 & 0.000 & -0.471 & -0.000 & -0.001 \\ -0.012 & -0.044 & -0.002 & -0.009 & -0.009 & -0.308 & 0.108 & 0.000 & 0.000 & 0.001 & -0.000 & -0.602 & -0.006 \\ 0.000 & 0.011 & -0.064 & 0.005 & 0.000 & -0.152 & -0.375 & 0.000 & 0.000 & 0.000 & 0.274 & 0.011 & -0.135 \\ -1.000 & 0.002 & -0.000 & 0.000 & 0.000 & 0.000 & 0.000 & 0.000 & 0.000 & 0.000 & 0.000 & 0.000 & 0.000 \\ -0.002 & -1.000 & 0.012 & 0.000 & 0.000 & 0.000 & 0.000 & 0.000 & 0.000 & 0.000 & 0.000 & 0.000 & 0.000 \\ -0.000 & 0.012 & 1.000 & 0.000 & 0.000 & 0.000 & 0.000 & 0.000 & 0.000 & 0.000 & 0.000 & 0.000 & 0.000 \\ 0.000 & 0.000 & 0.000 & 1.000 & 0.000 & 0.000 & 0.000 & 0.000 & 0.000 & 0.000 & 0.000 & 0.000 & 0.000 \\ 0.000 & 0.000 & 0.000 & 0.000 & 0.000 & 1.000 & -0.012 & 0.000 & 0.000 & 0.000 & 0.000 & 0.000 & 0.000 \\ 0.000 & 0.000 & 0.000 & 0.000 & 0.000 & 0.012 & 1.000 & 0.000 & 0.000 & 0.000 & 0.000 & 0.000 & 0.000 \end{bmatrix} \tag{4.44}$$

$$B_{\mathrm{d}} = \begin{bmatrix} 0.005 & -0.086 & 0.000 \\ -0.001 & -0.007 & 0.000 \\ -0.238 & -0.564 & 0.000 \\ -0.002 & -0.002 & -0.000 \\ 0.000 & 0.000 & 0.000 \\ 0.003 & -0.047 & 0.000 \\ 0.000 & 0.001 & 0.000 \\ 0.000 & 0.000 & 0.000 \\ 0.000 & 0.000 & 0.000 \\ 0.000 & 0.000 & 0.000 \\ 0.000 & 0.000 & 0.000 \\ 0.000 & 0.000 & 0.000 \\ 0.000 & 0.000 & 0.000 \end{bmatrix} \tag{4.45}$$

4.5.3 Simulation Results for Integrated Path Planning and Tracking

We evaluate the proposed path planning and path tracking for our designed MCT. For the tracking controller, the horizons are selected as $N_{\mathrm{t}} = 40$, and $N_{\mathrm{c}} = 20$ considering

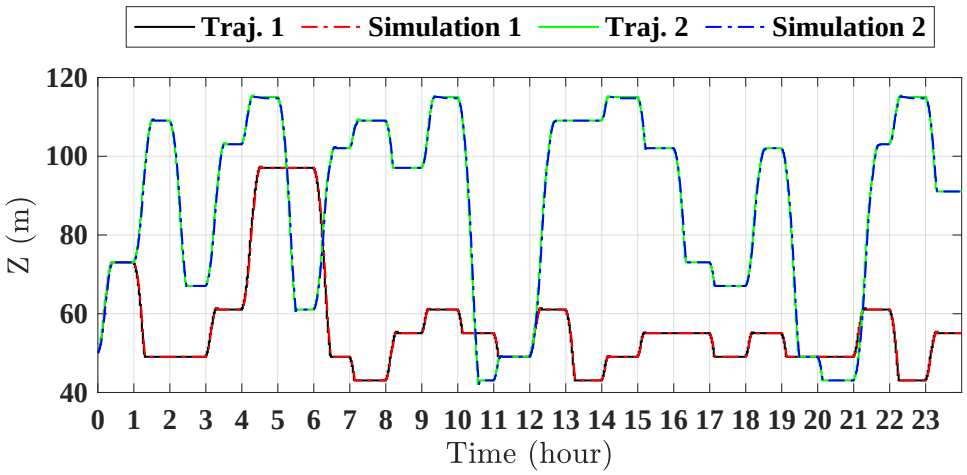

Figure 4.12: Trajectory followed by the MCT along with the optimal reference trajectory for two ocean shear profiles.

the system's performance with highly-limited actuator slew rates.

The goal is to maximize the net power of the MCT through modifying the operating water depth z (i.e., vertical path planning), where the tracking controller tracks the optimal depth with the minimized error. After the path planning, the z trajectory is sent to the tracking controller, where the error is minimized through (4.39a). Figure 4.12 shows the trajectory followed by the MCT along with the optimal reference trajectory for two shear profiles, verifying that the proposed path tracking controller successfully follows the assigned optimal path by the path planner for the entire trajectory. It is shown that the path planner is able to find the optimal trajectory over low and high shear profiles, where the MCT also navigates the commanded reference paths. Results show the efficiency of the path planner in finding the optimal path to maximize the net power, where the total harvested power after 24 hours shows an over 9% increase compared to the baseline case (the MCT maintains at $z_{\text{eq}} = 50$ m without path planning). Note that the baseline case is selected based on the equilibrium depth of the MCT, which can produce the highest power while keeping a constant depth. Figure 4.13 demonstrates that the Euler angles of the MCT remain

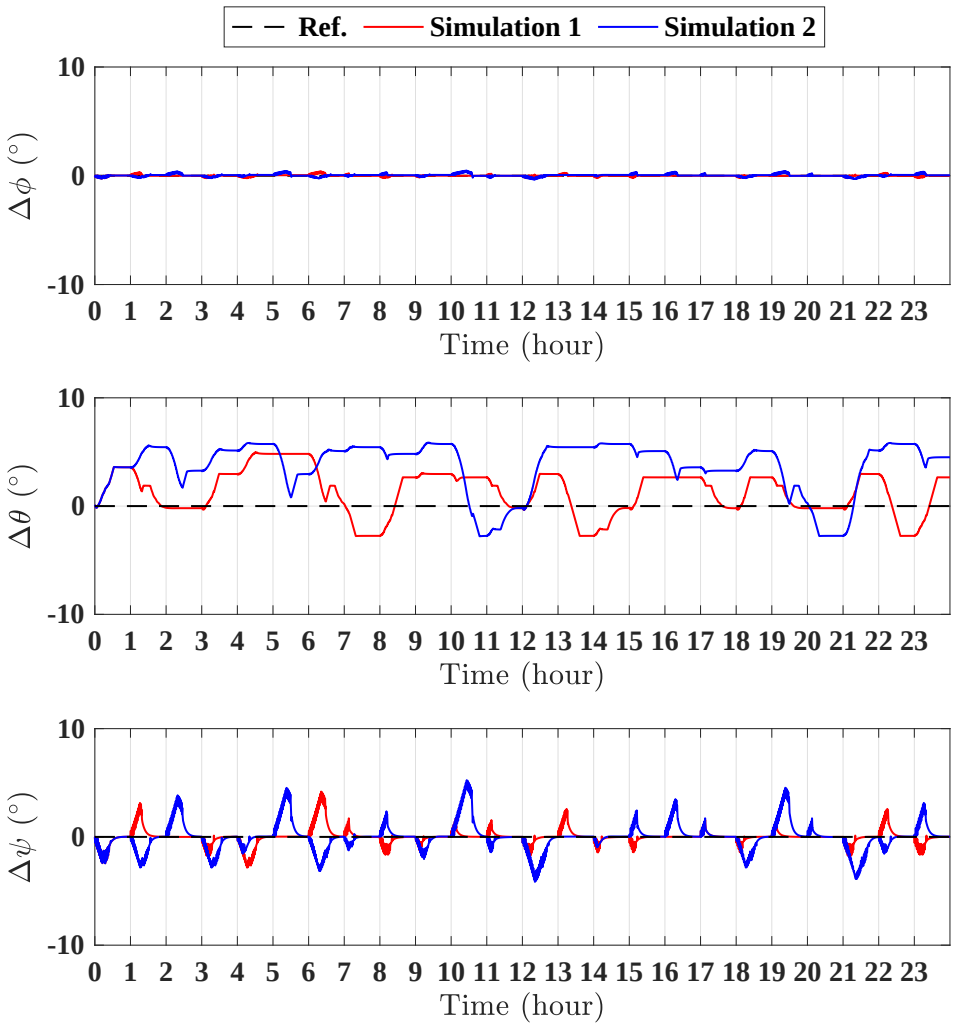

Figure 4.13: Euler angles of the MCT system for two ocean shear profiles.

within the acceptable bounds (±6°), and Figure 4.14 illustrates the control inputs applied to the MCT to track the reference trajectory, where the control inputs do not violate the limits.

4.6 CONCLUSION

In this chapter, a novel spatiotemporal optimization approach was presented for MCT vertical path planning to maximize the net power. The GP model was first developed to model the ocean velocity based on real data. Then, the MCT power models were

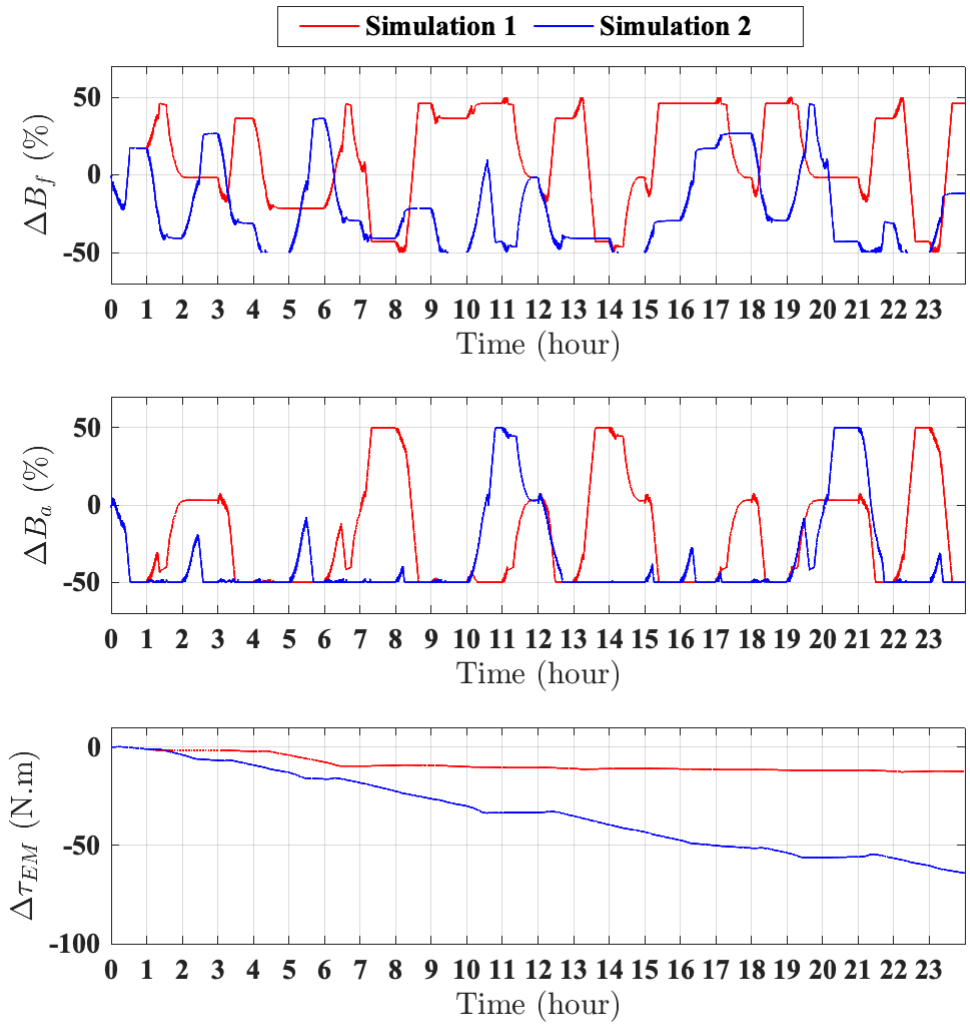

Figure 4.14: Control inputs applied to the MCT system to track the reference trajectory for two ocean shear profiles.

formulated, including the directly generated power from hydrokinetic energy, the consumed power for stabilizing, and the consumed power for changing the operating depth. Two types of methodologies, including MPC- and RL-based algorithms, were developed to solve the proposed spatiotemporal problem. Compared with the baseline approaches, the obtained results verify that both methods are efficient in finding the optimal path to maximize the output power.

Moreover, we presented an integrated path planning and tracking control framework for the MCT wherein the planner was designed using a DRL approach to develop

a strategy in order to optimize a cost criterion (maximizing the harvested power from the MCT). The tracking control was addressed through an MPC approach considering the linear model of the system obtained from the nonlinear dynamic model. The proposed approach was applied to a buoyancy controlled MCT, and the numerical results verified that our proposed approach is able to maximize the net power through path planning. Results also demonstrate that the tracking controller can effectively track the optimal path by considering the sluggish dynamics while avoiding any aggressive motion and instability.

CHAPTER 5

CONTROL CO-DESIGN FOR BUOYANCY CONTROLLED MCT

Recent research progress has confirmed that using advanced controls can result in massive increases in energy capture for MHK energy systems, including MCTs and wave energy converters (WECs); however, to realize maximum benefits, the controls, power-take-off system, and basic structure of the device must all be co-designed from early stages. In this chapter, we present an MCT turbine control co-design framework, accounting for the plant geometry and spatiotemporal path planning to optimize the performance. Developing a control co-design framework means that it is now possible to evaluate the effects of changing plant geometry on a level playing field when accounting for the MCT plant power optimization. The investigated framework evaluates the key design parameters, including the sizes of the generator, rotor, and variable buoyancy tank in the MCT system, and formulates these parameters' effect on the MCT model and harnessed power through defining a power-to-weight ratio, subject to the design and operational constraints. The control co-design is formulated as a nested optimization problem, where the outer loop optimizes the plant geometry and the inner loop accounts for the spatial-temporal path planning to optimize the harnessed power with respect to the linear model of the MCT system and ocean current uncertainties. Compared with a baseline design, results verify the efficacy of the proposed framework in co-designing an optimal MCT system to gain the maximum power-to-weight ratio.

Our main contribution in this chapter is to present a turbine geometric and spatiotemporal control co-design to maximize the power-to-weight ratio of a buoyancy-controlled MCT and analyze the whole design from ocean currents to power generation

to ensure that it is optimal.

5.1 PROMINENT DESIGN PARAMETERS IN MCT

The first task here is to identify the dominant design parameters in the MCT based on the nonlinear model and the performance of the MCT presented in Chapter 3. A prominent design of the MCT system may entail several prerequisites: (i) harnessing the maximum power while tethered to the anchor; (ii) conducting a real-time search to find the vertical position with the maximum power subject to consuming the minimal power to relocate the MCT system; and (iii) acquiring the maximum power with a minimum MCT weight. We repeat the equation for the power generation for the MCT system with emphasizing on that the generated power is limited by the generator rated power:

$$P_{\mathrm{MCT}} = \min(\frac{1}{2}\rho\pi(\frac{d}{2})^2 v^3 c_{\mathrm{p}}, P_{\mathrm{g}}^{\mathrm{r}}) \tag{5.1}$$

The prominent design parameters are represented in Figure 5.1. To address these conditions, the dominant design parameters of the MCT system should be pointed out:

5.1.1 Rotor

The rotor is a key parameter in the MCT system design, directly affecting the whole system design and power generation. To highlight the importance of the rotor, a complete study on the hydrodynamic design of the MCT's rotor (airfoil size and shape with the corresponding power and thrust coefficients) has been conducted in [40]. On account of the results obtained through [40], the main focus in the current study is on *rotor diameter*. Larger rotor diameters increase the power production from MCT systems operating in a homogeneous flow field in the order of the square of the rotor diameter (see (5.1)), but with increased hydrodynamic system drag/thrust

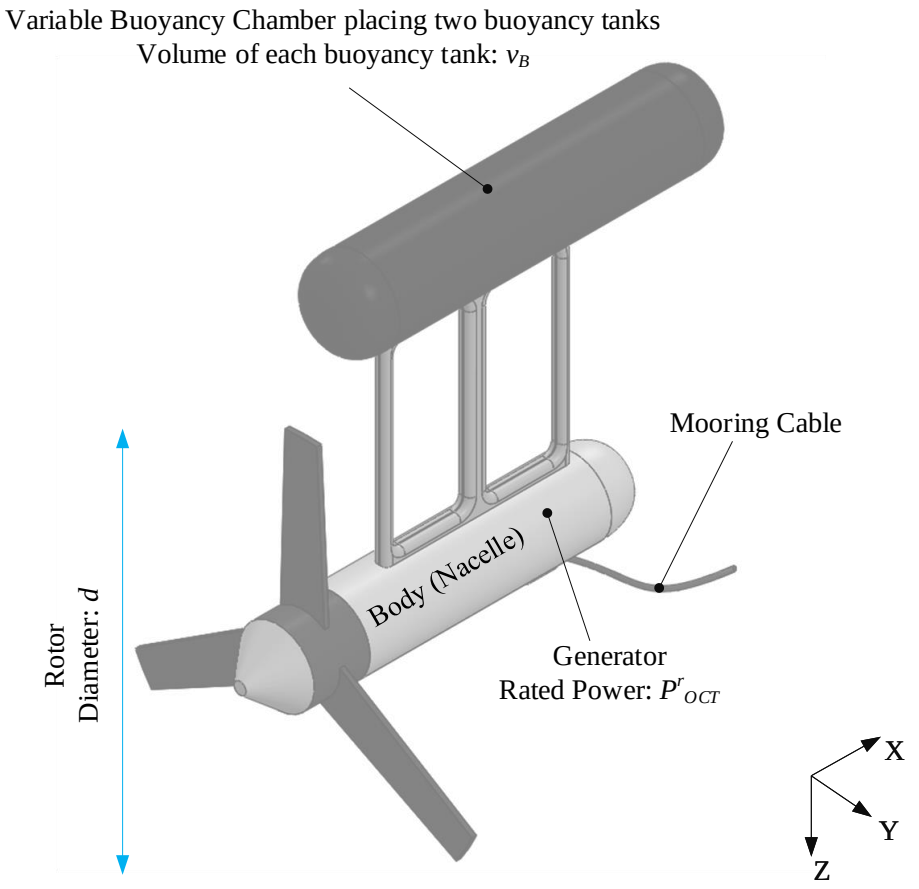

Figure 5.1: Schematic diagram of the buoyancy-controlled MCT and its prominent design parameters.

(also a function of the square of the diameter) and increased weight. The increased drag/thrust force on the rotor requires increased buoyancy forces to maintain the same elevation, which can be achieved by maintaining less water in the buoyancy tanks. However, for higher flow speeds, this increases the minimum achievable operating depth (i.e., depth when buoyancy tanks are completely filled with air), resulting in a decrease in the available energy density as available energy is typically strongest near the sea surface.

5.1.2 Buoyancy Tank

In our investigated MCT system, the buoyancy tank is another important design parameter that keeps the system afloat. Accordingly, the operating depth of the tethered MCT plant is initially determined through the amount of water in the tank, thereby imposing constraints on the vertical forcing and movement based on tank size. The results obtained previously suggest that the buoyancy tank size is not optimally designed since the MCT system can operate in a wide range of depth (e.g., $z = 27$ m to 216 m for a flow speed of 2.5 m/s) and can hit the depth of 50 m even with a strong flow speed of 2.5 m/s. Note that in the buoyancy tank, a pump drives water while setting the tank's pressure at vacuum pressure ($\cong 0$ kPa). Therefore, the key design parameter is the *tank size* (denoted as ν_{B} for the volume of each of the two buoyancy tanks). A larger tank size allows for the larger movement of the MCT, but increases the system's weight and cost.

5.1.3 Generator

To design a reliable and efficient MCT plant, the generator configuration plays an important role, limiting the power produced from the ocean currents (again, see (5.1)). In the current control co-design framework, the primary concentration is on the *generator rated power*. Picking a generator with a large rated power allows an electrical power output that is directly related to available hydrodynamic power from the ocean currents, however, at the expense of increased generator size, weight, and cost. Therefore, optimizing generator power rating to maximize the power-to-weight ratio (a surrogate for the cost of electricity) requires site specific energy resource data (commonly measured through the "power density" [6]).

5.2 PROPOSED CONTROL CO-DESIGN FRAMEWORK FOR MCT

A nested control co-design framework is developed with the objective of maximizing the power-to-weight ratio of the MCT plant; note that the power corresponds to the average power over the sampling time. The investigated architecture undertakes a combined geometric, structural design, and path planning to advance the performance of the MCT. Operating in a nested format, the framework consists of two main loops: the power-to-weight maximization outer loop addressed through the GA algorithm and the power-harnessing maximization inner loop solved by the MPC approach. A schematic of the proposed framework is shown in Figure 5.2. The GA method is applied to vary the design parameters and find the optimal value for these design parameters. To start the GA, a set of initial design parameters (denoted as a population in the GA method) are randomly generated, which is passed to the inner loop of spatiotemporal power optimization to calculate its corresponding optimal power. To find the optimal MCT design, each population should be ranked according to a so-called *fitness*, which is defined by the power-to-weight ratio. The MPC-based inner loop seeks to find a sequence of the optimal depths over prediction horizon T to maximize the harnessed power from the MCT for each population received from the outer loop.

Specifically, the control co-design is formulated as an optimization problem that seeks to maximize the power-to-weight ratio (transferring from maximization to minimization through multiplying the objective function by -1), subject to the operational and design constraints:

$$J(\upsilon) = \min_{\upsilon} \frac{-P}{m_{\mathrm{t}}} \tag{5.2}$$

s.t.

$$\upsilon^{\min} \leq \upsilon \leq \upsilon^{\max} \tag{5.3}$$

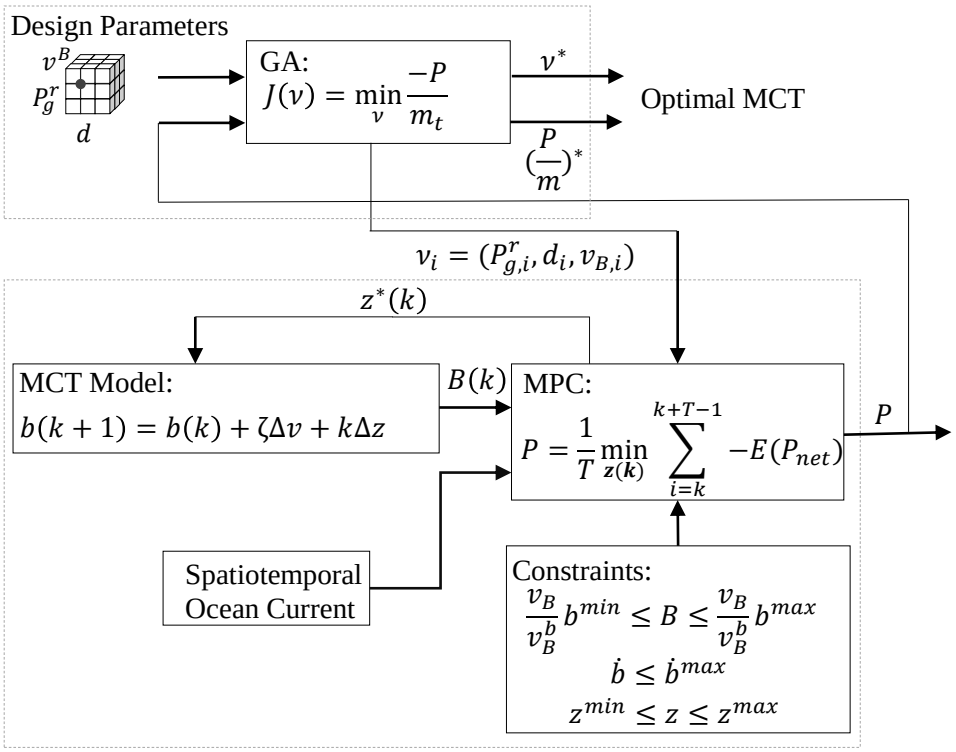

Figure 5.2: Proposed control co-design framework for optimizing the power-to-weight ratio, while accounting for the MCT geometry and spatiotemporal path control.

$$P = \frac{1}{T}\min_{\mathbf{z}(k)} \sum_{i=k}^{k+T-1} [-E(P_{\text{net}}(z(i|p), v_*(i|p, z(i|p))))] \tag{5.4}$$

$$m_{\text{t}} = m_{\text{t}}^{\text{b}} + \Delta m_{\text{r}} + \Delta m_{\text{g}} + \Delta m_{\text{B}} \tag{5.5}$$

Assuming that the inner spatiotemporal power optimization (through vertical path planning) is formulated by:

$$P = \frac{1}{T}\min_{\mathbf{z}(k)} \sum_{i=k}^{k+T-1} [-E(P_{\text{net}}(z(i|p), v_*(i|p, z(i|p))))] \tag{5.6}$$

s.t.

$$b(k+1) = b(k) + \zeta\Delta v + \kappa\Delta z \tag{5.7}$$

$$\frac{\nu_{\text{B}}}{\nu_{\text{B}}^{\text{b}}} b^{\min} \le b \le \frac{\nu_{\text{B}}}{\nu_{\text{B}}^{\text{b}}} b^{\max} \tag{5.8}$$

$$\dot{b} \leq \dot{b}^{\max} \tag{5.9}$$

$$z^{\min} \leq z(i|k) \leq z^{\max} \tag{5.10}$$

where $\upsilon = [P_{\mathrm{g}}^{\mathrm{r}},\ d,\ \nu_{\mathrm{B}}]$ are decision variables, including generator rated power, rotor diameter, and buoyancy tank size. Define $\mathbf{z}(k) \triangleq [z(k|k), ..., z(k|k+T-1)]^{\mathrm{T}}$. m_{t} is the total mass, consisting of the base mass, $m_{\mathrm{t}}^{\mathrm{b}}$, and mass deviations arising from changing the design parameters (i.e., rotor Δm_{r}, generator Δm_{g}, and variable buoyancy Δm_{B}). Notation $z(i|k)$ represents the value of z at time i given its value at time k. Constraint (5.7) is rewritten based on the fill fraction equation due to changes in flow speed and depth change presented in (4.38). Constraints (5.8) and (5.9) represent the limitations on the fill fractions. The major control objective of the spatiotemporal power optimization is to plan the vertical path for the MCT system, where constraint (5.10) limits the vertical movement of the system. The MPC-based spatiotemporal objective function in (5.6) can be minimized using either "dynamic programming (DP) by forwarding recursion" over the discrete oceanic environment or "fmincon" over the continuous environment to find the global minimum.

Here, the main challenge is to relate the mass deviation terms to the design parameters. To do this, two expressions initially formulated for the wind turbine's rotor and generator (recognized as one of the most similar plant to the MCT system) are extracted from the previous study [134]. To cope with the MCT system, it is important to set the coefficient α_1 in the rotor mass expression (5.11) according to the increased mass of the MCT rotor in comparison with the wind turbine's rotor. In this study, the MCT's rotor is designed based on an FX-83-W hydrofoil (see [40] for details), outperforming other rotor designs in generating more power P_{MCT}. Hence, the mass deviations of the rotor and generator are:

$$\Delta m_{\mathrm{r}} = \alpha_1 (\frac{d_{\mathrm{r}}^{\mathrm{b}}}{2} + \frac{\Delta d}{2})^{\alpha_2} - m_{\mathrm{r}}^{\mathrm{b}} \tag{5.11}$$

$$\Delta m_{\mathrm{g}} = \beta_1 (p_{\mathrm{g}}^{\mathrm{r,b}} + \Delta p_{\mathrm{g}}^{\mathrm{r}})^{\beta_2} - m_{\mathrm{g}}^{\mathrm{b}} \tag{5.12}$$

The equation for the variable buoyancy tank is formulated according to our previous numerical simulations study, namely:

$$\Delta m_{\mathrm{B}} = \gamma_1 \Delta \nu_{\mathrm{B}} \tag{5.13}$$

where α_1, α_2, β_1, β_2, and γ_1 are the coefficients as presented in Table 5.1.

5.3 SIMULATION RESULTS

The efficacy of the proposed control co-design framework is tested on our designed MCT. The base design parameters are presented in Table 5.1. The simulations are fully conducted in Python on a machine equipped with a 2.3 GHz CPU and 32 GB of RAM. For the MPC-based spatiotemporal power optimization algorithm, the time step is set as 1 hour, the prediction horizon is set as $T = 2$ hours, and the number of discrete depths is 17 within the allowable depth range (i.e., between $z_{\min}$ and $z_{\max}$ as presented in Table 5.1). Note that the selection of sampling time and prediction horizon for the problem at hand is justified through a comparative analysis on different prediction horizons and sampling times. The design parameters are assumed to change within $\upsilon^{\min} = 0.1 \times \upsilon^b$ and $\upsilon^{\max} = 1.1 \times \upsilon^b$ to help ensure that the compatibility is maintained with the MCT components that are satisfied at their baseline values. Also, to introduce spatiotemporal uncertainties of the ocean currents into our model, we use a set of real measured ocean data at a latitude of $26.09°N$ and longitude of $-79.80°E$ by a 75 kHz acoustic Doppler current profiler (ADCP) with a vertical resolution of 5 m within 400 m exactly as presented in Chapter 4 [6].

The following three cases are simulated and compared:

- **Baseline MCT design:** The baseline MCT design investigated in this study is modeled in Chapter 3, and its major design parameters are presented in

Table 5.1: Parameters of the buoyancy-controlled MCT.

Symbol	Description	Value	Unit
$d_{\mathrm{r}}^{\mathrm{b}}$	Base rotor diameter	20	[m]
$P_{\mathrm{g}}^{\mathrm{r,b}}$	Base generator rated power	700	[kW]
$\nu_{\mathrm{B}}^{\mathrm{b}}$	Base volume of each buoyancy tank	31.215	[m^3]
$z^{\min}$	Minimum vertical position	50	[m]
$z^{\max}$	Maximum vertical position	150	[m]
$b^{\min}$	Minimum buoyancy tank fill fraction	0	–
$b^{\max}$	Maximum buoyancy tank fill fraction	1	–
$\dot{b}^{\max}$	Maximum slew rate of fill fraction	7.45×10^{-4}	[1/s]
$m_{\mathrm{t}}^{\mathrm{b}}$	Total mass	497800	[kg]
$m_{\mathrm{r}}^{\mathrm{b}}$	Mass of base rotor	61573	[kg]
$m_{\mathrm{g}}^{\mathrm{b}}$	Mass of base generator	2246.9	[kg]
$m_{\mathrm{B}}^{\mathrm{b}}$	Mass of base buoyancy tank	20427	[kg]
ζ	Coefficient for fill fraction equation (5.7)	0.65	[s/m]
κ	Coefficient for fill fraction equation (5.7)	-0.0026	[1/m]
α_1	Coefficient for rotor mass equation	74.2832	[kg/m]
α_2	Coefficient for rotor mass equation	2.9158	–
β_1	Coefficient for generator mass equation	5.34	[kg/kW]
β_2	Coefficient for generator mass equation	0.9223	–
γ_1	Coefficient for variable buoyancy mass equation	650.0721	[$\mathrm{kg/m}^3$]

Table 5.1. The mechanical and structural design of this system was detailed in Chapter 3, which lacks an analysis to account for the structural design and its effect on the harnessed power. Here, the spatiotemporal optimization is performed for the baseline MCT system, and the maximum harnessed power

along with the power-to-weight ratio for the baseline are found.

- **Co-design for a single MCT design parameter:** The co-design framework solves the optimization problem of maximizing the power-to-weight ratio for a single MCT design parameter. Three separate optimizations are performed for the buoyancy tank, generator, and rotor as major design parameters.

- **Co-design for multiple MCT design parameters:** The proposed co-design framework (as shown in Figure 5.2) evaluates multiple design parameters at the same time in relation to the maximum power-to-weight for the MCT system when operating in the spatiotemporal uncertain ocean environment.

Figure 5.3 compares the obtained average power-to-weight ratios over a 7-day period of the simulation for changes applied in each design parameter (± 10 % from its base value). From this result, the rotor diameter is the dominant design parameter, which significantly affects the power-to-weight ratio; also, the power-to-weight ratio depicts less sensitivity to the changes in generator rated power. The obtained results are reasonable since the harvested power is squared with the rotor diameter. Meanwhile, a bigger rotor diameter needs larger supporting infrastructure, including a larger nacelle and a stronger mooring system, which increases the weight more rapidly.

The design parameters of the baseline MCT, the optimal design parameters obtained through co-design for the rotor, and co-design for multiple parameters simultaneously are presented in Table 5.2. The average power-to-weight ratios over the sampling time for a 7-day period of the simulation under baseline design and optimal designs for the other two cases, along with the corresponding ocean current velocity (i.e., the turbine operating environment), are shown in Figure 5.4. The optimal MCT designs for case II and case III generate the same power (e.g., $P(v) = 256.99$ kW) but different total mass. The rotor diameter dominates other design parameters due to

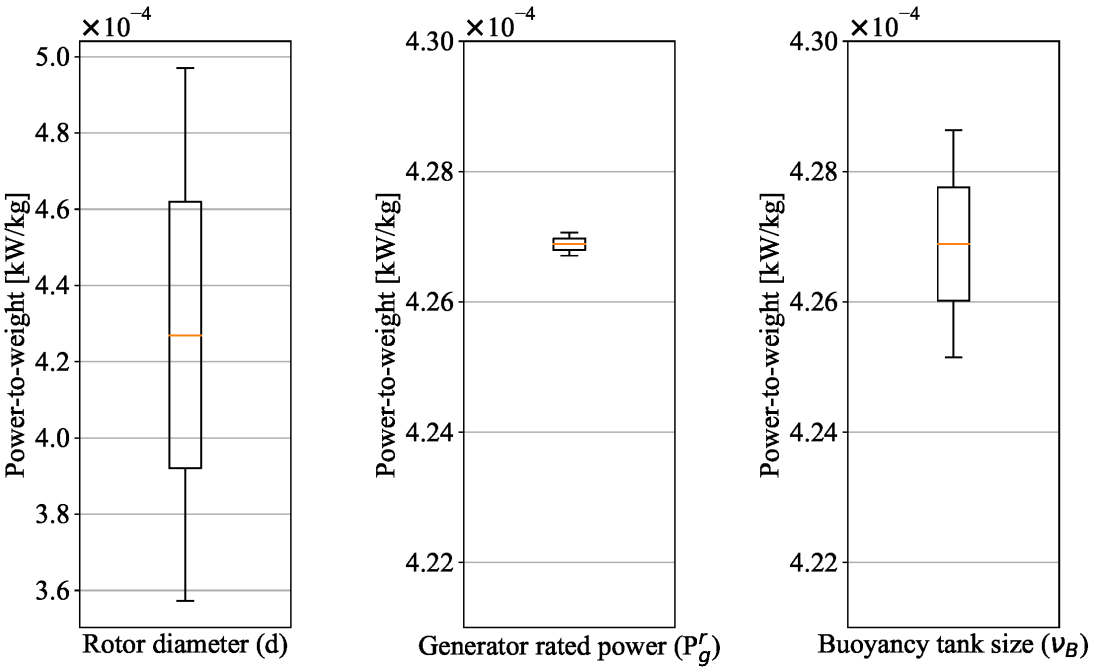

Figure 5.3: Comparing the power-to-weight ratio changes due to changes (± 10 % from its base value) in design parameters, including rotor, generator, and buoyancy tank. The power-to-weight ratio is more sensitive to changes in the rotor diameters.

its significant mass and effect on the power generation (P_{MCT}). From all these three cases, we see that the generated powers $P(v)$ are smaller than the baseline design of 700 kW, which means that the baseline design was away from the optimal. The reason is that the average ocean current speed that we used in this section is around 0.67 m/s, much smaller than the speed considered for formulating the baseline design 1.015 m/s. Through control co-design, the optimal generator rated power in case III is largely decreased from 700 kW in baseline design to 495 kW, much closer to the harvesting power 256.99 kW. These results highlight the importance of applying the geometric/spatiotemporal control co-design approach to design the optimal MCT in dynamic ocean environments.

The efficacy of the proposed approach, which maximizes the power-to-weight ratio and finds the optimal values of three key design parameters, is validated through

Table 5.2: Comparing the optimal MCT designs obtained through three cases: (case I) baseline MCT design, (case II) co-design for the rotor, and (case III) co-design for multiple design parameters.

Parameter	Unit	Case I	Case II	Case III
d_{r}	[m]	20	22	22
$P_{\mathrm{g}}^{\mathrm{r}}$	[kW]	700	700	495
ν_{B}	[m^3]	31.215	31.215	18.824
m_{r}	[kg]	61191	80795	80795
m_{g}	[kg]	2247	2247	1633
m_{B}	[kg]	20427	20427	12372
m_{t}	[kg]	497418	517021	508353
$P(\upsilon)$	[kW]	212.34	256.99	256.99
$\frac{P(\upsilon)}{m_{\mathrm{t}}}$	[kW/kg]	4.269e-4	4.971e-4	5.055e-4

simulations. The current study can be expanded on different aspects. The cost minimization objective can be added to the control co-design framework and formulated as a multi-objective optimization. Application of the GA algorithm for an outer optimization loop decreases the convergence speed, which could be replaced with another approach. Furthermore, the spatiotemporal optimization in the current format ignores the complete model of the MCT and the coupling between all MCT states. Although the presented model considers measured ocean currents, the increased forcing on different components and coupling between different components are neglected.

5.4 CONCLUSION

We presented a novel nested control co-design framework for a buoyancy-controlled MCT to take into account the spatiotemporal path planning and turbine geometry when maximizing the power-to-weight ratio. The investigated framework accounts

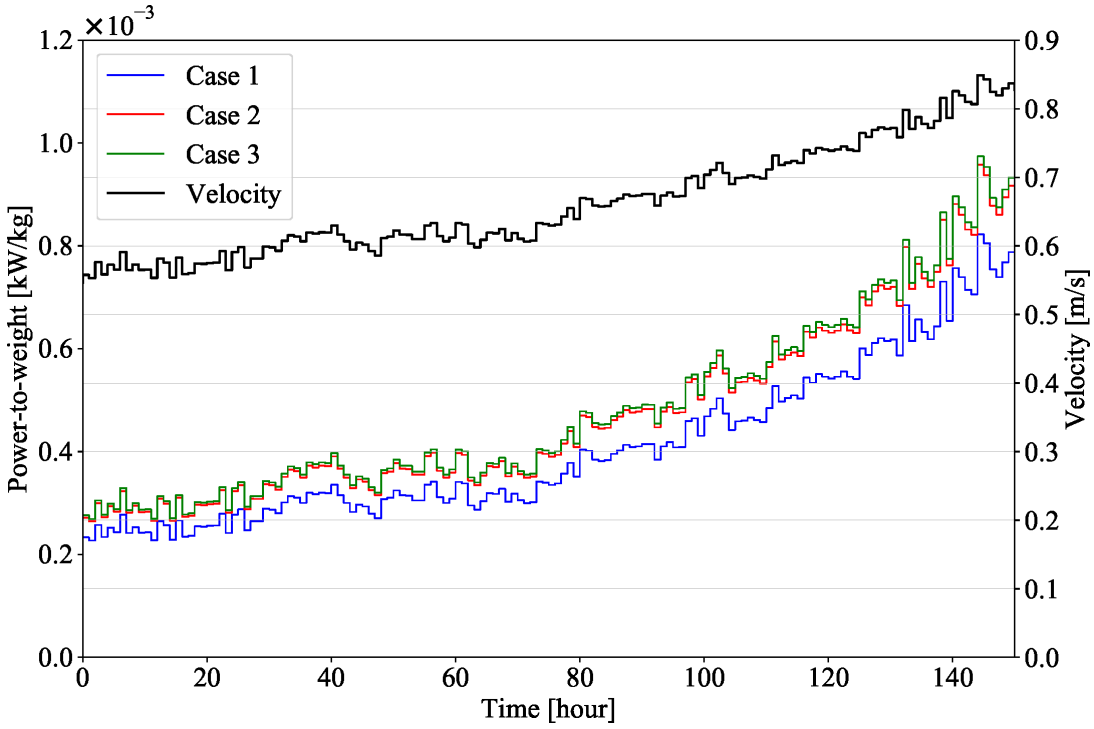

Figure 5.4: Comparing optimal power-to-weight ratios obtained by (case I) baseline MCT design, (case II) co-design for the rotor, and (case III) co-design for multiple design parameters. The results are shown over a sample real measured ocean current velocity from the Gulf Stream. The power-to-weight ratios are presented according to an average power over the time step.

for key design parameters, including the sizes of the generator, rotor, and variable buoyancy tank. In the current study, we assume an ideal case to maintain the baseline dimensions for the MCT system while changing the design parameters. The simulation results obtain the optimal design parameters according to the maximized harnessed power from the MCT.

CHAPTER 6
DISCUSSION AND FUTURE WORK

MHK turbines, including MCT and waver energy converters that are being used to harness renewable power from puissant oceanic resources, have recently gained significant attention from academia and industry. An autonomous MCT system, similar to an AUV, should be able to navigate itself without human intervention. This level of autonomy necessitates the first step, precise modeling, design, and numerical simulation. The MCT's parameter should be precisely chosen and designed to ensure a successful operation in the real oceanic environment.

Path planning is also a crucial task for the MHK turbines, facing challenges of the nonlinear and complex MCT system, as well as operation in a spatiotemporal uncertain underwater environment. The investigated problem in this thesis is different from the existing literature on AUV's path planning, pursuing different goals, such as minimizing travel time, minimizing path length, or minimizing energy consumption. The primary goal of the autonomous MCT is to find the path (i.e., operation depth) that maximizes the harnessed power from the ocean current since the ocean current speed is depth-dependent and time-varying. Indeed, the baseline design can be optimized according to the path control requirements, which results in the optimal MCT design with maximum harnessed power and minimum cost.

In this thesis, we propose (a) comprehensive dynamic modeling of the MCT, where real data recorded by the ADCP in the Gulf Stream are used as the real ocean environment. Numerical simulations results of the turbine performance for normal, hurricane, and fault conditions are presented and discussed; (b) vertical path planning of the MCT, where the problem is formulated as a novel spatiotemporal

optimization problem to maximize the total harvested power of the system in an uncertain oceanic environment. The RL-based method is designed to explore the optimal control actions, and results are quantitatively compared with the MPC-based strategy and the baseline A* method; (c) control co-design of the MCT, where the physical device geometry and turbine path control are optimized simultaneously. The main contributions and presented results in each area are summarized in the following.

6.1 CONCLUSION

1. Modeling of Buoyancy Controlled MCT. In chapter 3, we designed and modeled a 700 kW autonomous MCT, which is initially designed for the operation in the Gulf Stream of Florida's East Coast.

- **Contributions.** We propose a comprehensive modeling and numerical simulation of a 700 kW variable buoyancy controlled MCT for operation in a realistic environment of the Gulf Stream off the East Coast of Florida. We discuss the mechanical design and the main design components of the MCT and formulate the equations of motion for this 7 DOF system. The mathematical models of main actuators, including generator and buoyancy tank, are also presented.

- **Evaluation.** We evaluated the designed MCT under different scenarios to seek its operation range and response to different conditions. First, we simulated the MCT system for two simplified cases of homogeneous and shear flow speed profiles to assess the MCT's operating range. Then, we added the pitch control to the MCT system and showed that the designed MCT could perform while the pitch remains near 0°. We introduced multiple fault scenarios, including rotor braking and blade pitch fault, and demonstrated the MCT response for these cases. Finally, we simulated the real oceanic environment using the real recorded data from the Gulf Stream and represented the MCT operation for

three sample days considering both normal and hurricane conditions.

2. Path Planning Algorithm for Buoyancy Controlled MCT.

- **Contributions.** We propose a novel spatiotemporal optimization problem for the MCT vertical path planning operating in a spatiotemporally varying oceanic environment to maximize the total harvested power from the system. We also present a precise linear model to represent the net harvested power of a buoyancy-controlled MCT system, which includes directly generated power from ocean currents, consumed power for stabilizing the system at specified water depths, and consumed power to navigate to new optimal operating depths. To solve this problem, we utilize the MPC algorithm and, for the first time RL algorithm, which is compared with a base approach of A* method. To recast the path planning problem into the RL framework, the state set, action set, and reward functions are defined, and the problem is solved through three RL candidates of Q-learning, DQN, and PPO.

- **Evaluation.** We first justified the presented linear model for the net power of the MCT with its nonlinear model presented in Chapter 3. Then, we presented the simulation results for the optimal path obtained through RL algorithms, MPC algorithm, and the baseline A* method, where the average power and the total harnessed energy are compared. Finally, we represented two sample trajectories for the low and high shear profiles, where the MCT could successfully navigate both trajectories with maintaining the allowable range for both states and actuators.

4. Control Co-Design for Buoyancy Controlled MCT.

- **Contributions.** We propose a turbine geometric/spatiotemporal control co-design to maximize the power-to-weight ratio of a buoyancy-controlled MCT,

which couples physical design and path control. We identify the dominant design parameters of the MCT system, including rotor diameter, generator size, and buoyancy tank size, where the proposed framework aims to find the optimal values for these parameters. To formulate the relation between changes in the design parameters and the MTC's weight, we also presented formulations to model the weight deviations. The whole co-optimization nested framework is formulated through two optimization loops, i.e., an outer optimization loop responsible for the optimal design parameters and an inner optimization loop taking care of path planning.

- **Evaluation.** We evaluate the proposed control co-design framework for the designed buoyancy controlled MCT, where we identified that the power-to-weight ratio is more sensitive to changes in the rotor diameter. Then, we presented the optimal design parameters obtained after co-designing the MCT system, and we compared the power-to-weight ratio with a baseline MCT design.

6.2 FUTURE DIRECTIONS

Many directions remain open for future research in modeling, path planning, and control co-design of the MCT system, which are discussed as follows:

6.2.1 Modeling and Designing MCT

The designed MCT system is the initial design proposed for operation in the Gulf Stream, which can be extended in different aspects. Future work will focus on the extension of the flight controller and generator controller for the designed buoyancy controlled MCT. Also, a control methodology should be developed to integrate the harnessed power from the MCT into power grids using energy storage and converter. After finalizing the whole design and performing simulations to evaluate the MCT

performance under different conditions, it should be validated in a scaled MCT (such as a 1/5th scale turbine) and then a full-scale turbine.

6.2.2 Path planning for MCT and Similar Applications

The proposed framework for path planning can be generalized to other energy-harvesting autonomous vehicles (such as airborne wind energy) to employ the real-recorded data from the spatiotemporally varying environment for path planning. The key factor here is to utilize the RL algorithm as a promising and learning-based algorithm to address path planning. The following steps are required to extend to other applications:

1. The ultimate objective is still power maximization; it is then intuitive to find an equation modeling the net power of the agent (similar to (4.10)-(4.20)).

2. The spatiotemporal environment can be modeled in either discrete gridded or continuous manners with respect to the path accuracy. The key concern here is to access sufficient field-recorded data to train the RL algorithms.

3. The specific energy-harvesting vehicle should be adapted with the RL framework, where the states are defined according to the environment and agent's operating mechanism, and the action set introduces the potential paths.

4. The final step is to find the most suitable reward function to yield the optimal path with the highest harvested power. Three reward functions are introduced in this thesis to cope with both discrete and continuous path planning, showing promising results and can be adjusted to other applications.

It is also critical to extend the proposed spatiotemporal optimization to the MCT array to maximize the total power of the array considering the wake effects among the MCTs and integrate the harnessed power into power grids using energy storage. One possible approach is to present a multi-layer optimization framework to address the

array optimization in the outer loop and include a single MCT power maximization in the second layer or inner loop. It can also complete the proposed integrated path planning and tracking framework by adding the MCT array optimization as a higher level in the optimization loop.

6.2.3 Control Co-design for MCT

This work is the first attempt to control co-design for a buoyancy-controlled MCT system. The current study can be expanded on different aspects. The cost minimization objective should be added to the control co-design framework in addition to the optimization of the power-to-weight ratio. Application of the GA algorithm for an outer optimization loop decreases the convergence speed, which could be replaced with an analytical approach with a faster convergence speed and stability guarantee. Furthermore, the spatiotemporal optimization in the current format ignores the complete model of the MCT and, in a broader view, a dynamic model of the MCT as well as the coupling between all MCT states. Although the presented model takes into account measured ocean currents, the increased forcing on different components is neglected, which is bounded by defining an upper limit for changing the design parameters. Finally, the ultimate goal of control co-design is to optimize the whole MCT design parameters with detailed modeling of the corresponding couplings.

BIBLIOGRAPHY

[1] A. v. Jouanne and T. K. A. Brekken, "Ocean and geothermal energy systems," *Proceedings of the IEEE*, vol. 105, no. 11, pp. 2147–2165, 2017.

[2] P. Jacobson, "Assessment and mapping of the riverine hydrokinetic energy resource in the continental united states," *Electric Power Research Insitute (EPRI)*, 2012.

[3] X. Yang, K. A. Haas, and H. M. Fritz, "Evaluating the potential for energy extraction from turbines in the gulf stream system," *Renewable Energy*, vol. 72, pp. 12–21, 2014.

[4] J. VanZwieten, A. Duerr, G. Alsenas, and H. Hanson, "Global ocean current energy assessment: an initial look," *Proceedings of the 1st Marine Energy Technology Symposium (METS13)*, 2013.

[5] K. Haas, "Assessment of energy production potential from ocean currents along the united states coastline," Georgia Tech Research Corporation, Tech. Rep., 2013.

[6] M. C. P. M. Machado, J. H. VanZwieten, and I. Pinos., "A measurement based analyses of the hydrokinetic energy in the gulf stream," *Journal of Ocean and Wind Energy*, vol. 3, no. 1, pp. 25–30, 2016.

[7] A. C. O'Sullivan and G. Lightbody, "Co-design of a wave energy converter using constrained predictive control," *Renewable energy*, vol. 102, pp. 142–156, 2017.

[8] A. Hasankhani, Y. Tang, A. Snyder, J. VanZwieten, and W. Qiao, "Control co-design for buoyancy-controlled mhk turbine: A nested optimization of geometry and spatial-temporal path planning," *arXiv preprint arXiv:2110.06470*, 2021.

[9] T. Wilberforce, Z. El Hassan, D. A., J. Thompson, B. Soudan, and A. Olabi, "Overview of ocean power technology," *Energy*, vol. 175, pp. 165–181, may 2019.

[10] S. Bin-Karim, M. Muglia, and C. Vermillion, "Centralized position optimization of multiple agents in spatiotemporally-varying environment: a case study with relocatable energy-harvesting autonomous underwater vehicles in the gulf stream," in *2019 IEEE Conference on Control Technology and Applications (CCTA)*. IEEE, 2019, pp. 264–269.

[11] P. F. Lermusiaux, C.-S. Chiu, G. G. Gawarkiewicz, P. Abbot, A. R. Robinson, R. N. Miller, P. J. Haley, W. G. Leslie, S. J. Majumdar, A. Pang *et al.*, "Quantifying uncertainties in ocean predictions," HARVARD UNIV CAMBRIDGE MA, Tech. Rep., 2006.

[12] T. Ueno, S. Nagaya, M. Shimizu, H. Saito, and N. Handa, "Development and demonstration test for floating type ocean current turbine system conducted in kuroshio current," in *2018 OCEANS-MTS/IEEE Kobe Techno-Oceans (OTO)*. IEEE, 2018, pp. 1–6.

[13] D. Coiro, G. Troise, F. Scherillo, A. De Marco, G. Calise, and N. Bizzarrini, "Development, deployment and experimental test on the novel tethered system gem for tidal current energy exploitation," *Renewable energy*, vol. 114, pp. 323–336, 2017.

[14] Q. Abu-al rubb, Khalil (Doha, "Water turbine with variable buoyancy," Patent 20 160 160 835, June, 2016. [Online]. Available: http://www.freepatentsonline.com/y2016/0160835.html

[15] F.-L. Chiu, S.-A. Lai, C.-F. Lee, Y.-A. Tzeng, and C.-Y. Hsin, "Design and analysis of the floating kuroshio turbine blades," *Journal of Taiwan Society of Naval Architects and Marine Engineers*, vol. 37, no. 2, pp. 73–81, 2018.

[16] J.-T. Wu, J.-H. Chen, C.-Y. Hsin, and F.-C. Chiu, "Dynamics of the fkt system with different mooring lines," *Polish Maritime Research*, 2019.

[17] A. Fleming, "Aquantis c-plane ocean current turbine project," Dehlsen Associates, LLC, Santa Barbara, CA (United States), Tech. Rep., 2015.

[18] Minesto – power from tidal and ocean currents. [Online]. Available: http.wwww.minesto.com

[19] V. S. Neary, M. Previsic, R. A. Jepsen, M. J. Lawson, Y.-H. Yu, A. E. Copping, A. A. Fontaine, K. C. Hallett, and D. K. Murray, "Methodology for design and economic analysis of marine energy conversion (mec) technologies," Sandia National Laboratories, Tech. Rep., 2014.

[20] S. Tandon, S. Divi, M. Muglia, C. Vermillion, and A. Mazzoleni, "Modeling and dynamic analysis of a mobile underwater turbine system for harvesting marine hydrokinetic energy," *Ocean Engineering*, vol. 187, p. 106069, 2019.

[21] V. S. Neary, M. Lawson, M. Previsic, A. Copping, K. C. Hallett, A. LaBonte, J. Rieks, and D. Murray, "Methodology for design and economic analysis of marine energy conversion (mec) technologies." Sandia National Lab.(SNL-NM), Albuquerque, NM (United States), Tech. Rep., 2014.

[22] A. Baheri, P. Ramaprabhu, and C. Vermillion, "Iterative 3d layout optimization and parametric trade study for a reconfigurable ocean current turbine array using bayesian optimization," *Renewable energy*, vol. 127, pp. 1052–1063, 2018.

[23] A. Tidal, "Environmental appraisal (ea) for the argyll tidal demonstrator project," Tech. Rep., 2013.

[24] K. Shirasawa, K. Tokunaga, H. Iwashita, and T. Shintake, "Experimental verification of a floating ocean-current turbine with a single rotor for use in kuroshio currents," *Renewable Energy*, vol. 91, pp. 189–195, 2016.

[25] S. Bin-Karim, A. Bafandeh, A. Baheri, and C. Vermillion, "Spatiotemporal optimization through gaussian process-based model predictive control: A case study in airborne wind energy," *IEEE Transactions on Control Systems Technology*, vol. 27, no. 2, pp. 798–805, 2017.

[26] K. Naik, S. Beknalkar, A. Mazzoleni, and C. Vermillion, "Fused geometric, structural, and control co-design framework for an energy-harvesting ocean kite," in *2021 American Control Conference (ACC)*. IEEE, 2021, pp. 3525–3531.

[27] Y. Dodo, S. Nagaya, T. Okada, M. Toyoda, and A. Ito, "Development and design of a floating type ocean current turbine system," in *Practical Design of Ships and Other Floating Structures*. Springer, 2019, pp. 732–755.

[28] D. Coiro, D. Iannuzzi, M. Coppola, L. Di Noia, G. Troise, N. Bizzarrini, and G. Lazzerini, "Coupling fixed pitch rotor design to pmg de-fluxing control for gemstar marine current turbine," in *2019 International Conference on Clean Electrical Power (ICCEP)*. IEEE, 2019, pp. 680–689.

[29] J. G. P. DehlsenJames, B. DehlsenGeoffrey, and F. Deane, "Method of controlling operating depth of an electricity-generating device having a tethered water current-driven turbine," Patent US6 091 161A, 2000. [Online]. Available: https://patents.google.com/patent/US6091161A/en#title

[30] "Southeast National Marine Renewable Energy Center," http://snmrec.fau.edu/, accessed: 2020-05-30.

[31] K. Sakata, T. Gonoji, and K. Takagi, "A motion of twin type ocean current turbines in realistic situations," *2012 Oceans - Yeosu*, 2012.

[32] K. Takagi, Y. Suyama, and K. Kagaya, "An attempt to control the motion of floating current turbine by the pitch control," *OCEANS'11 MTS/IEEE KONA*, 2011.

[33] K. Takagi, "Motion analysis of floating type current turbines," in *International Conference on Offshore Mechanics and Arctic Engineering*, vol. 44946. American Society of Mechanical Engineers, 2012, pp. 189–195.

[34] K. Takeda, K. Sakata, and K. Takagi, "Motion simulation of a twin-type ocean current turbine," *Journal of the Japan Society of Naval Architects and Ocean Engineers*, vol. 18, 2013.

[35] T. Gonoji and K. Takagi, "Motion of a twin-rotor ocean current turbine in transient state," *Journal of the Japan Society of Naval Architects and Ocean Engineers*, vol. 20, 2014.

[36] T. Gonoji, K. Takagi, and K. Takeda, "Motion of twin type ocean current turbine at the time of startup and accident," in *2013 OCEANS-San Diego*. IEEE, 2013, pp. 1–6.

[37] J. H. VanZwieten, N. Vanrietvelde, and B. L. Hacker, "Numerical Simulation of an Experimental Ocean Current Turbine," *IEEE Journal of Oceanic Engineering*, vol. 38, no. 1, pp. 131–143, Jan. 2013.

[38] P. Pyakurel, J. H. VanZwieten, C. Sultan, M. Dhanak, and N. I. Xiros, "Numerical simulation and dynamical response of a moored hydrokinetic turbine operating in the wake of an upstream turbine for control design," *Renewable Energy*, vol. 114, pp. 1134–1145, 2017.

[39] J. VanZwieten, F. Driscoll, A. Leonessa, and G. Deane, "Design of a prototype ocean current turbine—part ii: flight control system," *Ocean engineering*, vol. 33, no. 11-12, pp. 1522–1551, 2006.

[40] J. H. VanZwieten, P. Pyakurel, T. Ngo, C. Sultan, and N. I. Xiros, "An assessment of using variable blade pitch for moored ocean current turbine flight control," *International journal of marine energy*, vol. 13, pp. 16–26, 2016.

[41] B. Davis, J. Farrell, D. Swan, K. Jeffers *et al.*, "Generation of electrical power from the florida current of the gulf stream," in *Offshore Technology Conference*. Offshore Technology Conference, 1986.

[42] "Ocean energy technology: The davis hydro turbine," *Refocus*, vol. 2, no. 2, pp. 44–47, 2001.

[43] H. Swales, D. Coackley, S. Gupta, S. Way *et al.*, "Stability and loads validation of an ocean current turbine," 2014.

[44] W. D. Bolin, "Systems and methods for transportation and maintenance of a water current power generation system," Jun. 22 2017, uS Patent App. 15/446,207.

[45] "Ihi demonstrated the world's largest ocean current turbine for the first time in the world," *IHI Engineering review*, vol. 52, no. 1, pp. 6–9, 2019.

[46] D. Iaconangelo. Ocean electricity takes 'big step' with baseload project. [Online]. Available: https://www.eenews.net/stories/1063312473

[47] J.-F. Tsai, Y.-X. Zeng, and F.-C. Chiu, "Study on the hydrodynamic performance of a floating kuroshio current turbine," *Proceedings of the 3rd World Congress on Civil, Structural, and Environmental Engineering (CSEE'18)*, 2018.

[48] K. Shirasawa, J. Minami, and T. Shintake, "Scale-model experiments for the surface wave influence on a submerged floating ocean-current turbine," *Energies*, vol. 10, no. 5, p. 702, 2017.

[49] M. Drela, "Xfoil: An analysis and design system for low reynolds number airfoils," in *Low Reynolds number aerodynamics*. Springer, 1989, pp. 1–12.

[50] C. Hansen and N. Codes, "Airfoilprep," *NWTC Design Codes, Available: http://wind. nrel. gov/designcodes/preprocessors/airfoilprep/Last modified*, 2010.

[51] T. D. Ngo, C. Sultan, J. H. VanZwieten, and N. I. Xiros, "Constrained control of moored ocean current turbines with cyclic blade pitch variations," *IEEE Journal of Oceanic Engineering*, pp. 1–17, 2020.

[52] P. Pyakurel, J. H. VanZwieten, M. Dhanak, and N. I. Xiros, "Numerical modeling of turbulence and its effect on ocean current turbines," *International journal of marine energy*, vol. 17, pp. 84–97, 2017.

[53] M. A. D. Ali, N. R. Babu, and K. Varghese, "Collision free path planning of cooperative crane manipulators using genetic algorithm," *Journal of computing in civil engineering*, vol. 19, no. 2, pp. 182–193, 2005.

[54] M. S. Wiig, K. Y. Pettersen, and T. R. Krogstad, "Collision avoidance for underactuated marine vehicles using the constant avoidance angle algorithm," *IEEE Transactions on Control Systems Technology*, vol. 28, no. 3, pp. 951–966, 2019.

[55] S. A. Bortoff, "Path planning for uavs," in *Proceedings of the 2000 American Control Conference. ACC (IEEE Cat. No. 00CH36334)*, vol. 1, no. 6. IEEE, 2000, pp. 364–368.

[56] Z. Zeng, A. Lammas, K. Sammut, F. He, and Y. Tang, "Shell space decomposition based path planning for auvs operating in a variable environment," *Ocean Engineering*, vol. 91, pp. 181–195, 2014.

[57] C. Di Franco and G. Buttazzo, "Energy-aware coverage path planning of uavs," in *2015 IEEE international conference on autonomous robot systems and competitions*. IEEE, 2015, pp. 111–117.

[58] M. Cobb, J. Reed, J. Daniels, A. Siddiqui, M. Wu, H. Fathy, K. Barton, and C. Vermillion, "Iterative learning-based path optimization with application to marine hydrokinetic energy systems," *IEEE Transactions on Control Systems Technology*, 2021.

[59] A. Alvarez, A. Caiti, and R. Onken, "Evolutionary path planning for autonomous underwater vehicles in a variable ocean," *IEEE Journal of Oceanic Engineering*, vol. 29, no. 2, pp. 418–429, 2004.

[60] E. W. Dijkstra *et al.*, "A note on two problems in connexion with graphs," *Numerische mathematik*, vol. 1, no. 1, pp. 269–271, 1959.

[61] K. P. Carroll, S. R. McClaran, E. L. Nelson, D. M. Barnett, D. K. Friesen, and G. N. William, "Auv path planning: an a* approach to path planning with consideration of variable vehicle speeds and multiple, overlapping, time-dependent exclusion zones," in *Proceedings of the 1992 Symposium on Autonomous Underwater Vehicle Technology*. IEEE, 1992, pp. 79–84.

[62] D. Ferguson and A. Stentz, "Using interpolation to improve path planning: The field d* algorithm," *Journal of Field Robotics*, vol. 23, no. 2, pp. 79–101, 2006.

[63] Z. Zeng, L. Lian, K. Sammut, F. He, Y. Tang, and A. Lammas, "A survey on path planning for persistent autonomy of autonomous underwater vehicles," *Ocean Engineering*, vol. 110, pp. 303–313, 2015.

[64] M. P. Aghababa, M. H. Amrollahi, and M. Borjkhani, "Application of ga, pso, and aco algorithms to path planning of autonomous underwater vehicles," *Journal of Marine Science and Application*, vol. 11, no. 3, pp. 378–386, 2012.

[65] Y. Sun, J. Cheng, G. Zhang, and H. Xu, "Mapless motion planning system for an autonomous underwater vehicle using policy gradient-based deep reinforcement learning," *Journal of Intelligent & Robotic Systems*, vol. 96, no. 3-4, pp. 591–601, 2019.

[66] J. Ji, A. Khajepour, W. W. Melek, and Y. Huang, "Path planning and tracking for vehicle collision avoidance based on model predictive control with multiconstraints," *IEEE Transactions on Vehicular Technology*, vol. 66, no. 2, pp. 952–964, 2016.

[67] M. McNaughton, C. Urmson, J. M. Dolan, and J.-W. Lee, "Motion planning for autonomous driving with a conformal spatiotemporal lattice," in *2011 IEEE International Conference on Robotics and Automation*. IEEE, 2011, pp. 4889–4895.

[68] D. Saccani and L. Fagiano, "Autonomous uav navigation in an unknown environment via multi-trajectory model predictive control," in *2021 European Control Conference (ECC)*. IEEE, 2021, pp. 1577–1582.

[69] J. S. Willners, L. Toohey, and Y. Petillot, "Sampling-based path planning for cooperative autonomous maritime vehicles to reduce uncertainty in range-only localization," *IEEE Robotics and Automation Letters*, vol. 4, no. 4, pp. 3987–3994, 2019.

[70] S. Bin-Karim, M. Muglia, A. Mazzoleni, and C. Vermillion, "Control of a relocatable energy-harvesting autonomous underwater vehicle in a spatiotemporally-varying gulf stream resource," in *2018 Annual American Control Conference (ACC)*. IEEE, 2018, pp. 2575–2580.

[71] T. Wang, R. M. Lima, L. Giraldi, and O. M. Knio, "Trajectory planning for autonomous underwater vehicles in the presence of obstacles and a nonlinear flow field using mixed integer nonlinear programming," *Computers & Operations Research*, vol. 101, pp. 55–75, 2019.

[72] D. Kularatne, H. Hajieghrary, and M. A. Hsieh, "Optimal path planning in time-varying flows with forecasting uncertainties," in *2018 IEEE International Conference on Robotics and Automation (ICRA)*. IEEE, 2018, pp. 4857–4864.

[73] A. Ramos, V. García-Garrido, A. Mancho, S. Wiggins, J. Coca, S. Glenn, O. Schofield, J. Kohut, D. Aragon, J. Kerfoot *et al.*, "Lagrangian coherent structure assisted path planning for transoceanic autonomous underwater vehicle missions," *Scientific reports*, vol. 8, no. 1, pp. 1–9, 2018.

[74] M. K. Cobb, K. Barton, H. Fathy, and C. Vermillion, "Iterative learning-based path optimization for repetitive path planning, with application to 3-d crosswind flight of airborne wind energy systems," *IEEE Transactions on Control Systems Technology*, vol. 28, no. 4, pp. 1447–1459, 2019.

[75] A. Bafandeh and C. Vermillion, "Real-time altitude optimization of airborne wind energy systems using lyapunov-based switched extremum seeking control," in *2016 American Control Conference (ACC)*. IEEE, 2016, pp. 4990–4995.

[76] B. Garau, A. Alvarez, and G. Oliver, "Path planning of autonomous underwater vehicles in current fields with complex spatial variability: an A* approach," in *Proceedings of the 2005 IEEE international conference on robotics and automation*. IEEE, 2005, pp. 194–198.

[77] A. Bafande and C. Vermillion, "Altitude optimization of airborne wind energy systems via switched extremum seeking—design, analysis, and economic assessment," *IEEE Transactions on Control Systems Technology*, vol. 25, no. 6, pp. 2022–2033, 2016.

[78] A. Bafandeh and C. Vermillion, "Optimal altitude control of an integrated airborne wind energy system with globalized lyapunov-based switched extremum seeking," in *2018 European Control Conference (ECC)*. IEEE, 2018, pp. 2089–2094.

[79] F. Mandić, N. Mišković, and Z. Vukić, "Range–only navigation–maximizing system observability by using extremum seeking," *IFAC-PapersOnLine*, vol. 48, no. 16, pp. 101–106, 2015.

[80] J. Cochran, E. Kanso, S. D. Kelly, H. Xiong, and M. Krstic, "Source seeking for two nonholonomic models of fish locomotion," *IEEE Transactions on Robotics*, vol. 25, no. 5, pp. 1166–1176, 2009.

[81] A. Hernandez-Sanchez, I. Chairez, and A. Poznyak, "Extended integral sliding mode robust sub-gradient extremum seeking control for tracking trajectory

of autonomous underwater vehicle," in *2020 7th International Conference on Control, Decision and Information Technologies (CoDIT)*, vol. 1. IEEE, 2020, pp. 433–438.

[82] T. B. von See, T. Meurer, and J. Greinert, "Marine boundary layer tracking using an auv with ukf based extremum seeking," *IFAC-PapersOnLine*, vol. 54, no. 16, pp. 320–326, 2021.

[83] C. Liu, S. Lee, S. Varnhagen, and H. E. Tseng, "Path planning for autonomous vehicles using model predictive control," in *2017 IEEE Intelligent Vehicles Symposium (IV)*. IEEE, 2017, pp. 174–179.

[84] T. Shim, G. Adireddy, and H. Yuan, "Autonomous vehicle collision avoidance system using path planning and model-predictive-control-based active front steering and wheel torque control," *Proceedings of the Institution of Mechanical Engineers, Part D: Journal of automobile engineering*, vol. 226, no. 6, pp. 767–778, 2012.

[85] M. Graf Plessen, D. Bernardini, H. Esen, and A. Bemporad, "Spatial-based predictive control and geometric corridor planning for adaptive cruise control coupled with obstacle avoidance," *IEEE Transactions on Control Systems Technology*, vol. 26, no. 1, pp. 38–50, 2018.

[86] M. Kehs, C. Vermillion, and H. Fathy, "Online energy maximization of an airborne wind energy turbine in simulated periodic flight," *IEEE Transactions on Control Systems Technology*, vol. 26, no. 2, pp. 393–403, 2017.

[87] D. C. Fernández and G. A. Hollinger, "Model predictive control for underwater robots in ocean waves," *IEEE Robotics and Automation letters*, vol. 2, no. 1, pp. 88–95, 2016.

[88] C. V. Caldwell, D. D. Dunlap, and E. G. Collins, "Motion planning for an autonomous underwater vehicle via sampling based model predictive control," in *OCEANS 2010 MTS/IEEE SEATTLE*. IEEE, 2010, pp. 1–6.

[89] S. Aradi, "Survey of deep reinforcement learning for motion planning of autonomous vehicles," *IEEE Transactions on Intelligent Transportation Systems*, pp. 1–20, 2020.

[90] B. Wang, Z. Liu, Q. Li, and A. Prorok, "Mobile robot path planning in dynamic environments through globally guided reinforcement learning," *IEEE Robotics and Automation Letters*, vol. 5, no. 4, pp. 6932–6939, 2020.

[91] J. Xie, Z. Shao, Y. Li, Y. Guan, and J. Tan, "Deep reinforcement learning with optimized reward functions for robotic trajectory planning," *IEEE Access*, vol. 7, pp. 105 669–105 679, 2019.

[92] Q. Zhang, K. Wu, and Y. Shi, "Route planning and power management for phevs with reinforcement learning," *IEEE Transactions on Vehicular Technology*, vol. 69, no. 5, pp. 4751–4762, 2020.

[93] M. Deisenroth and C. E. Rasmussen, "Pilco: A model-based and data-efficient approach to policy search," in *Proceedings of the 28th International Conference on machine learning (ICML-11)*. Citeseer, 2011, pp. 465–472.

[94] Y. Pan, G. I. Boutselis, and E. A. Theodorou, "Efficient reinforcement learning via probabilistic trajectory optimization," *IEEE transactions on neural networks and learning systems*, vol. 29, no. 11, pp. 5459–5474, 2018.

[95] M. Raissi, P. Perdikaris, and G. E. Karniadakis, "Numerical gaussian processes for time-dependent and nonlinear partial differential equations," *SIAM Journal on Scientific Computing*, vol. 40, no. 1, pp. A172–A198, 2018.

[96] C. Shen, Y. Shi, and B. Buckham, "Trajectory tracking control of an autonomous underwater vehicle using lyapunov-based model predictive control," *IEEE Transactions on Industrial Electronics*, vol. 65, no. 7, pp. 5796–5805, 2017.

[97] E. Meyer, H. Robinson, A. Rasheed, and O. San, "Taming an autonomous surface vehicle for path following and collision avoidance using deep reinforcement learning," *IEEE Access*, vol. 8, pp. 41 466–41 481, 2020.

[98] S. T. Havenstrøm, A. Rasheed, and O. San, "Deep reinforcement learning controller for 3d path following and collision avoidance by autonomous underwater vehicles," *Frontiers in Robotics and AI*, vol. 7, p. 211, 2021.

[99] E. Meyer, A. Heiberg, A. Rasheed, and O. San, "Colreg-compliant collision avoidance for unmanned surface vehicle using deep reinforcement learning," *IEEE Access*, vol. 8, pp. 165 344–165 364, 2020.

[100] Z. He, L. Dong, C. Sun, and J. Wang, "Asynchronous multithreading reinforcement-learning-based path planning and tracking for unmanned underwater vehicle," *IEEE Transactions on Systems, Man, and Cybernetics: Systems*, 2021.

[101] M. Garcia-Sanz, "Control co-design: an engineering game changer," *Advanced Control for Applications: Engineering and Industrial Systems*, vol. 1, no. 1, p. e18, 2019.

[102] R. G. Coe, G. Bacelli, S. Olson, V. S. Neary, and M. B. Topper, "Initial conceptual demonstration of control co-design for wec optimization," *Journal of Ocean Engineering and Marine Energy*, vol. 6, no. 4, pp. 441–449, 2020.

[103] J. Lyu, O. Abdelkhalik, and L. Gauchia, "Optimization of dimensions and layout of an array of wave energy converters," *Ocean Engineering*, vol. 192, p. 106543, 2019.

[104] D. R. Herber and J. T. Allison, "Wave energy extraction maximization in irregular ocean waves using pseudospectral methods," in *International Design Engineering Technical Conferences and Computers and Information in Engineering Conference*, vol. 55881. American Society of Mechanical Engineers, 2013, p. V03AT03A018.

[105] D. R. Herber, "Dynamic system design optimization of wave energy converters utilizing direct transcription," 2014.

[106] F. R. Driscoll, G. M. Alsenas, P. P. Beaujean, S. Ravenna, J. Raveling, E. Busold, and C. Slezycki, "A 20 KW open ocean current test turbine," in *OCEANS 2008*, Sep. 2008.

[107] M. Borghi, F. Kolawole, S. Gangadharan, W. Engblom, J. VanZwieten, G. Alsenas, W. Baxley, and S. Ravenna, "Design, fabrication and installation of a hydrodynamic rotor for a small-scale experimental ocean current turbine," in *2012 Proceedings of IEEE Southeastcon*. IEEE, 2012.

[108] M. U. Rentschler, F. Adam, and P. Chainho, "Design optimization of dynamic inter-array cable systems for floating offshore wind turbines," *Renewable and Sustainable Energy Reviews*, vol. 111, pp. 622–635, 2019.

[109] J. H. VanZwieten, N. Vanrietvelde, and B. L. Hacker, "Numerical simulation of an experimental ocean current turbine," *IEEE Journal of Oceanic Engineering*, vol. 38, no. 1, pp. 131–143, 2012.

[110] T. I. Fossen, "Guidance and control of ocean vehicles," *University of Trondheim, Norway, Printed by John Wiley & Sons, Chichester, England, ISBN: 0 471 94113 1, Doctors Thesis*, 1999.

[111] Y. Tang, Y. Zhang, A. Hasankhani, and J. VanZwieten, "Adaptive super-twisting sliding mode control for ocean current turbine-driven permanent magnet synchronous generator," in *2020 American Control Conference (ACC)*. IEEE, 2020, pp. 211–217.

[112] The fleet type submarine online submarine trim and drain systems (chapter 2). [Online]. Available: https://maritime.org/doc/fleetsub/trim/chap2.htm

[113] J. VanZwieten, W. Baxley, G. Alsenas, I. Meyer, M. Muglia, C. Lowcher, J. Bane, M. Gabr, R. He, T. Hudon *et al.*, "Ss marine renewable energy–ocean current turbine mooring considerations," in *Offshore Technology Conference*. Offshore Technology Conference, 2015.

[114] W. E. Baxley, J. VanZweiten, and N. Small, "Measuring the effects of hurricanes on major ocean currents and implications for ocean energy devices," in *2019 IEEE/OES Twelfth Current, Waves and Turbulence Measurement (CWTM)*, 2019, pp. 1–6.

[115] Monitoring and prediction of waves and shoreline changes. [Online]. Available: http://cdip.ucsd.edu/m/products/?stn=134p1&param=waveHs

[116] T. D. Ngo, C. Sultan, J. H. VanZwieten, and N. I. Xiros, "Constrained control of moored ocean current turbines with cyclic blade pitch variations," *IEEE Journal of Oceanic Engineering*, vol. 46, no. 2, pp. 594–610, 2020.

[117] T. D. Ngo., C. Sultan, J. H. VanZwieten, and N. I. Xiros, "Model predictive control for moored ocean current turbines," in *2017 American Control Conference (ACC)*. IEEE, 2017, pp. 875–880.

[118] B. Pearson and B. Fox-Kemper, "Log-normal turbulence dissipation in global ocean models," *Physical review letters*, vol. 120, no. 9, 2018.

[119] I. Lozovatsky, K. Shearman, A. Pirro, and H. J. S. Fernando, "Probability distribution of turbulent kinetic energy dissipation rate in stratified turbulence: Microstructure measurements in the southern california bight," *JGR Oceans*, vol. 124, no. 7, pp. 4591–4604, July 2019.

[120] J. Yan, K. Li, B. Er-Wei, J. Deng, and A. M. Foley, "Hybrid probabilistic wind power forecasting using temporally local gaussian process," *IEEE transactions on sustainable energy*, vol. 7, no. 1, pp. 87–95, Jan. 2016.

[121] H. Cai, X. Jia, J. Feng, W. Li, Y.-M. Hsu, and J. Lee, "Gaussian process regression for numerical wind speed prediction enhancement," *Renewable Energy*, vol. 146, pp. 2112–2123, 2020.

[122] K.-C. Ma, L. Liu, and G. S. Sukhatme, "Informative planning and online learning with sparse gaussian processes," in *2017 IEEE International Conference on Robotics and Automation (ICRA)*. IEEE, 2017, pp. 4292–4298.

[123] G. A. Hollinger, A. A. Pereira, J. Binney, T. Somers, and G. S. Sukhatme, "Learning uncertainty in ocean current predictions for safe and reliable navigation of underwater vehicles," *Journal of Field Robotics*, vol. 33, no. 1, pp. 47–66, 2016.

[124] Y. Huang, Y. Tang, H. Zhuang, J. VanZwieten, and L. M. Cherubin, "Physics-informed tensor-train convlstm for volumetric velocity forecasting of loop current," *Frontiers in Artificial Intelligence*, p. 197, 2021.

[125] L. Csató and M. Opper, "Sparse on-line gaussian processes," *Neural computation*, vol. 14, no. 3, pp. 641–668, 2002.

[126] J. Hensman, N. Fusi, and N. D. Lawrence, "Gaussian processes for big data," *arXiv preprint arXiv:1309.6835*, 2013.

[127] C. Zhang, H. Wei, X. Zhao, T. Liu, and K. Zhang, "A gaussian process regression based hybrid approach for short-term wind speed prediction," *Energy Conversion and Management*, vol. 126, pp. 1084–1092, 2016.

[128] S. Couch and I. Bryden, "Tidal current energy extraction: Hydrodynamic resource characteristics," *Proceedings of the Institution of Mechanical Engineers, Part M: Journal of Engineering for the Maritime Environment*, vol. 220, no. 4, pp. 185–194, 2006.

[129] J. Schulman, F. Wolski, P. Dhariwal, A. Radford, and O. Klimov, "Proximal policy optimization algorithms," *arXiv preprint arXiv:1707.06347*, 2017.

[130] T. Marine, "Workhorse long ranger 75 khz adcp," Brochure, 2020. [Online]. Available: http://www.teledynemarine.com/Lists/Downloads/long-ranger-datasheet-lr.pdf

[131] Y. Tang, J. VanZwieten, B. Dunlap, D. Wilson, C. Sultan, and N. Xiros, "In-stream hydrokinetic turbine fault detection and fault tolerant control-a benchmark model," in *2019 American Control Conference (ACC)*. IEEE, 2019, pp. 4442–4447.

[132] W. B. Greer and C. Sultan, "Shrinking horizon model predictive control method for helicopter–ship touchdown," *Journal of Guidance, Control, and Dynamics*, vol. 43, no. 5, pp. 884–900, 2020.

[133] A. J. Jerri, "The shannon sampling theorem—its various extensions and applications: A tutorial review," *Proceedings of the IEEE*, vol. 65, no. 11, pp. 1565–1596, 1977.

[134] L. Fingersh, M. Hand, and A. Laxson, "Wind turbine design cost and scaling model," National Renewable Energy Lab.(NREL), Golden, CO (United States), Tech. Rep., 2006.